Biophysical Characterization of Interactions Between Two Membrane Proteins: SERCA and Sarcolipin

A DISSERTATION
SUBMITTED TO THE FACULTY OF
UNIVERSITY OF MINNESOTA
BY

Alysha Ann Dicke

IN PARTIAL FULFILLMENT OF THE REQUIREMENTS
FOR THE DEGREE OF
DOCTOR OF PHILOSOPHY

Adviser
Dr. Gianluigi Veglia

May 2017

© Alysha Ann Dicke 2017

Acknowledgements

Foremost, I would like to thank the mentors who were the most positive influences throughout my scientific training. My advisor at Gustavus, Dr. Brandy Russell, first taught me the fundamentals about research and inspired my interest in structural biology. Dr. Cheryl Ethen, my co-worker at R&D Systems, taught me the importance of being meticulous about controls for every experiment. Both continued to provide support throughout my graduate studies and have contributed to making this work possible. I am deeply grateful to Dr. Laurie Parker for reminding me about the good sides of academia and helping me to look at my work with fresh eyes. Dr. Parker has also been a phenomenal role model for approaching life even outside of science.

Second, I am indebted to Kailey Soller. She has been there for me not only as a colleague to talk through our respective projects together, but has also been an incredible friend and has been instrumental in helping me to overcome many of the challenges I faced during graduate school. Thank you, Kailey, for being the incredible person that you are.

I am also grateful to the lab members and fellow graduate students who influenced this work along the way, taught me many of the needed skills, or helped make lab more enjoyable: Dr. Vitaly Vostrikov, Dr. Kaustubh Mote, Dr. Jonggul Kim, Dr. Manu Subrahmanian, Dr. Leanna McDonald, Dr. Geoffrey Li, Dr. T. Gopinath, Xaiobai Patrinostro, Chelsea Lau, Sarah Nelson, Adak Karamafrooz, Seth Kimball, and Max Anderson.

Of course, my family and close friends need to be acknowledged for their unwavering support; thank you.

"You cannot buy the revolution. You cannot make the revolution. You can only be the revolution. It is in your spirit, or it is nowhere."

-Ursula K. Le Guin

Abstract

Understanding the structures and interactions of proteins that interact with membranes has many implications. Membrane proteins play roles in the transfer of necessary materials and information between cells and their environments as well as within cells (e.g., between the cytosol and organelles). As such, they currently constitute more than half of all drug targets, and some peptides, such as antimicrobial peptides (AMPs), are also being investigated for their therapeutic use in treating bacterial infections for humans. However, studying the structures of membrane proteins has proven more challenging compared to soluble proteins. This is due to the necessity of including the membrane or a good membrane mimic to ensure the integrity of the membrane protein remains intact, as poor mimics or no membrane can detrimentally affect membrane protein structure and function. Some proteins, like the AMP chionodracine, are highly amenable to study with methods such as solution NMR spectroscopy (Chapter 2), but larger membrane proteins prove challenging or impossible to measure in solution due to the molecular weight limitations and frequently do not crystallize easily either. Solid-state NMR spectroscopy (ssNMR) has helped to overcome these obstacles and more methodology continues to be developed expanding the application of ssNMR. For example, Chapters 3 and 4 of this thesis describe new ssNMR methods using the sarco(endo)plasmic reticulum (SERCA) and sarcolipin (SLN), respectively. SERCA and SLN form a crucial complex in the membrane of the sarcoplasmic reticulum in skeletal muscles cells. Muscle relaxation is largely controlled by SERCA pumping calcium out of the cytosol using energy from ATP hydrolysis, and SLN inhibits SERCA as well as uncouples the ATP hydrolysis and calcium transport. SLN's effect on SERCA leads to more heat production, which may be important to thermogenesis in mammals as well as an additional mechanism to control energy expenditure. Chapter 5 primarily uses ssNMR with the goal to better understand the mechanism by which SLN inhibits and uncouples SERCA. Overall, gaining a better understanding of how SERCA is regulated will aid in developing therapies for diseases resulting from improper calcium cycling.

Table of Contents

List of Tables

Chapter 2 - Structure and Membrane Interactions of Chionodracine, a Piscidin-Like Antimicrobial Peptide from the Icefish *Chionodraco hamatus*

Chapter 5 - Mapping of SLN Conformational States Along the Enzymatic Pathway of SERCA

List of Figures

Chapter 1 - Introduction

Chapter 2 - Structure and Membrane Interactions of Chionodracine, a Piscidin-Like Antimicrobial Peptide from the Icefish *Chionodraco hamatus*

Chapter 3 - Ca^{2+} ATPase Conformational Transitions in Lipid Bilayers Mapped by Site-directed Ethylation and Solid-State NMR

Chapter 4 - Probing Residue-Specific Water–Protein Interactions in Oriented Lipid Membranes via Solid-State NMR Spectroscopy

Chapter 5 - Mapping of SLN Conformational States Along the Enzymatic Pathway of SERCA

Chapter 6 - Conclusions

List of Abbreviations

SERCA: Sarco(endo)plasmic reticulum Ca^{2+} ATPase

SLN: Sarcolipin

PDB: Protein Data Bank

AMPs: Antimicrobial peptides

NMR: Nuclear magnetic resonance spectroscopy

ssNMR: Solid-state NMR

O-ssNMR: Oriented ssNMR

MAS: Magic angle spinning NMR

NOE: Nuclear Overhauser effect

DMPC: Dimyristoylphosphatidylcholine

DHPC: Dihexanoylphosphatidylcholine

PISEMA: Polarization inversion with spin exchange at the magic angle

PISA: Polarity indexed slant angle

Cnd: Chionodracine

ER: Endoplasmic reticulum

SR: Sarcoplasmic reticulum

Ryr: Ryanodine receptor

ATP: Adenosine triphosphate

smORFs: Small open reading frames

PLN: Phospholamban

DPC: Dodecylphosphocholine

DOPC: 1,2-Dioleoyl-*sn*-glycero-3-phosphocholine

DOPE: 1,2-Dioleoyl-*sn*-glycero-3-phosphoethanolamine

POPC: 1-Palmitoyl,2-oleyl-sn-glycero-3-phosphocholine

TMs: Transmembrane helices

MIC: Minimum inhibitory concentrations

TEM: Transmission electron microscopy

LUVs: Large unilamellar vesicles

POPG: 1-Palmitoyl-2-oleoyl-sn-glycero-3-phosphoglyceol

CA: Cardiolipin

ANS: 1-Aminonaphtalene-8-sulfonic acid

TOCSY: Total correlation spectroscopy

TPPI: Time-proportional phase incrementation

SA: Simulated annealing

IM: Inner membrane

OM: Outer membrane

OMV: Outer membrane vesicles

MMTS: Methylmethanethiosulfonate

EMTS: Ethylmethanethiosulfonate

DARR: Dipolar assisted rotational resonance

$C_{12}E_8$: Octaethylene glycol monododecyl ether

PRE: Paramagnetic relaxation enhancement

CAM: Carbamidomethylated

ADP: Adenosine diphosphate

TEMPO: (2,2,6,6-Tetramethylpiperidin-1-yl)oxyl

TLC: Thin-layer chromatography

SLF: Separated local field

WE: Water-edited

DAGK: Diacylglycerol kinase

SE: Sensitivity enhanced

MBP: Maltose binding protein

CP: Cross polarization

RF: Radio frequency

HETCOR: Heteronuclear correlation

WIM: Windowless isotropic mixing

FSLG: Frequency-switched Lee–Goldburg

SPINAL64: Small phase incremental alteration 64

PKA: Protein kinase A

pSLN: Phosphorylated SLN

OG: *n*-Octyl-β-D-glucopyranoside

DDM: *n*-Dodecyl-β-D-maltoside

CaMKII: Ca^{2+}/calmodulin-dependent protein kinase II

NHMFL: National High Magnetic Field Laboratory

STK16: Serine/threonine kinase 16

AMPPCP: β,γ-Methyleneadenosine 5′-triphosphate disodium salt

Syn pSLN: Synthetic pSLN

O-GlcNAc: *N*-Acetylglucosamine

OGT: O-Linked β-N-acetylglucosamine transferase

WT: Wild-Type

AFA: Monomeric form of PLN

MLN: Myoregulin

DWORF: Dwarf open reading frame

SCL: Sarcolamban

ELN: Endoregulin

ALN: Another-regulin

Chapter 1 – Introduction

Biophysical Characterization of Interactions Between Two Membrane Proteins: SERCA and Sarcolipin

1. Introduction

1.1 Membrane Proteins

Determining the structure and dynamics of proteins to understand their corresponding functions has been a hallmark of biochemistry,[1-3] especially as these studies aid the rational design of therapeutics. Membrane proteins are particularly important to human health. They constitute 20-30% of the proteins in all genomes[4-6] and have critical roles in mediating both the transfer of material, such as lipids, sugars, and metals, as well as the transfer of information across the membranes of cells. Significantly, membrane proteins currently comprise more than half of all drug targets.[7-10] However, despite their importance to drug development, membrane proteins are still underrepresented in the Protein Data Bank (PDB).[11,12] More and more membrane protein structures are being solved with new method developments, but they still lag behind structures solved for globular proteins,[13-15] as currently membrane proteins comprise only ~2% of the protein structures deposited in the data bank.[14,16]

In addition to being drug targets, protein-based therapeutics are emerging as a new strategy to treat a variety of diseases including cancers,[17] chronic inflammatory conditions, and other diseases.[18] Many of these therapies are based on antibodies,[18] but peptide therapeutics are also being developed with the main focus on treating cancers and metabolic diseases,[19,20] and many of these peptides interact with biological membranes. For example, naturally-occurring peptide hormones and antimicrobial peptides (AMPs) interact with biological membranes.[13,21-23] AMPs, which interact directly with some cell membranes, have recently gained considerable attention as potential antibiotics,[24-26] especially as bacteria are rapidly becoming resistant to conventional

treatments.[26,27] Further structural characterization of membrane proteins to understand their functions as well as their interactions with other proteins and molecules is imperative to human health as they are both important drug targets and potential therapeutics.

An essential consideration when studying membrane proteins is the membrane bilayer and its composition, as these are highly influential in driving membrane protein structure and function. The current understanding of the biological membrane is based on the fluid-mosaic model first introduced by Singer and Nicholson in 1972[28] (**Fig. 1A**).[29] Membranes are necessary for creating boundaries to the outside environment for the cell and for organelles within cells. The amphipathic nature of lipids causes them to spontaneously form a bilayer in aqueous solution with the hydrophilic heads exposed to the water and the hydrophobic tails facing each other.[28,30] Membrane proteins are either embedded within the membrane (integral membrane proteins) or interact with the polar headgroups of the lipids (peripheral membrane proteins). A key component of the model is that both the lipids and proteins can diffuse freely,[28,31,32] but they are distributed asymmetrically among the two monolayers of the membrane.[28,33] Since this model was introduced, studies have demonstrated that the membrane is more complex.[29] It actually has a high density of transmembrane proteins (**Fig. 1B**)[29] and some only bind to the membrane periodically.[34,35] Many membranes are also curved, can exist in different phases, and can be laterally heterogeneous or patchy.[29,35] Thus, membranes are variable, complex, and dynamic, which makes them much more than passive walls.[29,35]

Importantly, the diversity of the membrane, including the composition and phase, impacts the activity of membrane proteins,[36] and all of these aspects are dependent upon the type(s) of lipid(s) present in the membrane and interacting with the protein.[35] For example, the bilayer thickness is controlled by length of the acyl chain of the lipid. If there

is a mismatch between the hydrophobic region of the protein and that of the lipid bilayer, either the protein, the lipids, or both must deform such that the hydrophobic regions are not exposed to the aqueous solution.[36] While many studies indicate that the lipids adjust around the protein,[36,37] helices in transmembrane proteins may also tilt or flex to ensure that the hydrophobic areas stay within the hydrophobic core of the bilayer.[38-41] It has even been proposed that the tertiary structure and function of membrane proteins may be regulated by the bilayer thickness.[38] Likewise, membrane curvature is affected by the types of lipids and has been demonstrated to affect the secondary structure of membrane proteins such as AMPs.[36,42] Besides the acyl chain, the lipid head group can also alter the activity of membrane proteins;[43,44] changes in the charge can disrupt the association of proteins such as AMPs with the membrane when their association depends on electrostatic interactions.[42,45] Even specific lipid molecules are important as some membrane proteins require certain lipids to bind to them for their proper function.[46] Accordingly, different lipid types are prevalent for different organisms as well as organelles,[47] it is clear that the membrane proteins will vary accordingly. All of these considerations contribute to the interest of studying membrane proteins, but also the challenges in purifying and characterizing them.

1.2 Structural Studies of Membrane Proteins using Nuclear Magnetic Resonance Spectroscopy

Historically, protein structure determination has focused on X-ray crystallography and solution nuclear magnetic resonance (NMR) spectroscopy. However, the necessity of studying membrane proteins within a lipid bilayer or mimic has hindered structural determination, especially for membrane proteins that need lipid bilayers to maintain their

structural integrity.[15,48] This has been the major factor contributing to the relatively few solved structures for membrane proteins compared to globular proteins.[13-15] Advances in crystallography using new techniques to include lipids[49-51] have helped to determine more membrane protein crystal structures, but frequently these crystals provide data with low resolution.[52-54] On the other hand, solution NMR is limited by the size of the molecules studied; as the size increases, the tumbling slows and anisotropic interactions begin to broaden lines and complicate the spectra.[13] While solution NMR remains useful for studying small membrane proteins like peptides, solid-state NMR (ssNMR) has been revolutionary for membrane proteins. Not only can samples be prepared using large proteins and hydrated lipid bilayers,[55] but ssNMR has also developed two main methods, oriented ssNMR (O-ssNMR) and magic angle spinning (MAS) NMR, to deal with the anisotropy inherent in large systems such as membrane proteins reconstituted in lipid environments.

Chapter 2 of this thesis utilizes solution NMR to investigate the structure of the AMP chionodracine (Cnd), and so a brief description of solution NMR for membrane proteins is included here. The remaining chapters focus on using ssNMR to understand the structure and interactions of the membrane proteins sarcolipin (SLN) and a Ca^{2+}ATPase (SERCA), thus, the theory of ssNMR is described in greater detail.

1.2.1 Solution NMR Spectroscopy

In solution NMR, rapid molecular reorientation averages the anisotropic interactions of nuclei with the magnetic field to their isotropic values providing highly resolved spectra. Methodological developments have expanded the size limit for solution

NMR, but most of the structures solved are still of proteins below 35 kDa in molecular weight.[13] For membrane proteins, the membrane mimetic contributes to the overall molecular weight restricting the resolvable size of the protein even further.[56] As such, solution NMR is most useful for smaller transmembrane peptides or peptides that interact with lipid bilayers as these are more amenable to studies with detergents than large membrane proteins. Although the conventional methods for structural determination in solution NMR can be used for membrane peptides and proteins, special considerations must be considered when preparing these samples. As size limitations inhibit studying peptides in lipid vesicles, small membrane-mimetic systems such as micelles or isotropic bicelles are employed (**Fig. 2**),[13] but the types of detergents and/or lipids used also need to be considered as these can alter the structures of peptides. For example, sodium dodecyl sulfate has been shown to induce secondary structure characteristics that are not seen with other systems and may not be physiologically accurate.[13,57] Generally, having the hydrophobic diameter of the micelles match the hydrophobic thickness of the membrane protein aids in obtaining high-quality spectra.[58]

Furthermore, the conventional experiments in solution NMR establish the structure of the peptide, but they do not reveal information about the localization or orientation of the peptide relative to the membrane-mimetic system.[13] Thus, one more difference between solving structures of globular proteins compared to membrane proteins is the necessity to use experiments to ascertain this additional structural dimension. Common solution NMR experiments adapted for this purpose include nuclear Overhauser effect (NOE) measurements between the peptide and detergent,[13,59] residual dipole couplings,[13,60] and/or paramagnetic relaxation enhancements[13,61]. Overall, solution NMR

has significantly aided in the structural determination of peptides such as Cnd, but its use is limited for larger systems.

1.2.2 Oriented Solid-State NMR Spectroscopy

Between MAS and O-ssNMR, the two main methods for dealing with the anisotropic interactions in ssNMR samples, O-ssNMR takes advantage of the orientation-dependent interactions present to provide structural and topological information about the protein, which must be determined to fully describe the structure of a protein within the membrane. For example, α-helices may be described by their tilt, rotation, and immersion depth within the membrane (see **Fig. 3**) as well as the solvent exposure of specific residues.[62] O-ssNMR experiments may be used to obtain most of this information, but while high-quality, well-resolved spectra are needed, their quality and resolution depend upon the sample being well aligned relative to the magnetic field. Proper alignment requires special sample conditions, and it can be very challenging to prepare samples that produce high-quality spectra. Currently, there are several methods used to align proteins within lipid bilayers in a strong magnetic field. Originally, mechanical alignment was used in which lipid bilayers with the protein are stacked between thin glass slides.[54] The current commonly used method relies on bilayered mixed micelles or "bicelles"[63] (**Fig. 2**). This is the method that will be discussed in detail here as the optimization of the bicelle preparation protocol led to successful collection of most of the data in Chapters 4 and 5 of this thesis.

Bicelles are a mixture of at least two lipids; a long chain lipid (e.g. dimyristoylphosphatidylcholine, DMPC) that forms the bilayer and a short chain lipid (e.g.

dihexanoylphosphatidylcholine, DHPC) that covers the rim of the bilayer.[54,63] In order to form a bicelle that aligns with the magnetic field, an important factor to consider is the molar ratio between the long and short chain lipids (*q)*:

$$q = [\text{long chain}]/[\text{short chain}]$$

When lipids are mixed at certain ratios (*q*), bicelles in a liquid crystalline phase will form, and when they are placed in a strong magnetic field, the intrinsic magnetic susceptibility of the phospholipids that constitute the bicelle will cause their spontaneous alignment. This occurs such that the membrane normal, or the plane perpendicular to the surface of the bilayer, aligns perpendicularly to the external magnetic field.[64,65] Additionally, bicelles can be "flipped." When lanthanide ions are added, the sign of the anisotropy for the lipids' magnetic susceptibility is reversed causing the membrane normal to be parallel with the external magnetic field.[66,67] The bicelle system has several advantages over the mechanically-aligned bilayers: 1) normal glass tubes can be used allowing the samples to be placed in a round solenoid coil, which is better for signal detection/sensitivity than the rectangular scroll coil needed for glass plate samples,[54,68] 2) hydration can be controlled more finely, and 3) these samples have a larger filling factor (i.e., the fraction of the coil's sensitive volume that is filled with sample).[54] However, the down side is that bicelles are more restrictive than mechanically-aligned samples in the types of lipids that can be used.

Proper alignment of bicelles is imperative to collecting high-quality spectra from these samples. If the sample is not aligned well relative to the magnetic field, then all orientations of the molecules in question will be present in the sample resulting in a "powder pattern" (see **Fig. 4**). For example, the chemical shift anisotropy of the nucleus is an orientation-dependent nuclear spin interaction. It can be described by the equation:[69]

$$\omega_{CS}=-\omega_0 \sigma_{iso} -1/2\ \omega_0 \Delta\ [3\cos^2\theta-1 + \eta\sin^2\theta\ \cos 2\Phi]$$

Where ω_{CS} is the chemical shift, ω_0 is the Larmor frequency, $-\omega_0\sigma_{iso}$ is the isotropic frequency, and θ and Φ are the angles as described by **Figure 4**. The symmetry of the chemical shift anisotropy is described by η while Δ describes the span (see **Fig. 4**). Both of these are dependent on the type of nucleus. When all possible orientations of the nucleus (e.g., the entire range of angles, θ and Φ) are present, then all possible chemical shifts will be observed resulting in the powder pattern. Conversely, when the molecules within the sample are uniformly aligned and only one set of angles are present then each nucleus will only give rise to one peak in the NMR spectrum, and the position of this peak will depend on the nucleus' orientation.

Separated local field experiments utilize this orientation dependence and separate the chemical shift from the local field. For example, in the PISEMA experiment (Polarization Inversion with Spin Exchange at the Magic Angle), chemical shifts are correlated to dipolar couplings.[70] Typically, this is the chemical shift of ^{15}N-labeled amides with the dipolar coupling between the amide ^{15}N and the bonded ^{1}H. Like the chemical shift anisotropy described above, the dipolar coupling is also orientation-dependent, but it is given by a different equation:

$$\omega_{DC}= \omega_{max}\ (3\cos^2\theta-1)/2$$

Where ω_{DC} is the dipolar coupling, ω_{max} is the maximum dipolar coupling between the ^{15}N and ^{1}H nucleus, and θ is the angle of the amide ^{15}N - ^{1}H bond relative to the external magnetic field.

In the case of helices, the resulting spectra have a very specific pattern. First, as each amino acid has only one amide bond, each peak in the spectra represents one residue. (There may be additional peaks for nitrogen-containing side chains, but these will be distinct from the backbone). As transmembrane helices have 3.6 residues per helical turn, they give rise to a Polarity Indexed Slant Angle (PISA) wheel in PISEMA spectra with 3.6 peaks per turn of the PISA wheel. Thus, the spectra can be understood as a projection of the peptide's helical wheel.[13]

The PISA wheel provides important topological information as its shape, size, and position are directly related to the angle between the helical axis (τ) as well as the rotation angle (ρ) and the dynamics of the protein (**Fig. 5**). For example, as the tilt of the helix increases relative to the bilayer normal, the span of ^{15}N-^{1}H dipolar couplings in the PISA wheel becomes larger (**Fig. 5**). The rotation about the helical axis can be determined with only a single resonance assignment within the distribution of peaks in the PISA wheel.[13] However, PISEMA on its own does not provide information about the immersion depth of the protein within the bilayer or its solvent exposure, which are necessary for fully characterizing the structure. PRE measurements can be used for determining immersion depth.[62] In Chapter 4 of this thesis, the development of a water-edited version of PISEMA that enables probing the solvent exposure of the protein is described.[71] Overall, the various types of experiments that can be performed using the O-ssNMR approach provide important, detailed information about the topology of a protein in the bilayer and can be used to monitor even small changes in structure such as alterations of tilt angles.[58,72-74]

1.2.3 Magic Angle Spinning Solid-State NMR Spectroscopy

MAS ssNMR and O-ssNMR are complementary techniques and each one provides important information for understanding a protein's conformation and dynamics. Unlike other methods, such as X-ray crystallography and solution NMR, MAS ssNMR is not as limited by sample preparations based on size limitations.[75] In fact, the lipid vesicles (**Fig. 2**) typically used in ssNMR samples have correlation times in the μs range[76] and under these conditions, the dipolar couplings and chemical shifts are orientation dependent. Just like O-ssNMR, if nothing was done to compensate for the slow tumbling, the spectra would show a powder pattern due to the range of angles of the nuclei's orientation that would be present in the sample. However, in MAS ssNMR, these anisotropic interactions are averaged out by spinning the sample around an axis at what has been termed the "magic angle" (54.7°) with respect to the magnetic field. At this angle, the $3\cos^2\theta$-1 term equals zero (see equations above), so if the spinning rate is greater than or equal to the magnitude of the anisotropic interaction, it will average to zero. Thus, MAS ssNMR can be used to obtain high-resolution spectra of membrane proteins similar to solution NMR, which includes chemical shift assignments, torsional and distance restraints, and internal dynamics.[77,78] Together, MAS and O-ssNMR aid in determining a more comprehensive view of the structure for the protein being studied.

1.3 Chionodracine- Antimicrobial Peptide

AMPs are a fascinating class of peptides. They have been found in nearly all organisms and display an extraordinary structural and functional variety.[79] In addition to being antimicrobial, some AMPs can even regulate the immune response.[80] As such, it is

no surprise that extensive effort has been spent structurally characterizing AMPs. They consist of 10-50 amino acids[81,82] with greater than 30% of the residues being hydrophobic, but with an overall positive charge from +2 to +9.[81] The secondary structures of AMPs are usually classified into three groups: α-helical, β-sheet, or peptides with extended/random coil structure.[83-85] The α-helical peptides are commonly unstructured in solution and only adopt secondary structure upon interaction with a biological membrane.[85,86] There are several examples of this type of AMP within the piscidin family.[87-90] Their exact mechanism of action is still unclear, but it is generally thought that either they disrupt the physical integrity of the microbial membrane and/or they cross the membrane to act on intracellular targets.[81,87] This disruption of the membrane is largely driven by electrostatic forces between the negatively-charged bacterial surface and the cationic AMPs.[79,81,91] Chionodracine (Cnd) is a piscidin-like AMP from the Antarctic icefish, *Chionodraco hamatus*,[92] and in Chapter 2 of this thesis, its characterization using solution NMR and other techniques is described.

1.4 SERCA and SLN- Integral Membrane Proteins

One important system to structurally characterize is the sarco(endo)plasmic reticulum Ca^{2+}-ATPase (SERCA), and its regulators like sarcolipin (SLN). SERCA is a key component of calcium signaling, which is of crucial importance to cells as intracellular calcium (Ca^{2+}) levels impact a variety of cellular processes including autophagy, apoptosis, gene expression, cell cycle control, and cell motility.[93-95] SERCA resides in the membrane of the endoplasmic reticulum (ER) and sarcoplasmic reticulum (SR) and pumps Ca^{2+} into the organelles' lumen to maintain cytosolic Ca^{2+} levels. It is even capable

of establishing a Ca^{2+} concentration gradient of greater than 10^4- fold across the membrane.[96] The energy for this feat comes from the hydrolysis of ATP. Further underscoring its importance, SERCA is highly conserved and present among all living organisms.[97] In vertebrates, several isoforms of SERCA are expressed depending on the tissue,[97] and defects in them can lead to distinctive diseases such as Darier's disease and Brody's disease, which affect the skin and skeletal muscle, respectively.[98]

In muscle cells, Ca^{2+} cycling also controls contraction and relaxation. Depolarization of the sarcolemma activates the dihydropyridine receptor, a voltage-gated ion channel, to transport Ca^{2+} across the sarcolemma into the sarcoplasm. This causes the ryanodine receptor (Ryr) to open and release Ca^{2+} from the SR. The distinct rise in cytosolic Ca^{2+} concentration then leads to muscle contraction through the thick and thin filaments. Relaxation is induced mainly through SERCA removing the Ca^{2+} from the sarcoplasm and pumping it into the SR lumen using energy from hydrolyzing ATP (**Fig. 6**). However, the amount of Ca^{2+} SERCA removes varies with the isoforms. SERCA1a is expressed in fast-twitch skeletal muscle,[99,100] and removes 99% of the Ca^{2+} from the sarcoplasm after muscle contraction whereas SERCA2a is expressed in cardiac and slow-twitch skeletal muscle[101,102] and removes 70% of the total calcium in cardiac muscle.[103] SERCA's activity must be carefully controlled to prevent Ca^{2+} mishandling, which can be highly detrimental and lead to disease.

SERCA is regulated by interactions with peptides encoded by small open reading frames (smORFs). Until recently, the only known peptides were sarcolipin (SLN) and phospholamban (PLN), but in the last few years, more regulators of SERCA have been identified including myoregulin,[104] DWORF,[105] the sarcolambans in *Drosophila,*[106] as well as others.[107,108] Abnormal expression and mutations of SLN and PLN, respectively, can

lead to pathological conditions in humans.[109-114] Clearly, it is highly important to understand how these peptides interact with and regulate SERCA.

SLN is a 31 amino acid transmembrane peptide[115,116] that inhibits SERCA1a in skeletal muscle and SERCA2a in the cardiac muscle of the atria.[109,117,118] The interaction of SLN with SERCA decreases the rate of Ca^{2+}-dependent ATP hydrolysis and Ca^{2+}-dependent Ca^{2+} transport in vivo and in reconstituted systems.[119,120] SLN also uncouples Ca^{2+} transport and ATP hydrolysis in SERCA leading to increased heat production.[121-123] Inhibition by SLN can be reversed through phosphorylation at Thr-5 of SLN, and though the physiological role for phosphorylation of SLN is still unclear, there is evidence that preventing phosphorylation in cardiac muscle is detrimental.[124-126] Although no mutations of SLN have yet been associated with disease, the SLN and SERCA1a complex has recently received attention for its importance to metabolism and thermogenesis. In mouse skeletal muscle, SLN and SERCA1a have a profound effect on heat generation via non-shivering thermogenesis.[123,127] In fact, SLN-knockout mice were unable to maintain their core body temperatures at 4 °C and became susceptible to cold-induced hypothermia, irrespective of the presence or absence of their intrascapular brown adipose tissue.[104] These mice were also fed a high fat diet; those expressing SLN were able to compensate for the metabolic overload suggesting that the interaction between SERCA and SLN has a key role in metabolism and obesity.[104] Despite what is known about their functions, the interactions between SLN and SERCA and how they lead to inhibition and thermogenesis is not well understood.

Countless structural studies have contributed to our general understanding of integral membrane protein structure as well as the independent structures of SLN and SERCA. These studies have shown that membrane protein structures can be more

complex than originally considered. For example, helical membrane proteins were initially thought to be long, hydrophobic α-helices whose orientation was essentially perpendicular to the membrane plane.[12,128] It is now accepted that hydrophobic α-helices can cross the membrane at a variety of angles, have kinks, be interrupted in the middle of the membrane, and even cross only part of the membrane and turn back.[12] However, there are known factors that govern these structures. The residues in the middle of the membrane tend to be hydrophobic amino acids whereas the aromatic residues tyrosine and tryptophan are found near the lipid-water interface.[12,129] If the length of this hydrophobic region does not match the hydrophobic thickness of the bilayer, (referred to as hydrophobic mismatch), the helix may tilt or flex ensuring the hydrophobic region is not exposed to a hydrophilic environment,[38-41] but the rotation angle of the helix is likely unaffected.[130] However, the lipids adjusting around the protein may be the more common mechanism to compensate for hydrophobic mismatch.[36,37] Compared to helices in globular proteins, there is a higher proportion of glycines and prolines in membrane protein helices,[131,132] which along with serine, threonine, asparagine, and glutamine, can cause kinks in the helix.[133-135] Although charged and polar residues are mostly absent from the membrane region, the frequency with which positively-charged residues are found on the cytoplasmic side compared to the non-cytoplasmic side has led to this being termed the "positive-inside rule."[12,136,137] Beyond individual helices, a simplified view of the packing of adjacent helices is that their side chains fit into a knobs-into-holes geometry.[138-140] Overall, membrane protein structure is becoming less mysterious, but there is still much more to be learned.

The individual structures of SLN and SERCA have both been well studied. SLN's structure was first solved in SDS micelles, which found that SLN is helical from residues

9-27 and that the N-terminus is more disordered than the C-terminus.[141] Determination of the structure in dodecylphosphocholine (DPC) micelles revealed a nearly identical structure to the one in SDS though residues 6-27 were helical.[142] The study in DPC micelles also investigated the structural dynamics of SLN and divided it into four parts: two highly mobile termini (residues 1-6 and 27-31) and two dynamically distinct segments of the α-helix with the more hydrophilic residues (7-14, domain Ib) being less rigid than the more hydrophobic region (15-26, domain II) (**Fig. 7A**).[142] Importantly, SLN has also been characterized in several lipid environments. Glass plate samples with 4:1 1,2-Dioleoyl-*sn*-glycero-3-phosphocholine/1,2-dioleoyl-*sn*-glycero-3-phosphoethanolamine (DOPC/DOPE) showed SLN's tilt angle to be 23° ± 2°,[143] which is very similar to the tilt angle of 24° ± 1° determined for SLN in bicelles composed of DMPC/DHPC as well as DMPC+POPC/DHPC (POPC is 1-Palmitoyl,2-oleyl-sn-glycero-3-phosphocholine).[144,145] With all of this information, SLN has also been useful for method development,[144,146-149] including that described in Chapter 4 of this thesis.[71]

SERCA is one of the most well-studied membrane proteins, thus, a significant amount is known about its structure and function. SERCA is 110 kDa with 10 transmembrane helices (M1-M10) and three cytoplasmic domains: the actuator (A), nucleotide-binding (N), and phosphorylation (P) domains (**Fig. 7B**).[150] The coordinated movement of these domains allows for the transport of Ca^{2+} ions from the cytosol to the lumen in exchange for two to three protons.[151-153] The energy to pump Ca^{2+} against its concentration gradient is derived from the hydrolysis of ATP; SERCA transports two Ca^{2+} ions per ATP hydrolyzed under ideal conditions.[154-157] Structural and kinetic studies have provided an understanding of the mechanism of transport (**Fig. 8**). The Ca^{2+} ions bind to two sites within transmembrane helices M4, M5, M6, and M8.[150] In Site I, Ca^{2+} coordinates

to the side chains of Glu-771 (M5), Asp-800 (M6) and Glu-908 (M8), and with the backbone carbonyl groups from Asp-768 (M5) and Thr-799 (M6). The coordination of Ca^{2+} in Site II is with the carboxyl groups of Glu-309 (M4, bidentate coordination) and Asp-800 (M6) as well as the backbone carbonyl groups of Val-304 (M4), Ala-305 (M4), Ile-307 (M4), and Asp-796 (M6).[150] There are two main categories for the structural states of SERCA, high Ca^{2+}-affinity, E1 states and low Ca^{2+}-affinity, E2 states.[150] The transport cycle begins with cytosolic Ca^{2+} binding to the E2 state causing the release of the bound protons and SERCA's transition to the E1 state.[150] Asp-351 in the P-domain is subsequently auto-phosphorylated by the bound ATP forming the high-energy [$2Ca^{2+}$]E1~P:ADP state. This coincides with conformational changes in the A-domain, which are propagated to the transmembrane helices largely through linkers to M1 and M2 and cause the Ca^{2+} ions to become occluded. SERCA then transitions to the [$2Ca^{2+}$]E2-P:ATP state where the ADP is exchanged for ATP. The Ca^{2+} ions are de-occluded and released into the SR lumen and protons bind in exchange for these Ca^{2+} ions (H_nE2P:ATP). Dephosphorylation then occurs forming the H_nE2:ATP state and allowing SERCA to re-start the transport cycle.

Despite the volume of information known about SLN and SERCA, how their interactions lead to the inhibition and uncoupling of SERCA is not well understood. Mutagenesis studies have demonstrated that several residues within the transmembrane region of SLN can affect SERCA's maximal activity as well as its apparent calcium affinity, which have established that the transmembrane region of SLN is involved in the regulation of SERCA.[119] Recently, two X-ray structures of SLN bound to SERCA have shed more light on the interactions of the transmembrane region of SLN with SERCA and confirmed previous cross-linking and mutational studies placing SLN within helices M2, M4, M6, and M9 of SERCA.[123,158-160] And although neither study fully revealed the mechanism of

regulation, both studies were important steps in understanding the complex and provided useful information to consider for future models. Winther et al. compared the binding site of SLN observed in their crystal structure to the [H_n]E2 and [2Ca^{2+}]E1P structures.[159] As the groove where SLN binds narrows significantly from the [H_n]E2 to the [2Ca^{2+}]E1P states, the authors found it likely that SLN will be displaced or repositioned when SERCA shifts between these conformations,[159] though cross-linking studies suggest that SLN is repositioned upon Ca^{2+} binding rather than being dissociated from SERCA.[123] Toyoshima et al., on the other hand, concluded that SLN's position stabilizes an E1·Mg^{2+} state, between E2 and E1, interfering with SERCA's transition into the [2Ca^{2+}]E1 state as the movement of M2 will be suppressed.[158] Additionally, the authors noted that SLN causes the A domain to undergo a larger rotation when moving into the [2Ca^{2+}]E1 state, providing an explanation for SLN's inhibitory kinetic effects.[158] There are caveats to these findings as both of these structures were crystallized under concentrations of Mg^{2+} significantly higher than physiological levels, and even though these structures were crystallized under similar conditions (i.e., high Mg^{2+} and AMPPCP present), there are differences in the arrangement of cytoplasmic domains (the arrangement of the transmembrane helices is very similar between the two).[158,159,161] Thus, the role of the transmembrane region of SLN in regulating SERCA is not fully understood.

Although the transmembrane domain is critical for SLN's interaction with SERCA, SLN's termini also seem to play a crucial role in causing inhibition.[120] The C-terminus (referred to as the luminal tail from here on) of SLN had previously been found to be vital for proper SR retention.[162] While the luminal tail is highly conserved, especially among mammals, the N-terminus is quite variable, a difference that implies a role beyond retention.[120] In fact, individual mutations of each residue of the luminal tail to alanine result

in decreased inhibitory activity, and removing the luminal tail entirely results in a major loss of function.[120] It also seems that SLN's luminal tail is more important than its transmembrane region for inhibition, which is in contrast to PLN.[120] The luminal tail is thought to interact with the luminal end of the M2 transmembrane segment of SERCA,[120,160,163] and the M1-M2 region of SERCA is known to undergo large structural rearrangements when the enzyme transitions from the calcium-free E2 state to the calcium-bound E1 state.[150] Unfortunately, neither crystal structure of the SLN-SERCA complex shows the luminal tail clearly,[158,159] but there is evidence from ssNMR that the tyrosines of the luminal tail do interact with SERCA1a.[163] As such, it seems likely that SLN's molecular interactions with the M1-M2 region of SERCA lead to inhibition. Compared to the luminal tail, less is known about SLN's N-terminus. A recent study suggested that the N-terminus causes the uncoupling of Ca^{2+} transport and ATP hydrolysis in SERCA,[164] and corresponding molecular dynamics simulations indicated that this could be through the N-terminus' interactions with the cytosolic part of SERCA's M4 helix,[164,165] which is part of the energy transduction domain critical for coupling transport and hydrolysis.[165-170] Overall, these studies suggest that each domain of SLN contributes to its regulation of SERCA, but it is still unclear how much each domain contributes to inhibition versus uncoupling of SERCA.

Studying membrane protein structure was the central focus of the work described in this thesis. Preparing the NMR sample of Cnd in DPC micelles as described in Chapter 2 and running the initial NMR experiments taught me about how to work with membrane peptides and contributed to my understanding about how peptides interact with biological membranes. This knowledge was applied to optimizing the bicelle samples for SLN, which led to the work presented in Chapter 4 as the increased sensitivity and resolution of my

samples allowed for the development of the WESE-PISEMA experiment. Synthesizing and testing the ethylating reagent used to modify SERCA (Chapter 3), and ultimately seeing the final data regarding SERCA's cytoplasmic domains, further honed my approach to thinking about the SLN+SERCA complex. Together, the expertise I acquired from these studies was instrumental to further optimizing ssNMR samples of the SLN+SERCA complex to help discover how the transport cycle of SERCA is modified by regulators such as SLN. For example, does SLN's topology change during SERCA's transport cycle? And how do these molecular interactions lead to uncoupling in SERCA? What is the effect of phosphorylation? The data presented in Chapter 5 help to address these outstanding questions.

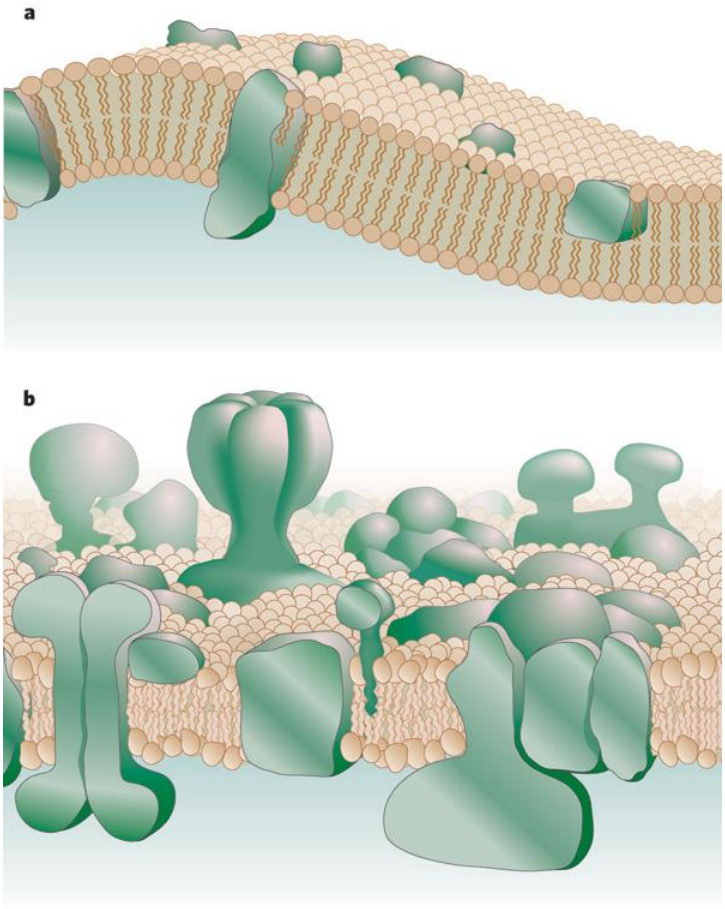

Figure 1. A) The Singer–Nicholson 'fluid mosaic model'.[28] **B)** An amended and updated version.

Reprinted by permission from Macmillan Publishers Ltd: Nature. (Engelman, D.M. Membranes are more mosaic than fluid), copyright (2005).[29]

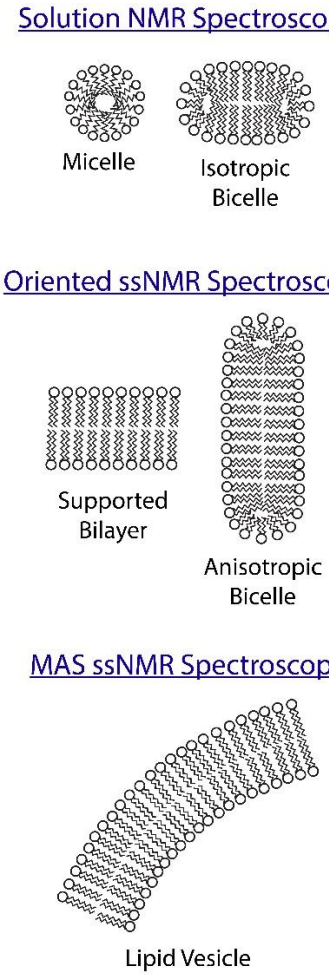

Figure 2. Membrane mimetics for solution NMR and the main solid-state NMR spectroscopy methods (O-ssNMR and MAS).

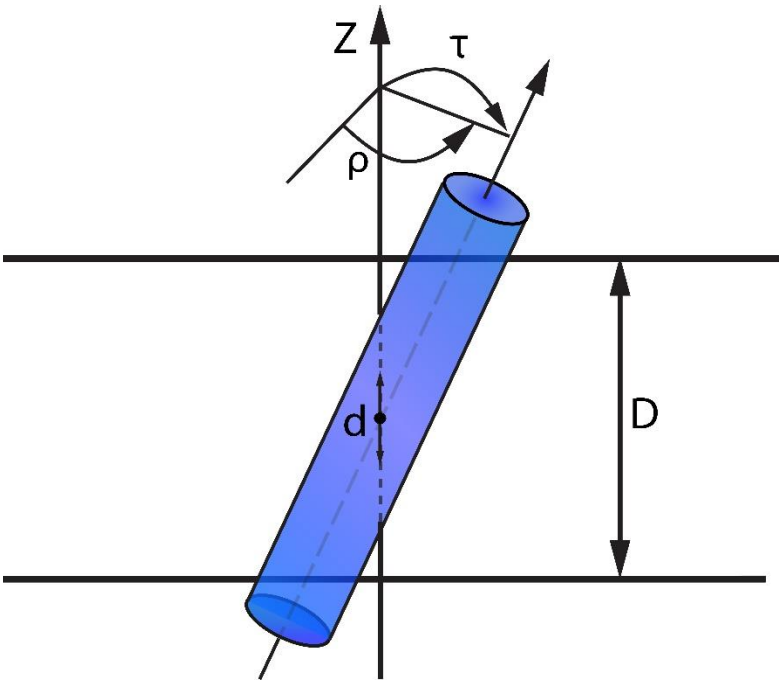

Figure 3. An α-helix in a lipid membrane showing the tilt angle (τ), rotation angle (ρ), hydrophobic thickness (D), and the shift (d) along the membrane normal (Z). The shift is related to the immersion depth of the helix within the membrane. Adapted from OPM database.[171]

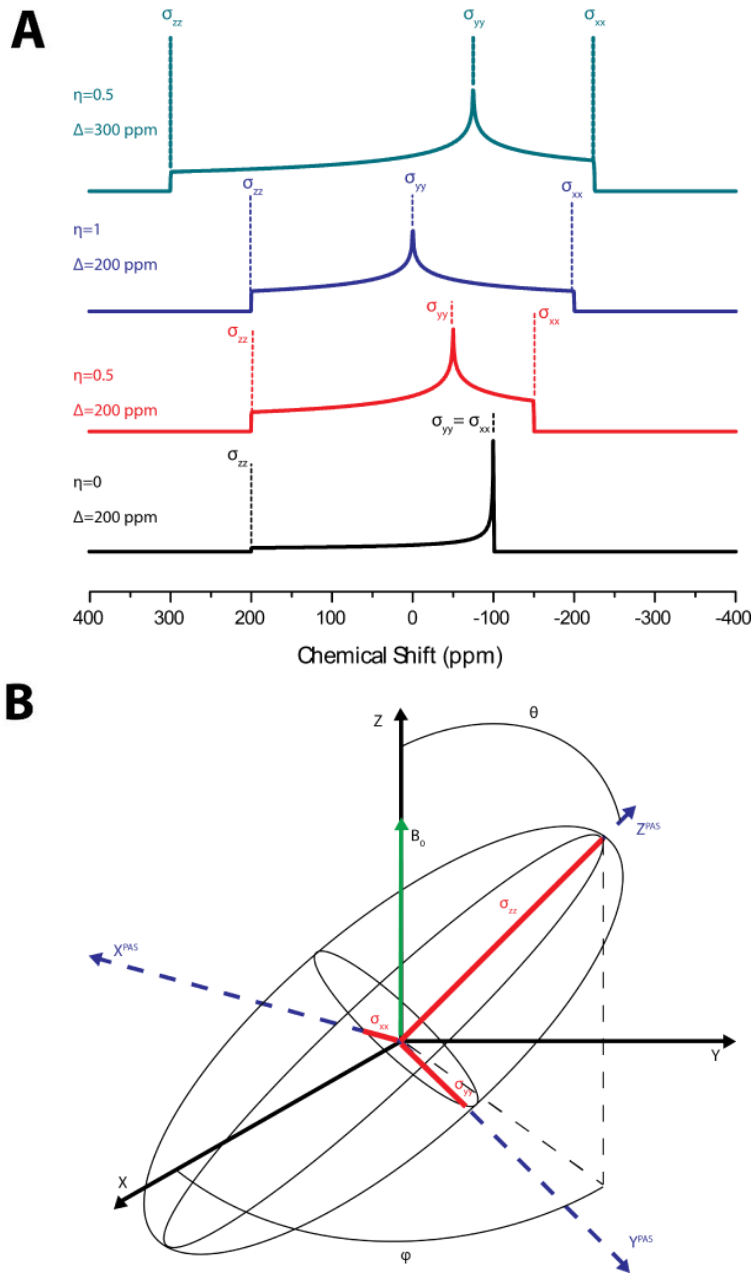

Figure 4. A) The static NMR signal is dependent on Δ and η. **B)** The principal components of the chemical shift tensor (σ_{xx}, σ_{yy}, and σ_{zz}) with the electron field surrounding the nucleus represented by the black ellipse. From: Chem LibreTexts.[69]

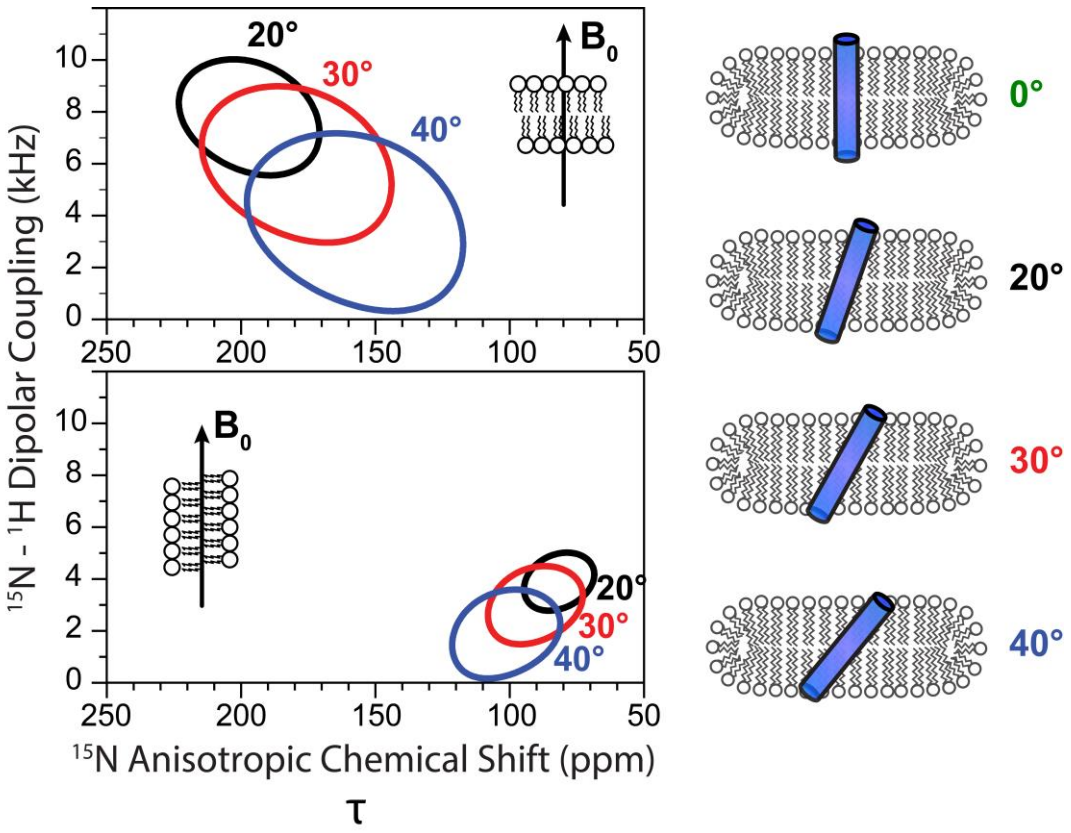

Figure 5. The PISA wheel is dependent on τ for an α-helix in flipped (top) and unflipped (bottom) bicelle samples.

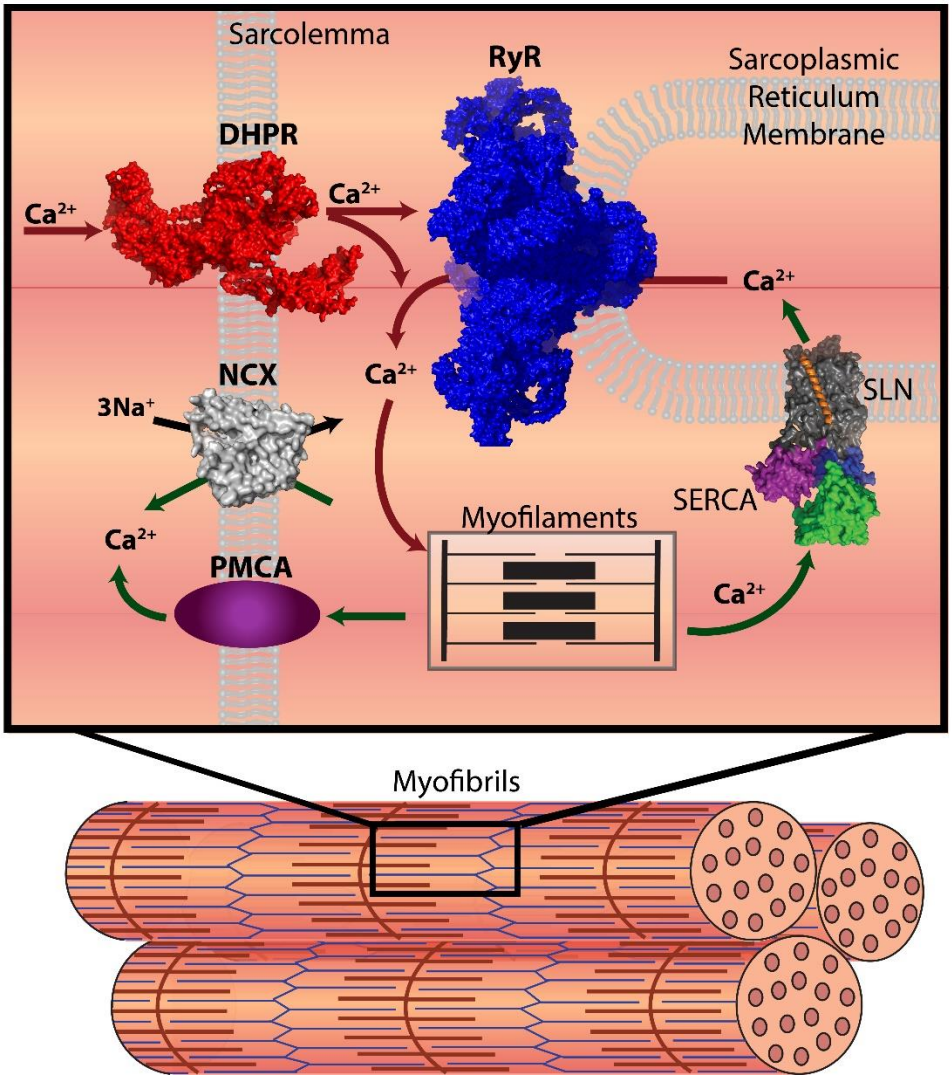

Figure 6. Schematic of a myocyte. The SR forms a network around the myofibrils, which are composed of the myofilaments.

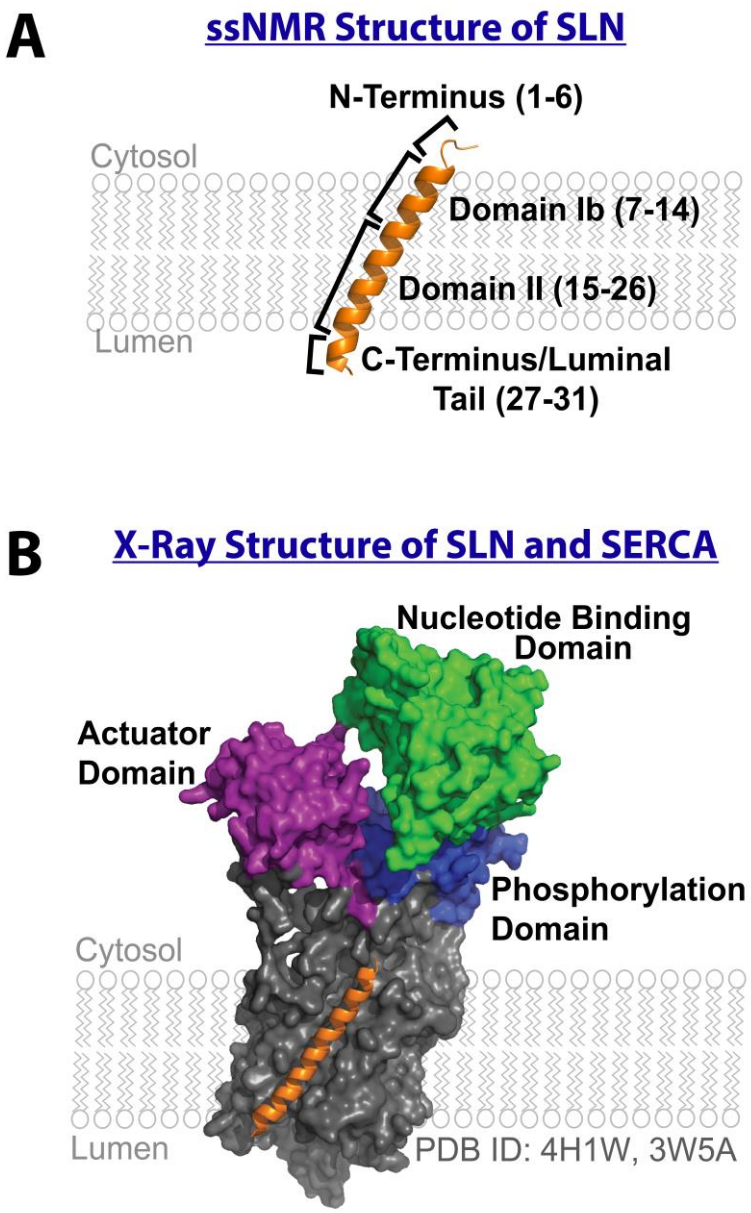

Figure 7. A) The structure of SLN with the different dynamic domains delineated. **B)** X-ray structure of SERCA with SLN (orange) bound to the transmembrane domain (gray).

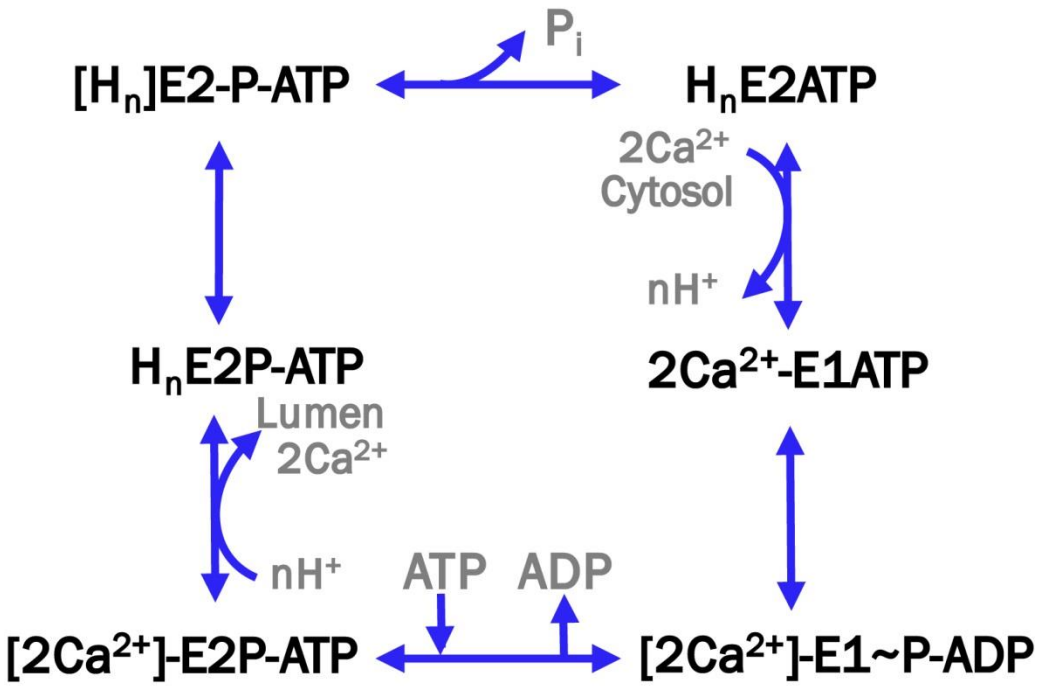

Figure 8. Schematic of SERCA's transport cycle. Adapted from Moller et al.[150]

Chapter 2 - Structure and membrane interactions of chionodracine, a piscidin-like antimicrobial peptide from the icefish *Chionodraco hamatus*

Reprinted and adapted from:

Biochim Biophys Acta, 1848(6), Cristina Olivieri, Francesco Buonocore, Simona Picchietti, Anna Rita Taddei, Chiara Bernini, Giuseppe Scapigliati, Alysha A. Dicke, Vitaly V. Vostrikov, Gianluigi Veglia and Fernando Porcelli. Structure and membrane interactions of chionodracine, a piscidin-like antimicrobial peptide from the icefish *Chionodraco hamatus*, 1285-93, Copyright (2015), with permission from Elsevier.

Abstract

Chionodracine (Cnd) is a 22-residue peptide of the piscidin family expressed in the gills of the *Chionodraco hamatus* as protection from bacterial infections. Here, we report the effects of synthetic Cnd on both *Psychrobacter* sp. TAD1 and *Escherichia coli* bacteria, as well as membrane models. We found that Cnd perforates the inner and outer membranes of *Psychrobacter* sp. TAD1, making discrete pores that cause the cellular content to leak out. Membrane disruption studies using intrinsic and extrinsic fluorescence spectroscopy revealed that Cnd behaves similarly to other piscidins, with comparable membrane partition coefficients. Membrane accessibility assays and structural studies using NMR in detergent micelles show that Cnd adopts a canonical topology of antimicrobial helical peptides, with the hydrophobic face toward the lipid environment and the hydrophilic face toward the bulk solvent. The analysis of Cnd free energy of binding to vesicles with different lipid contents indicates a preference for charged phospholipids and a more marked binding to native *E. coli* extracts. Taken with previous studies on piscidin-like peptides, we conclude that Cnd first adsorbs to the membrane, and then forms pores together with membrane fragmentation. Since Cnd has only marginal hemolytic activity, it constitutes a good template for developing new antimicrobial agents.

2.1 Introduction

Antimicrobial peptides (AMPs) represent an ancestral eukaryotic mechanism of immunity against prokaryotic organisms.[172-174] In particular, fish express a large variety of antimicrobial peptides, such as defensins, cathelicidins, hepcidins and piscidins.[92,175,176] Fish AMPs such as piscidin-2 act as anti-infective agents, and display high potency against human and fish pathogens,[177] while other peptides, such as epinecidin-1, show anticancer activity against human fibrosarcoma cells.[20]

Among the fish AMPs, piscidins constitute a rather interesting family. They are histidine- and phenylalanine-rich peptides with a broad spectrum of antimicrobial activity, and are effective against viruses, fungi and bacteria.[177] Three isoforms of piscidin have been isolated from the fish mast cells (i.e., piscidins 1, 2, and 3), differing by one or two residues.[178] Also, a new type of piscidin (i.e., piscidin-4) comprising 44 residues has been isolated and characterized from hybrid striped bass.[179] Interestingly, piscidins display in vitro anti-tumor activity against various cancer cell lines, such as HL60, HeLa[180], MCF7, and 4T1.[181] While the activity of piscidins has been attributed to their ability to form pores and disrupt cell membranes, they also have immunomodulatory properties, suggesting that they may target specific receptors.[182,183] Other reports show that piscidins may also inhibit the biosynthesis of the cell wall, nucleic acids, and proteins, or alternatively, inhibit the pathogens' enzymatic activity.[175]

We recently discovered a new antimicrobial peptide of the piscidin family named chionodracine (Cnd), which is produced by *Chionodraco hamatus*, an Antarctic teleost icefish, of the Channichthyidae family.[92] Cnd protects *Chionodraco* from infections; specifically, from the attack of *Psychrobacter* sp. TAD1 and TA144, two psychrotolerant

and psychrophilic bacteria strains typical of the Antarctic marine and terrestrial environments.[92] Cnd is expressed in the gills and head kidney of the *Chionodraco* as an 80 amino acid precursor and cleaved into a mature 22-residue peptide (*FFGHLYRGITSVVKHVHGLLSG*). We found that Cnd is active toward both *Psychrobacter* sp. TAD1 and TA144, but also shows activity toward Gram-positive *Bacillus cereus* and Gram-negative *Escherichia coli*. The minimum inhibitory concentrations (MIC) of the Cnd against mesophilic and psychrophilic bacteria have been previously reported and range between 5.00 and 20 μM.[92] Importantly, Cnd does not show any significant hemolytic activity toward human erythrocytes, with a ~ 0.8% percentage of hemolysis at 50 μM,[92] making it a promising template to develop new molecules with antimicrobial activity. Cnd's primary sequence is remarkably similar to that of other peptides belonging to the piscidin family, sharing the two N-terminal phenylalanines, the central glycine, and three histidines (**Fig. 1**). Although we have described the gene sequence, localization as well as the bactericidal activity of Cnd, we had yet to determine its interactions with prokaryotic cell membranes as well as the molecular and structural features of this peptide in membrane mimetic environments.

Here, we report the membranolytic properties and structural characterization of Cnd using transmission electron microscopy (TEM), cell permeation assays, and NMR spectroscopy. We found that Cnd interacts with cell membranes, disrupting the inner and outer membranes of both *Psychrobacter* sp. TAD1 and *E. coli* bacteria. In particular, TEM images reveal that Cnd forms well-defined pores in the bacterial membranes. Moreover, experiments carried out with synthetic membranes reveal a small but significant preference for negatively charged lipid membranes and a more marked affinity for *E. coli* bacteria membranes. The three-dimensional structure of Cnd is very similar to that of the

piscidin-1 peptide, adopting a canonical amphipathic helix, with hydrophobic amino acids adsorbed on the membrane surface and the hydrophilic amino acids pointing toward the bulk solvent. Taken together, the helical propensity (disorder to order transition), membrane binding assays, and TEM images show the formation of discrete pores as well as membrane fragmentation that enable the cellular content to leak out and killing the cells.

2.1 Materials and Methods

2.1.1 Peptide synthesis

The Cnd peptide (> 95%) *FFGHLYRGITSVVKHVHGLLSG* was purchased from United Biosystems Inc., USA. Peptide concentration was determined by light absorption at 280 nm before each sample preparation.

2.1.2 Lipid vesicle preparation

LUVs (Large Unilamellar Vesicles) of the appropriate lipid or lipid mix suspension were prepared by extrusion with an Avanti Polar mini-extruder through a polycarbonate membrane with pore sizes of 100 nm. Lipid vesicles were composed of 1-palmitoyl-2-oleoyl-sn-glycero-3-phosphocholine (POPC), mixtures of POPC and 1-palmitoyl-2-oleoyl-sn-glycero-3-phosphoglyceol (POPG), or *E. coli* B extract, ATCC 11303, comprised of 57.5% PE, 15.1% PG, 9.8% cardiolipin (CA), and 17.6% unknown (Avanti Polar Lipids Inc.). All the lipid vesicles were prepared as reported in the following sections.

2.1.3 Transmission Electron Microscopy (TEM)

Psychrobacter sp. TAD1 Antarctic bacteria were grown aerobically and cultured at 15 °C for 48 h in Luria–Bertani broth to mid-log phase (OD_{600} of 0.35), centrifuged at 3000 *g* for 10 min at 25 °C, washed and resuspended into 10 mM Tris–HCl (pH 7.4), and 150 mM NaCl (working buffer) to a final OD600 of 0.5. Treated cells were incubated with Cnd antimicrobial peptide (15 μM, PM 2424.83) while control cells were maintained in working buffer, all the groups of cells were then collected at 0, 10 and 180 min and fixed with 2% paraformaldehyde + 2.5% glutaraldehyde in cacodylate sucrose buffer (0.1 M cacodylate, 0.09 M sucrose, 0.01 M $CaCl_2$, 0.01 M $MgCl_2$, pH 6.9) containing 0.075% ruthenium red and 0.075 M lysine acetate for 20 min at 4 °C. Samples were washed in cacodylate sucrose buffer containing 0.075% ruthenium red and then fixed with 2% paraformaldehyde + 2.5% glutaraldehyde in cacodylate sucrose buffer containing 0.075% ruthenium red overnight at 4 °C. After washings in the cacodylate sucrose buffer containing 0.075% ruthenium red, samples were post-fixed in 1% OsO4 + 0.075% ruthenium red in 0.1 M cacodylate buffer at pH 7.2 for 1 h at room temperature and then washed again in the cacodylate sucrose buffer containing 0.075% ruthenium red. Specimens were dehydrated in a graded ethanol series and embedded in LR White resin (Multilab Supplies, Surrey, England).[184] The resin was polymerised in tightly capped gelatine capsules for 48 h at 50 °C. Thin sections were cut with Reichert Ultracut and LKB Nova ultramicrotomes using a diamond knife, collected on copper grids, stained with uranyl acetate and lead citrate, and observed with a JEOL 1200 EX II electron microscope at 100 kV. Micrographs were acquired by the Olympus SIS VELETA CCD camera equipped the iTEM software. TEM images (at the same magnification) were analysed to determine the percentage of damaged bacteria (bacteria with destroyed membranes) both

in controls and treated cells, by counting a total number of 50,000 cells. All the numerical results are presented in the text as mean ± SD. Homogeneity of variances was tested before data processing. To detail the source of variation attributed to treatment and time factors, two-way ANOVA was applied, followed by Bonferroni's test. Data were analysed using the GraphPad Prism 3.0 software statistical package. The level for accepted statistical significance was $P < 0.01$.

2.2.4 Steady-state fluorescence experiments

Partition Studies

A Perkin Elmer LS55 steady-state fluorescence spectrometer was used for steady-state fluorescence measurements. The experiments were carried out at 25 °C in a thermostated cell holder equipped with magnetic stirrer. In order to correct for polarization effects and reduce direct contributions from the vesicles, light scattering measurements were carried out with a cross-oriented configuration of polarizers (Pol_{em} = 0° and Pol_{exc} = 90°).[185] The partition of Cnd with lipid vesicles was quantified by titrating the peptide samples in 20 mM phosphate buffer at pH 7.4 containing EDTA 0.8 mM and NaCl 150 mM with increasing amounts of vesicle stock solutions; the lipid/peptide ratio ranged from 50 to 500. These binding assays were repeated with LUVs of different compositions: 100% POPC, 70%/30% POPC/POPG, and *E. coli* B extract. The lipid titrations were monitored following the increase of Tyr-6 fluorescence at λ_{em} = 320 nm upon excitation at λ_{exc} = 274. The background signals of both buffer and lipid vesicles were subtracted from each spectrum. The partition constant K_x, was defined according to Wimley and White:[186,187]

$$K_x = \frac{[P]_{bil}/[L]}{[P]_{water}/[W]}$$

where $[P]_{bil}$ and $[P]_{water}$ are the bulk molar concentration of peptide in the bilayer and in the water, and *[L]* and *[W]* are the molar concentrations of lipid and water, respectively. The partition constants were measured by titrating a 1 μM solution of Cnd with increasing amounts of lipid vesicles of varying compositions, then calculating the fraction of the peptide, f_p, partitioned into the lipid vesicles. Considering that $[P]_{tot} = [P]_{water} + [P]_{bil}$[188,189] the expression for f_p is:

$$f_p = \frac{K_x[L]}{[W] + K_x[L]}$$

The values of K_x were determined by the plot of f_p vs *[L]* using the GraphPad Prism 6 software package (GraphPad Software Inc.). Experimental data were fitted using equation:[188]

$$\frac{F}{F_o} = 1 + (F_{\max} - 1) f_p$$

where F is the fluorescence intensity, F_o and F_{max} are the fluorescence intensities before lipid vesicle addition and at saturation, respectively. In order to avoid the non-ideal behavior occurring at higher concentrations,[187,190] the molar partition coefficients were evaluated at a low peptide concentration (~ 1 μM).

Outer membrane disruption assay

For cell permeabilization studies, we used ANS (1-aminonaphtalene-8-sulfonic acid) uptake assays[191] with *E. coli* BL21(DE3) and *Psychrobacter* sp. TDA1 bacteria. Bacterial cells were cultured in LB medium. Cells from the mid-log phase were centrifuged,

washed, and then resuspended in PBS buffer to achieve an OD_{600} of ~ 1.2. Increasing amounts of peptide (ranging from 1.0 to 15.0 μM) were added to 1.0 mL of cell suspension in the presence of 5.0 μM of ANS. The spectra were recorded between 400 and 600 nm with an excitation wavelength of 360 nm and excitation/emission band-passes of 5.0 nm. The disruption of the outer membrane was quantified by the increase in fluorescence intensity and the blue shift of the spectra.

Calcein leakage studies

The kinetics of calcein release were followed by monitoring the fluorescence increase upon peptide binding to vesicles at different lipid compositions. LUVs charged with 50 mM calcein were prepared by an extrusion process. Briefly, the appropriate amount of lipids was dissolved in chloroform in a small round bottom flask and the solvent was gently removed in a rotary evaporator. The remaining solvent was removed under vacuum overnight at room temperature. The dried lipid films were hydrated with MOPS buffer at pH 7.5 containing 70 mM NaCl, 0.8 mM EDTA, and 50 mM calcein. The lipid suspensions were vortexed at room temperature and subjected to 5 freezing and thawing cycles. After freezing, the sample was heated to 50 °C and the mixture subjected to extrusion cycles using an Avanti polar mini-extruder containing two stacked 100 nm polycarbonate filters. To separate the non-encapsulated calcein in the external medium, the mixture was passed through a Sephadex-G50 column. Columns containing the calcein-loaded vesicles were centrifuged for 3 min at 1000 rpm. The lipid concentration was measured via the static light scattering at 90° of the lipid suspension at 550 nm and compared with a calibration curve.[192] The Bartlett method was used to determine the total phospholipid concentration. Fluorescence studies were carried out at 25 °C with an

excitation wavelength of 490 nm, producing an emission wavelength of 520 nm. The excitation and emission band-passes were 2.5 nm. LUVs charged with 50 mM calcein showed very little fluorescence quantum yield due to calcein self-quenching. The increase in observed fluorescence was due to the vesicle leakage caused by peptide addition. Before peptide titration (from 0.1 to 1.0 μM), the fluorescence baseline was monitored for 5 min and no deviations were observed. After peptide addition, the fluorescence was monitored up to 2000 s. To obtain the maximal leakage of the vesicles and normalize fluorescence intensities, we added ~ 5 μL of 0.1% solution of Triton X to each sample. Before each measurement, we performed light scattering experiments between 540 and 560 nm to assess the integrity of the vesicles.[192] Fluorescence traces were fitted with a double exponential equation:[192]

$$F_t = F_{eq} - a_1 e^{-k_1 t} - a_2 e^{-k_2 t}$$

where F_t and F_{eq} are the fluorescence at time t and at $t \rightarrow \infty$, respectively, the constants a_1 and a_2 represent the fractions of the two kinetic components and k_1 and k_2 are the respective constants expressed in s^{-1}. The percentage of calcein release was calculated using the formula:

$$Dye\ release(\%) = \frac{F - F_0}{F_t - F_0}$$

where F is the fluorescence upon addition of peptide, F_0 is the initial fluorescence before the addition of peptide and F_t is the fluorescence upon addition of Triton-X.

Iodide quenching experiments

Quenching of the tyrosine fluorescence both in the presence and absence of lipid vesicles was measured by addition of increasing aliquots of potassium iodide.[193] The excitation wavelength was set to 274 nm and florescence spectra were recorded between 295 and 360 nm. Fluorescence spectra were corrected for dilution and for the absorption of fluorophores and quenchers. The data were fitted according to the Stern–Volmer equation:

$$\frac{F_o}{F} = 1 + K_{SV}[Q]$$

where F_o and F are the fluorescence in the absence and presence of the quencher Q, respectively, and K_{SV} is the Stern–Volmer constant accounting for the collisional quenching process.[194]

NMR sample preparation and spectroscopy

The lyophilized peptide was dissolved in an aqueous solution (5% ^2H_2O, 95% H_2O) containing 300 mM perdeuterated DPC (Cambridge Isotope Laboratories) and 20 mM phosphate buffer at pH ~ 6.5 to a final concentration of ~ 1.5 mM. All of the NMR experiments were acquired at 300 K on a Varian Inova 900 MHz spectrometer. The 2D [^{1}H, ^{1}H] total correlation spectroscopy (TOCSY)[195] (50 and 70 ms mixing time) and 2D [^{1}H, ^{1}H] NOESY[196] (70–300 ms mixing time) experiments were run in the phase-sensitive mode using time-proportional phase incrementation (TPPI) for quadrature detection in the indirect dimension. All of the pulse sequences utilized a WATERGATE pulse scheme[197] for solvent suppression. The experiments were acquired with 256 and 1024

complex data points in the t_1 and t_2 dimensions, respectively, with 64 scans per increment. The 90° pulse width was 30 kHz, and recycle delay was set to 1 s. A DIPSI-2 pulse sequence[198] was used for isotropic mixing in the 2D TOCSY experiments. The spectral widths were 5400 Hz t_1 and 7200 Hz t_2 dimensions. The 2D data were zero-filled to 8192 points in t_1 and to 4096 points in t_2 and then processed with a sine-bell squared window function shifted between 60° and 90° before Fourier transformation. A polynomial function was used for baseline correction in the direct frequency dimension. The NMR data were processed using *NMRPipe*[199] and analyzed with *SPARKY*[200] software packages. Proton dimension was referenced to the water line at 4.7 ppm. The spectra were assigned using the standard assignment approach described by Wuthrich.[201] [^{1}H,^{13}C] HSQC and HMBC spectra were acquired on a Bruker 900 MHz spectrometer at 30 °C. All the ^{13}C experiments were carried out at natural abundance. Analysis of the natural abundance of ^{13}C edited HSQC and HMBC has been used to resolve amino acid spin system assignments as well as provide $^{13}C_\alpha$ and $^{13}C_\beta$ chemical shifts. A table with all of the ^{1}H chemical shift resonances is provided in the supporting information.

Structure calculations from NMR data

NOE cross-peaks from the 150 and 300 ms mixing time [^{1}H, ^{1}H]-NOESY experiments were integrated and used for the structure calculations. The NOE volumes were calibrated using the average NOE volume from resolved aromatic vicinal protons of Y6 and classified as strong, medium, and weak, corresponding to distance restraints of 1.8–2.9, 1.8–4.5, and 1.8–5.0 Å, respectively. *TALOS* + software[202] was used to obtain the dihedral constraints for residues 3 through 19 that were then implemented in the structure calculations. The NMR conformers were calculated starting from an extended

conformation of Cnd and minimized using a hybrid simulated annealing (SA) energy minimization protocol available in XPLOR-NIH[203]. A total of 100 conformers were generated using random seeds at an initial temperature of 5000 K with 6000 high temperature steps, 3000 cooling steps, and a step size of 5 fs. The final target function included a total of 240 NOEs (75 intra-residue and 165 inter-residue distances). The final stage of refinement of the structural ensemble was carried out starting at an initial temperature of 500 K and using 30,000 cooling steps with a 1 fs step size. The 70 refined structures had no NOE violations greater than 0.5 Å, no bond violations greater than 0.05 Å, and no bond angle violations greater than 4°. The 40 lowest energy conformers were then selected for further analysis. The analysis of Ramachandran angles for the 40 lowest energy structures was carried out using Molprobity[204]. For the final conformers, the occurrence of the ϕ and ψ angles for all of the residues in the Ramachandran plots was 83.6% in the most favored region, 11.1% in the allowed, 1.6% in the generously allowed, and 3.7% in disallowed regions. The residues located in the N- and C-termini, which had fewer structural restraints, account for those found in the disallowed regions of the Ramachandran plots.

2.3 Results

2.3.1 Effects of Cnd on the inner and outer membranes of Psychrobacter sp. TAD1 bacteria using transmission electron microscopy (TEM)

Examination of the *Psychrobacter* sp. TAD1 by TEM (**Fig. 2A**) revealed that the bacterium is bounded by two membranous structures. These two membranes, the inner membrane (IM) and the outer membrane (OM), are separated by a gel-like layer known as the periplasm (**Fig. 2B**). A large number of spherical structures, resembling the outer

membrane vesicles (OMVs) of Gram-negative bacteria, were found in the extracellular matter, mainly interspersed among cells. A process of bulging out and pinching off of a portion of the bacterial OM, which plays a dynamic role in the formation of OMVs, was noticed in many cells (**Fig. 2A; C**). The formation of OMVs is a common feature of cold-adapted bacteria that utilize these extracellular vesicles for sensing nutrients.[205]

Compared to control, treatment of *Psychrobacter* sp. TAD1 bacteria with the Cnd peptide (10–80 min) induced a significant increase ($P < 0.01$) of the number of cells with membrane damage (**Fig. 3**).

After 10 min of treatment Cnd perforated both OMs and IMs, with the consequent loss of intracellular components (**Figs. 2D** and **E**). Interestingly, this process is localized in well-defined areas, suggesting the formation of well-defined pores (**Fig. 2E**). After 180 min of treatment we observed no further increase of damaged bacteria (**Fig. 3**). Cnd also damaged the cell membranes of dividing cells, with leakage of cellular contents and breakup of the basic cellular structure (**Fig. 2F**). In the extracellular matter were observed fragments of destroyed cellular membranes, whose contents were lacking (**Fig. 2G**). The morphology of the cellular damage and the time course of the process suggest that Cnd might aggregate on the cell surface, forming well-defined pores together with membrane fragmentation. Discrete pores have been observed for the antimicrobial peptide piscidin-1.[175]

2.3.2 Outer membrane permeability assay

To compare the ability of Cnd to damage the integrity of the outer membrane of *Psychrobacter* sp. *TDA1* and *E. coli* bacteria, we used the ANS (1-aminonaphtalene-8-

sulfonic acid) fluorescence assay.[191] Because of its hydrophobic nature, ANS is not able to pass the cell wall of either *Psychrobacter* sp. *TAD1* or *E. coli*, giving rise to a weak fluorescence signal caused by the high polarity of water. Upon titration of the bacteria cells with Cnd, ANS penetrates the cell membranes, causing a drastic increase of its fluorescence accompanied by a blue shift of the band (**Fig. 4**). This dose-dependent effect is notable at concentrations as low as 1 μM for both *Psychrobacter* sp. and *E. coli* bacteria, confirming our previous data from the antibacterial activity assays.[92]

2.3.3 Membrane partition of the chionodracine peptide

To quantify the interaction of Cnd with membrane mimetic systems and assess the effects of lipid charges, we measured the fluorescence emission of Tyr-6 of Cnd upon partitioning within membranes of different compositions. **Figure 5** shows the binding isotherms for Cnd upon addition of increasing amount of lipid vesicles.

The mole fraction partition coefficients K_x obtained from the curves ranging from 3×10^4 to 2×10^5 are reported in **Table 1**. The calculated Gibbs free energies of the water/bilayer partition are − 25.6 kJ/mol for pure POPC, − 26.5 kJ/mol for the POPC/POPG mixture, and − 29.9 kJ/mol for the *E. coli* lipid extract. From these data, it is possible to see a small but significant increase of K_x value using the POPC:POPG mixture. The higher propensity to partition in native *E. coli* lipid extract can be explained by both charge effects and other constituents such as phosphatidylethanolamine (67% wt/wt) and cardiolipin that may anchor the peptide to the membrane. Analogous results have been reported by Vogel and co-workers for indolicin and tritrpticin in interaction with model and natural membranes.[206]

2.3.4 Calcein release studies

Membrane permeabilization by Cnd was also studied by monitoring the increase of calcein fluorescence upon addition of peptide. As calcein has excitation and emission wavelengths of 490 nm and 520 nm, respectively, its leakage from POPC, POPC/POPG (70/30 wt/wt) and *E. coli* extract LUVs was measured as a function of time at different peptide concentrations ranging from 0.1 to 1.0 μM. When a high concentration of calcein is present in the LUVs, the fluorescence is self-quenched. After addition of Cnd to the calcein-loaded vesicles, a gradual release of calcein induced by the peptide/lipid bilayers interaction is observed. To confirm that calcein release was due to vesicle/peptide interaction and not to vesicle rupture, the integrity of the lipid vesicles was determined by right angle light scattering. In **Table 2**, the relative leakage capabilities of Cnd with different liposome vesicles are reported as function of lipid/peptide ratio. We employed POPC vesicles, negatively charged vesicles containing POPC/POPG (70/30 w/w) to simulate bacterial cell membranes, and *E. coli* extract vesicles. The relative percentage of leakage shows that the dose-response of Cnd-induced calcein leakage is more effective in the presence of negatively charged membranes, especially at a low peptide/lipid ratio. The minor leakage capability observed for *E. coli* lipid extract was also reported by Vogel et al.[206] for tryptophan rich cathelicidin antimicrobial peptides; this was attributed to the complexity of the *E. coli* extract making vesicles less prone to disruption.

We also examined the kinetics of leakage using a method developed by Tatulian and co-workers.[192] **Figure 6** shows the fractional release of calcein from a solution containing 25 μM of POPC/POPG vesicles as an example of peptide-induced calcein release. Upon addition of the peptide, a gradual increase of fluorescence due to calcein release is observed until fluorescence reaches the equilibrium, F_{eq}.

The values of the kinetic parameters accounting for the fast and the slow components of the process are reported in **Table S1**. The kinetic constants depend on the membrane charge and peptide concentrations and range from 0.2–2.0 min and 7–59 min for the fast and the slow components.

2.3.5 Fluorescence quenching experiments

The degree of peptide exposure to the bulk solvent was assessed through Tyr-6 fluorescence quenching experiments using iodide ions as a quencher.[194] **Figure 7** shows the Stern–Volmer plots for iodide quenching of Cnd in the absence and presence of POPC, POPC/POPG and *E. coli* extract.

The data are corrected for both dilution and absorption of fluorophores. The iodide quenching curves follow a linear correlation with the KI concentration, indicative of collisional quenching. The K_{SV} values, obtained from the slopes of the curves and accounting for the dynamic quenching, are reported in **Table 3**.

As expected, the K_{SV} values of are higher in buffer solution ($K_{SV} \approx 10\ M^{-1}$) than in the presence of vesicles ($K_{SV} \approx 3\ M^{-1}$), with the slopes determined in the presence of vesicles ~3–6 fold smaller than in buffer only. This implies that Tyr-6 has a higher accessibility to solvent in the absence of lipid membranes, and suggests that Tyr-6 partitions at the interfacial region of the lipid bilayer. As for the partition constant, the quenching experiments show that the peptide interacts more strongly with charged lipids and with native *E. coli* membranes than with POPC.

2.3.6 NMR studies of chionodracine in micelles

For the structural studies, Cnd was reconstituted in DPC micelles.[207-209] Sequence specific resonance assignments were obtained by a combination of 2D [^{1}H–^{1}H]-TOCSY and [^{1}H–^{1}H]-NOESY spectra. From these spectra, we assigned most of the resonances and NOE connectivities. Due to slow tumbling of the peptide in micelles, we were not able to measure the J coupling constants.[207-210] The complete resonance assignment is given in **Table S2**. In the TOCSY experiment, we were able to assign most of the fingerprint region containing H_α–H_N cross-peaks. However, only a few spin systems show correlations between the amide and the side chains due to the inefficient relay of magnetization. The peptide spin system assignment was achieved following the NOESY-walk method reported by Wuthrich.[201] From the analysis of the NOESY spectra at 300 ms, a total of 240 NOEs (75 intra-residue and 165 inter-residue) were assigned. **Figure S3** shows the summary of NMR data and NOEs connectivities obtained for the fingerprint region H_α–H_N, the backbone NOE patterns, and the chemical shift index for H_α.[211] We assigned several d_{NN} (i,i + 1) and $d_{\alpha N}$ (i,i + 1) along the peptide backbone, as well as dαN (i,i + 2). Connectivities diagnostic of an α-helical conformation, such as $d_{\alpha N}$ (i,i + 3), $d_{\alpha N}$ (i,i + 4), d_{NN} (i,i + 3) and $d_{\alpha\beta}$ (i,i + 3), were detected along the entire peptide backbone, especially in the region between residues 5 and 20. From the analysis of the natural abundance ^{13}C-edited HSQC, we were able to resolve the amino acid spin system and assign C_α and C_β for the different residues. NMR chemical shifts are strongly related to the secondary structure of proteins and peptides and can be used to calculate the structures.[211,212] To obtain Cnd peptide backbone torsion angles, we input the chemical shifts into TALOS+.[202] **Figure S4 (C)** reports the RCI-S2, Random Coil Index derived order parameter S2,[212] predicting protein flexibility, and the ANN-predicted secondary structure

calculated from backbone chemical shifts of H_α, H_N, C_α and C_β using TALOS+.[202] According to this method, RCI-S2 values less than 0.5 indicate dynamic residues. In **Figure S4**, the bar length is proportional to the probability of the residues to be in either a helix (negative values) or beta-sheet (positive values) conformation. For the Cnd peptide, the average order parameter for residues 5–20 is ~ 0.8, except for the C-terminal region, which is predicted to be disordered. The conformers obtained from the XPLOR-NIH calculations[203] confirmed this prediction. **Figure 8** displays the superposition of the 40 lowest energy conformers obtained from the structure calculations as well as the average structure. As shown in **Figure 8**, the well-defined ensemble is arranged in an α-helical conformation between residues 5 through 20, featuring a classical amphipathic α-helix.

The superposition of backbone atoms between residues H4 through L20 gives a RMSD of 0.30 ± 0.17 Å, and a RMSD of 0.92 ± 0.28 Å for the heavy atoms. From the analysis of the amphipathic helix, there is evidence that hydrophobic residues are on the face of the peptide that is likely closest to the lipid bilayer. The statistics for the 40 best NMR structures of Cnd in DPC micelles are reported in **Table S3**.

2.4 Discussion and conclusion

Interest in studying AMPs has grown significantly in recent years due to the fact that increasing bacterial resistance to conventional antibiotics is becoming a global emergency.[26,27] The majority of AMPs share the ability to kill a broad spectrum of prokaryotic cells by interacting with and disrupting bacterial cell membranes.[21,213-215] In addition, several AMPs are involved in modulating immune and inflammatory responses.[216,217] AMPs' broad spectrum of activity, as well as the obstacles they present

to the development of resistance, makes them an important candidate for a valid alternative to conventional antibiotics.[25] In fact, some AMPs are already used, in drug formulation, to topically treat infections.[26] Recent studies, reviewed by Hancock, show that AMPs also have immunomodulatory properties.[217]

Generally, AMPs such as piscidins are cationic, small (15–45 residues), and amphipathic, with about 50% of their residues hydrophobic to facilitate the interaction with cell membranes.[218,219] Since the first antimicrobial peptide, nisin was isolated in 1947, more than 1800 AMPs have been identified, some natively expressed and others synthesized and tested against different microorganisms.[220] Unfortunately, a unified mechanism of action of AMPs has not yet been found. The only way to understand their biological function is to combine functional assays with detailed structural studies.[207-209,221,222]

Peptides derived from fish are attracting growing attention, as they are active at high salt concentrations and a wide range of temperatures, making them ideal candidates for antimicrobial drugs. Pardaxin from Moses sole (*Pardachirus marmoratus*) was the first fish antimicrobial peptide to be discovered and characterized.[207,223] Thereafter, many peptides showing a broad-spectrum of antimicrobial activity were isolated from fish, such as misgurin from the loach *Misgurnus anguillicaudatus,*[224] pleurocidin from winter flounder (*Pleuronectes americanus*),[225] and piscidins from hybrid striped bass (*Morone chrysops* female and *Morone saxatilis* male).[178]

The TEM images show the formation of distinct pores (35–50 nm in diameter), highly localized at possible points of peptide aggregation. This mode of permeabilization supports the macroscopic current and single-channel measurements carried out by

Campagna and co-workers on piscidin-1,[175] supporting the formation of discrete pores. Moreover, the presence of completely fragmented membranes suggests a carpet-like mechanism of action for Cnd. However, Cotten and coworkers emphasize for piscidins 1 and 3 that is difficult to discern between these two mechanism suggesting the carpe model as an extension of pore mechanism.[87] The affinity for synthetic bilayers, quantified via the intrinsic fluorescence quantum yield of the native Tyr-6 of Cnd, shows that the peptide has a piscidin-like behavior with the cationic residues preferentially targeting negative charged lipid membranes. As with the other piscidins, Cnd undergoes a disorder-to-order transition into a well-defined amphipathic α-helical conformation. The amphipathic α-helix motif is a relevant and well-known membrane-binding motif in which both hydrophilic and hydrophobic sites are involved in membrane binding. For instance, an amphipathic helix form from residue 2 through 22 has also been found for the 22 residue analog peptide piscidin-1 in SDS micelles.[226] The presence of an amphipathic helix for the analogues piscidin-1 and piscidin-3 has been confirmed by ssNMR studies in lipid bilayer.[87,88,90] Using ssNMR spectroscopy and MD simulation, Cotten and co-workers[87] showed that piscidin-1 and piscidin-3 insert and rotate in the bilayer; furthermore, due to the presence of the aromatic residues at the N-terminus, it is more deeply inserted in the bilayer than the C-terminus. For Cnd, NMR derived structures (**Fig. 8**) indicated that Cnd interacts with the lipid membrane so that the non-polar face is in contact with the hydrophobic portion of the membrane and the polar residues are oriented toward the solvent.[227] This evidence is also confirmed by the Tyr-6 quenching studies. As reported in **Table 3**, Tyr-6 is much less accessible to the solvent upon binding with lipid vesicles, and the Stern–Volmer constant is 3–6 fold smaller, depending on the vesicles, than in buffer. The decrease in accessibility of the fluorophore to the quencher can be explained by the fact that, upon binding, the N-terminus is deeply inserted into the lipid bilayer due to the presence of the two

phenylalanine residues in positions 1 and 2. Moreover, the presence of anionic lipids lowers the Gibbs partition energy by about 4 kJ/mol moving from the zwitterionic POPC to the anionic mixture (POPC/POPG 70:30). We speculate that following binding to the membrane surface, there is a perturbation of the lipid membrane and the formation of pores and membrane fragmentation that concur to the leakage of the cell content. To this extent, leakage measurements reveal the ability of Cnd to induce calcein release from lipid vesicles in a dose-dependent manner, based on both peptide-to-lipid ratio as well as the type of lipids used (**Fig. 4**). The efflux rates increase in the presence of a higher peptide/lipid ratio and in the presence of anionic lipids, likely as a consequence of better binding, as confirmed by higher values of K_x. At low peptide to lipid ratios the induced leakage is low, while upon increasing this ratio the leakage also drastically increases.[193]

In conclusion, the combination of TEM, fluorescence data, solution NMR spectroscopy, and lipid binding assays of Cnd support a mechanism of action in which the mature peptide is essentially unstructured and adopts a canonical α-helical structure upon interaction with lipid membranes, with a preference toward charged lipids and *E. coli* extracts. The TEM images and the NMR data suggest that the initial adsorption of the peptide on membranes is followed by the recruiting of other monomers, forming well-defined pores that perforate both inner and outer membranes. The latter mechanism occurs together with an extensive membrane fragmentation that concurs to killing bacterial cells. Given the weak hemolytic activity of Cnd, these data suggest that this peptide could constitute a great starting point for the development of more specific and potent antimicrobial agents.

Figure 1. Primary sequences for Cnd and other piscidin antimicrobial peptides with sequence homology highlighted.

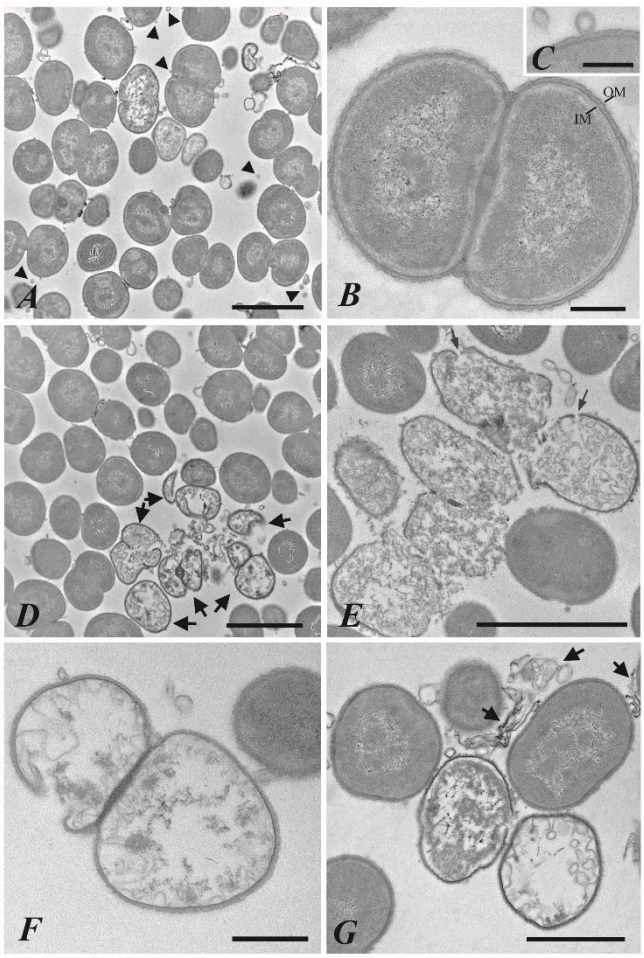

Figure 2. TEM micrographs of ultrathin sections from *Psychrobacter* sp. TAD1. (**A**) General view of cells showing the OMVs interspersed among bacteria (arrow heads). (**B**) Magnified view of cells surrounded by two membranous structures: the inner membrane and the outer membrane. (**C**) Image showing the OMVs protruding from the bacterial outer membrane. (**D**) Bacteria showing membrane damage after 10 min of treatment (arrows). (**E**) Higher magnification of damaged bacteria showing discrete pores (arrows) together with membrane fragmentation. (**F**) Dividing cells with leakage of cellular contents after 10 min of treatment. (**G**) A detail of fragments of destroyed cellular membranes (arrows) after 10 min of treatment. IM: inner membrane; OM: outer membrane. Scale bar: 2 μm in (**A**); 250 nm in (**B**); 250 nm in (**C**); 2 μm in (**D**); 2 μm in (**E**); 500 nm in (**F**); 1 μm in (**G**).

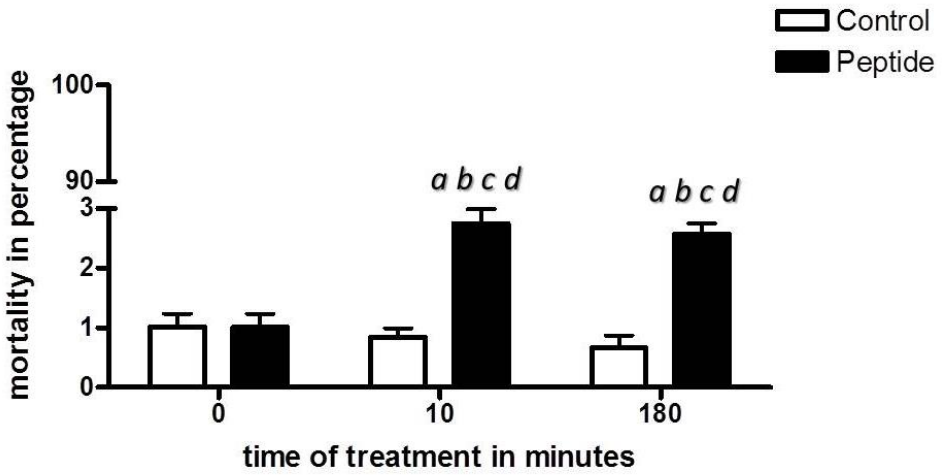

Figure 3. Percentage of *Psychrobacter* sp. TAD1 damaged bacteria. TEM images were analyzed to determine the percentage of mortality both in controls and treated cells (at the same magnification), by counting a total number of 50,000 cells. Data were collected at different times (0, 10 and 180 min in) and only cells with completely fragmented membranes were considered. Numerical results are presented as mean ± SD. The level for accepted statistical significance was $P < 0.01$. Significantly different ($P < 0.01$) from: (*a*) peptide 0 min, (b) control 0 min, (c) control 10 min, and (d) control 180 min.

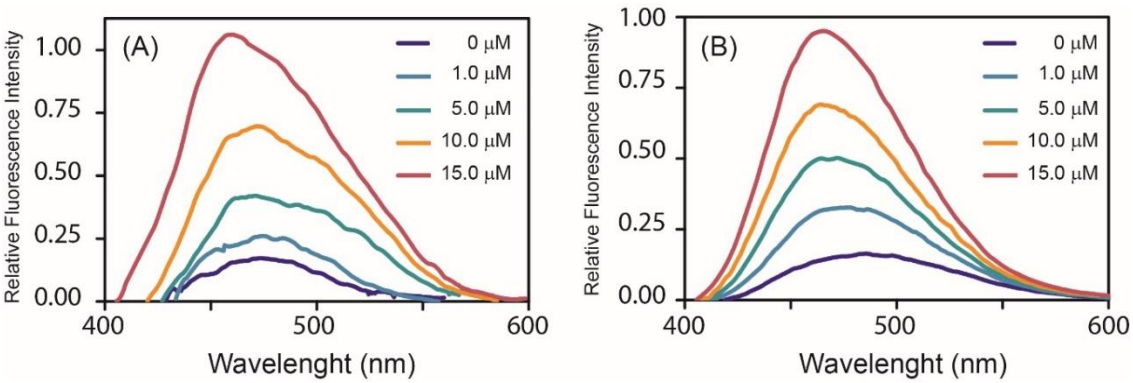

Figure 4. Permeabilization of *E. coli* (**A**) and TAD1 (**B**) outer membrane by Cnd. Fluorescence of ANS equilibrated with cells and in the presence of increasing amount of Cnd peptide from 1.0 through 15 μM. The cell density measured at OD_{600} was 1.2.

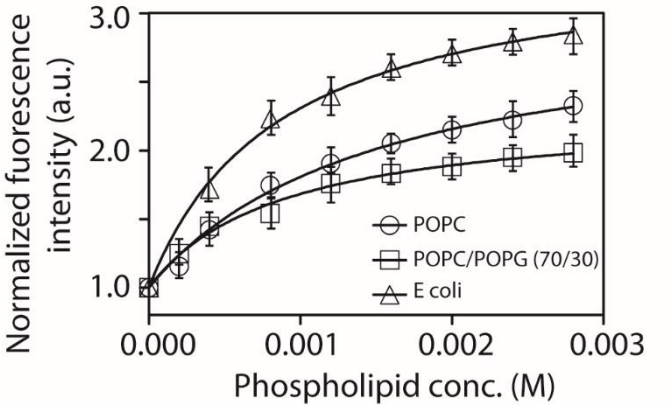

Figure 5. Binding isotherms for Cnd upon addition of increasing amount of lipid vesicles. The concentration of peptide was 10.0 μM.

Peptide Concentration	Lipid Composition	K_x	ΔG (kJ/mol)
1.0 μM	POPC	$(3.43 \pm 0.26)\times10^4$	-25.9
	POPC/POPG (70/30 w/w)	$(4.91 \pm 0.29)\times10^4$	-26.7
	Total *E. coli* extract	$(1.83 \pm 0.08)\times10^5$	-30.0

Table 1. Partition parameters for Cnd in the presence of different mixtures of POPC/POPG and *E.coli* total lipid extract.

Peptide/lipid (molar ratio)	Relative leakage PC LUVs	Relative leakage POPC/POPG (70/30) LUVs	Relative leakage *E.coli* total extract LUVs
1/25	63%	100%	18%
1/50	26%	90%	13%
1/100	11%	60%	9%

Table 2. Relative leakage capabilities of Cnd, at different peptide/lipid ratios, in the presence of 100% POPC, 70/30 POPC/POPG and 100% total *E.coli* lipid extract LUVs.

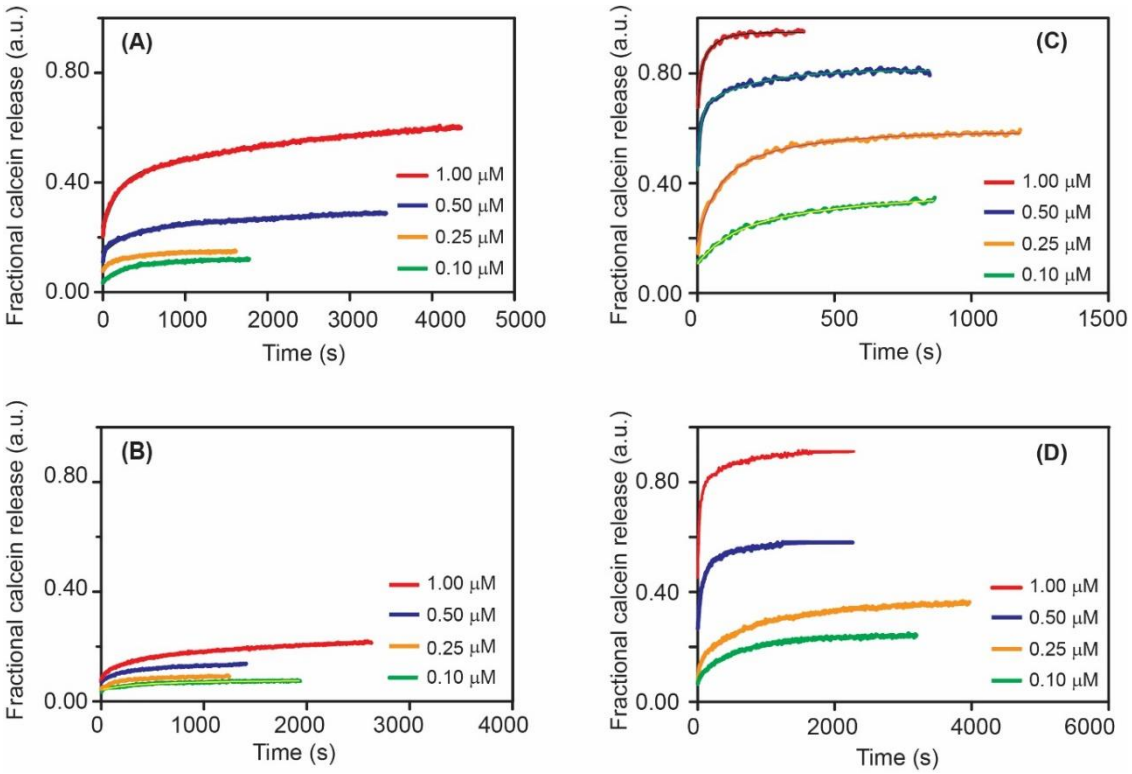

Figure 6. Kinetics of calcein efflux from LUVs after addition of different amount of Cnd from 0.10 μM through 1.0 μM. The curves are the experimental data normalized by Triton X-100. (**A**) Kinetics curves for POPC LUVs (25.0 μM) at different peptide concentrations; (**B**) kinetics curves for POPC LUVs (50.0 μM); (**C**) kinetics curves for POPC/POPG (70/30) LUVs (25.0 μM) and (**D**) kinetics curves for POPC/POPG (70/30) LUVs (50.0 μM). Note the difference in time scale for different panels.

	K_{SV} (M^{-1})	$1/K_{SV}$ (M)	Percent of quenching
Buffer	10.4 ± 0.2	0.096	100
POPC (LUVs)	2.9 ± 0.1	0.340	28.4
POPC-POPG (70:30 LUVs)	2.5 ± 0.1	0.408	23.6
E. coli (LUVs)	1.6 ± 0.2	0.625	15.4

Table 3. KI quenching. Stern–Volmer quenching constant (K_{SV}) and percentage of iodide quenching for Cnd in the presence of different lipid vesicles. The peptide/lipid molar ratio was 1:100 in all cases.

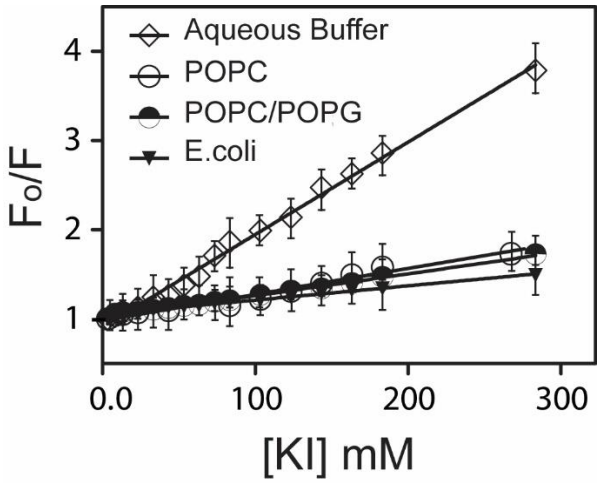

Figure 7. Stern–Volmer plots for the quenching of Tyrosine 6 of Cnd by KI in aqueous buffer and in the presence of POPC, POPC/POPG (70/30) and *E. coli* total extract LUVs.

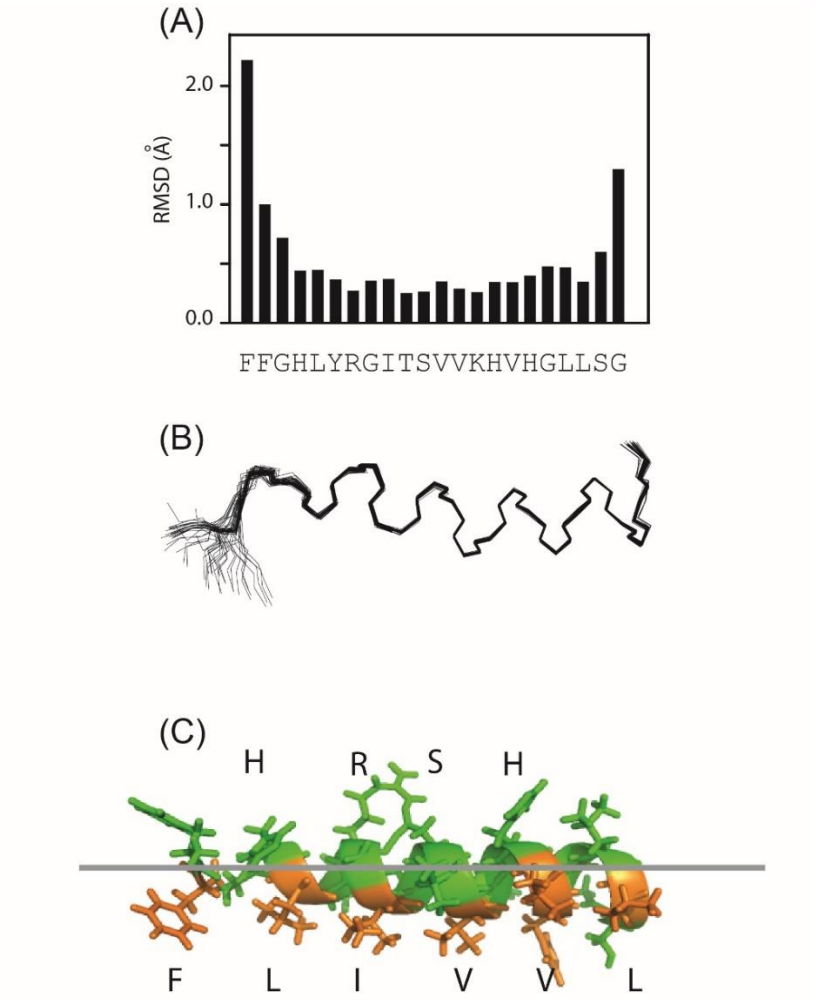

Figure 8. NMR structural models of Cnd. (**A**) Histogram of the backbone RMSD versus residues for the final 40 Cnd conformers, superimposing heavy atoms for residues 2–20; (**B**) conformational ensemble showing the convergence of the structures for heavy atoms of the backbone; (**C**) representative structure of Cnd showing the two faces of the amphipathic helix. The hydrophobic residues are represented in orange and the hydrophilic residues in green.

2.5 Supplemental Data

2.5.1 Supplemental tables.

Lipid vesicle concentration 25 µM

[P] µM	F_{eq} PC	PC/PG	σ_1 PC	PC/PG	σ_2 PC	PC/PG	k_1(s^{-1}) PC	PC/PG	k_2(s^{-1}) PC	PC/PG
0.10	0.1252	0.3787	0.0360	0.1454	0.0534	0.1272	0.001103	0.001465	0.00515	0.00855
0.25	0.1500	0.5856	0.0487	0.1741	0.0241	0.2249	0.002249	0.003544	0.02263	0.01557
0.50	0.3355	0.8131	0.1126	0.1431	0.0757	0.2254	0.000264	0.005121	0.00362	0.08149
1.00	0.6414	0.9500	0.2387	0.1479	0.1667	0.1652	0.000408	0.018941	0.00611	0.11511

Lipid vesicle concentration 50 µM

[P] µM	F_{eq} PC	PC/PG	σ_1 PC	PC/PG	σ_2 PC	PC/PG	k_1(s^{-1}) PC	PC/PG	k_2(s^{-1}) PC	PC/PG
0.10	0.0917	0.2418	0.0261	0.1391	0.0228	0.0322	0.000275	0.001436	0.00359	0.01082
0.25	0.0970	0.3684	0.0228	0.1782	0.0298	0.0859	0.001250	0.000792	0.00998	0.00713
0.50	0.1448	0.5775	0.0412	0.1069	0.0317	0.2065	0.001064	0.002399	0.00971	0.01678
1.00	0.2448	0.9096	0.1014	0.1501	0.0554	0.3614	0.000481	0.002130	0.00557	0.03475

Table S1. Kinetic parameters for calcein efflux from LUVs of different lipid composition upon addition of increasing amount of Cnd. The parameters are derived from fitting data with the equation: $F_t = F_{eq} - a_1 \exp(-k_1 t) - a_2 \exp(-k_2 t)$.

Residue	NH (ppm)	$C^{\alpha}H$ (ppm)	$C^{\beta}H$ (ppm)	Others (ppm)
F1	NA	4.051		δ-H
				ε-H
				ζ-H NA
F2	8.575	4.158		δ-H
				ε-H
				ζ-H NA
G3	8.229	3.979		
H4	8.567	4.154	3.178/3.108	δ -H 7.014
L5	8.066	4.061	1.695	γ-CH 1.596
				δ-CH_3 0.892
Y6	8.397	4.518	3.195	δ-H 7.020
				ε-H 6.794
R7	8.334	3.966	1.906	γ-CH_2 1.669
				δ-CH_2 3.270
G8	8.545	3.758		
I9	8.389	3.961	1.924	γ1-CH_2 1.671
				γ2-CH_3 1.593
				δ-CH_3 0.909
T10	8.185	3.766	4.187	γ-CH_3 1.094
S11	7.875	4.292	4.140/4.029	
V12	8.013	4.292	2.365	γ-CH_2 1.119
				γ-CH_3 0.972
V13	8.398	3.528	2.245	γ-CH_2 1.095
				γ-CH_3 0.905
K14	8.185	4.094	1.938	γ-CH_2 1.423
				δ-CH_2 1.832
				ε-CH_2 2.956
				ε-NH_3^+ 7.128

H15	8.162	4.541	3.355	δ-H	7.204
V16	8.611	3.752	2.264	γ-CH_2	1.106
				δ-CH_2	0.974
H17	8.629	4.300	3.394/3.304	δ-H	7.2414
G18	8.225	3.883			
L19	7.759	4.235	1.941	γ-CH	1.588
				δ-CH_3	0.925
L20	7.704	4.342	1.807	γ-CH	1.638
				δ-CH_3	0.891
S21	7.806	4.429	3.807		
G22	7.908	3.792			

Table S2. Resonance assignments of ^{1}H chemical shifts of Cnd in DPC detergent micelles using solution NMR experiments.

Parameter	Value
Distance and Angle Restraints	
Total NOEs Intraresidual Interresidual Angles	240 75 165 32
Hydrogen bond restraints	10
Total restraints per residue	12.8
Statistics for Calculated Structures	
R.M.S.D. (Å) Backbone All Heavy Atoms	 0.30 ± 0.17 0.92 ± 0.28
Analysis (performed with Molprobity)	
% residues in most favored regions % residues in additional allowed regions % residues in generally allowed regions % residues in disallowed regions	83.6 11.1 1.6 3.7

Table S3. Statistics for the 40 best NMR structures of Cnd in DPC micelles.

2.5.2 Supporting Figures.

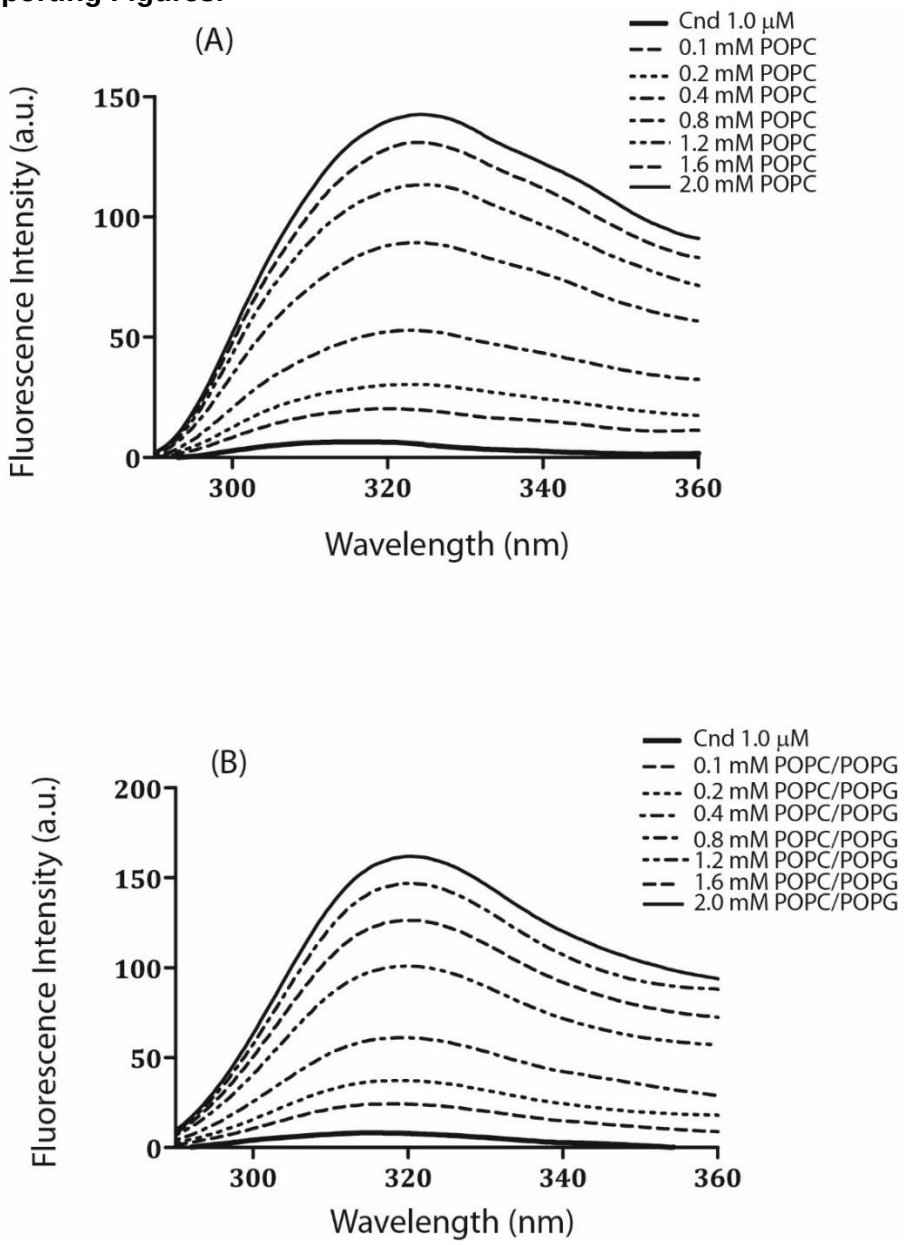

Figure S1. Partition experiments. Cnd fluorescence in absence and presence of increasing concentration of LUVs (**A**) POPC (**B**) POPC/POPG (70/30).

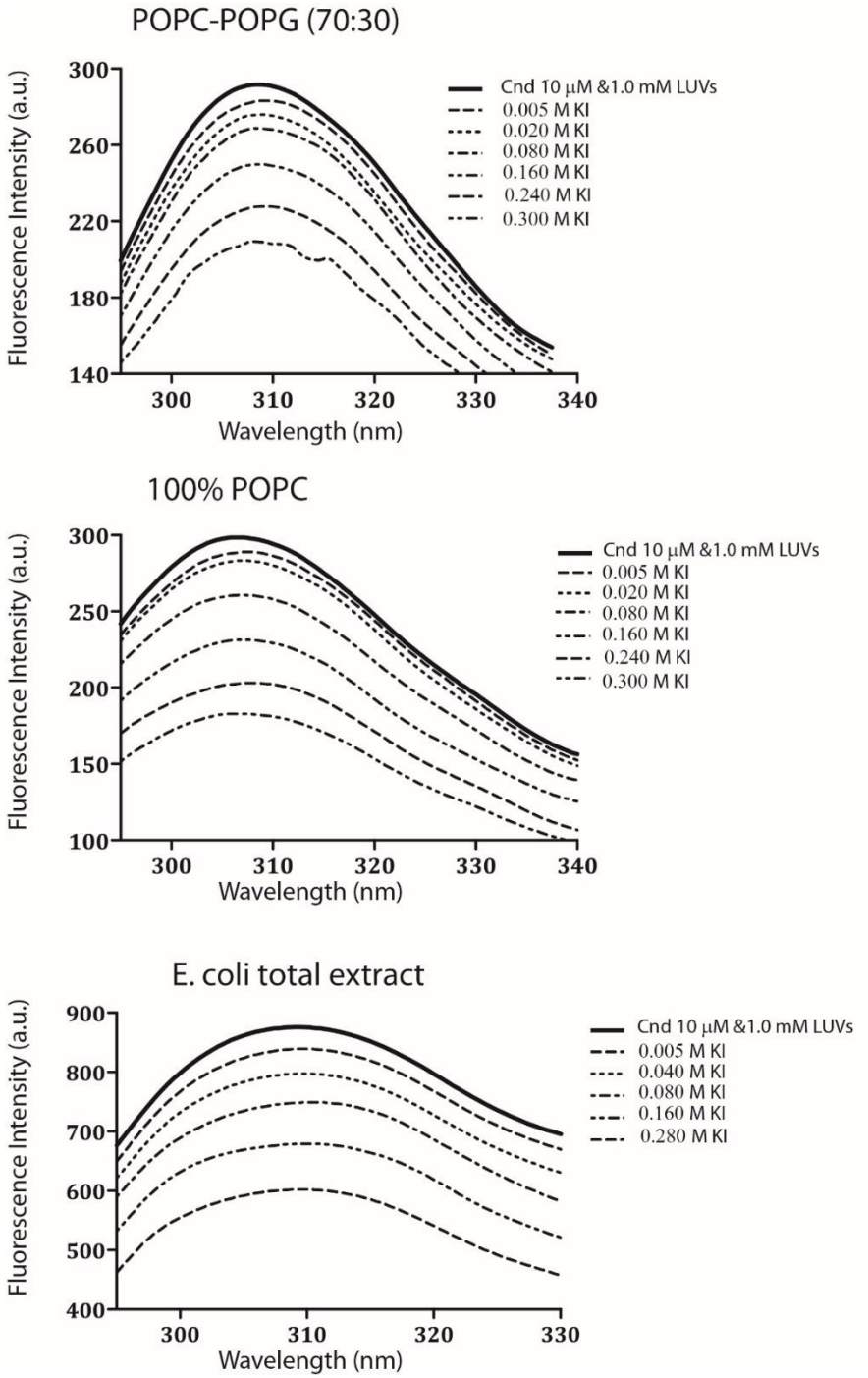

Figure S2. Iodide quenching experiments. Cnd intrinsic fluorescence in absence and presence of increasing amount of KI.

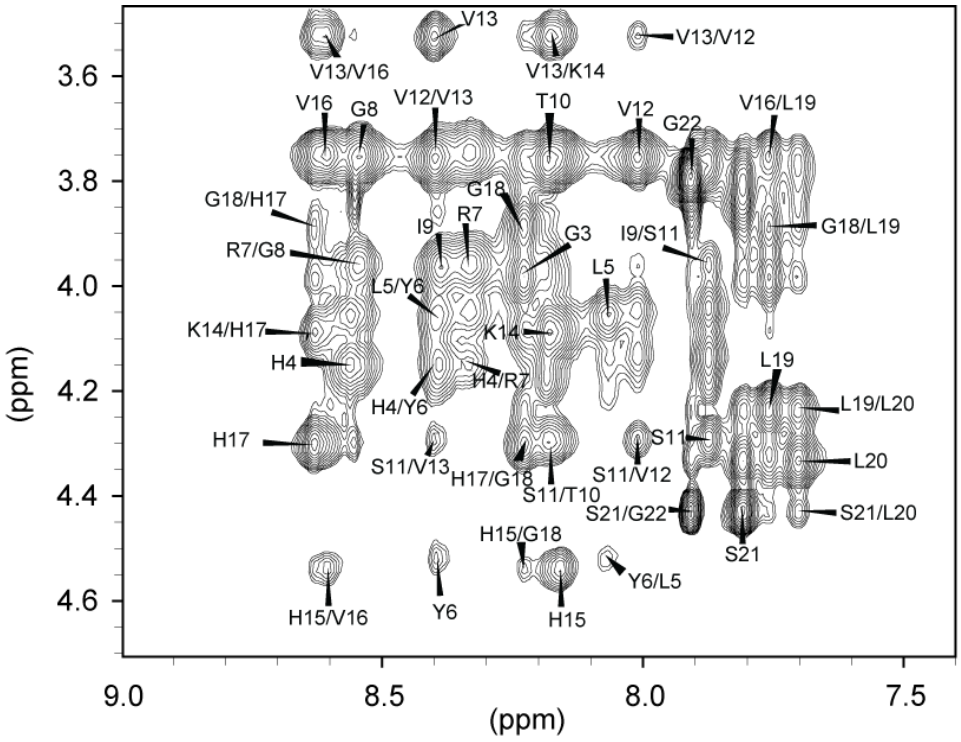

Figure S3. Fingerprint region of Cnd extracted from a 2D [^{1}H-^{1}H] NOESY experiment at 300 ms mixing time. The sample consisted of 1.5 mM Cnd reconstituted into phosphate buffer containing 300 mM DPC at pH 6.5.

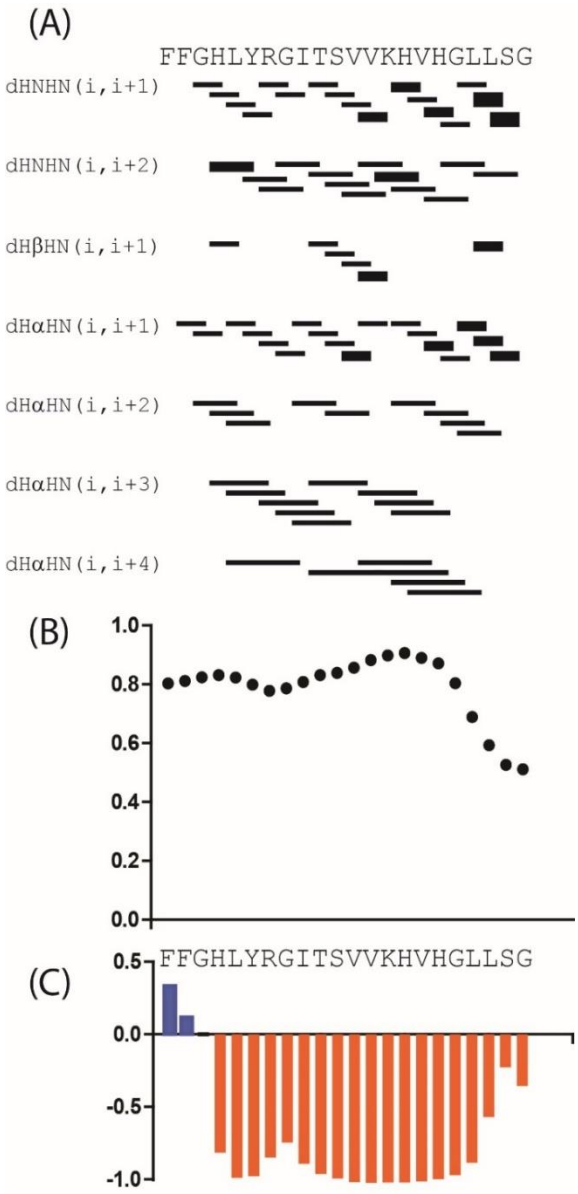

Figure S4. Summary of NMR structural parameters. (**A**) Backbone NOEs pattern for Cnd in DPC micelles. Correlations indicated with thick lines correspond to strong NOE, whereas correlation indicated with thinner lines correspond to medium or weak NOEs. (**B**) Predicted order parameter RCI-S^2 (residues with values less than 0.5 are dynamics) and (**C**) predicted secondary structure calculated using TALOS+. Negative bars indicate the helix structure while the height of the bars specifies the probability assigned using a neural network secondary structure prediction.

Chapter 3 - Ca^{2+} ATPase Conformational Transitions in Lipid Bilayers Mapped by Site-directed Ethylation and Solid-State NMR

Reprinted with permission and adapted from:

Vitaly V. Vostrikov, Martin Gustavsson, Tata Gopinath, Dan Mullen, Alysha A. Dicke, Vincent Truong, and Gianluigi Veglia. Ca2+ ATPase Conformational Transitions in Lipid Bilayers Mapped by Site-directed Ethylation and Solid-State NMR. *ACS Chem. Biol*. 2016; 11(2):329–334. Copyright (2016) American Chemical Society.

Abstract

To transmit signals across cellular compartments, many membrane-embedded enzymes undergo extensive conformational rearrangements. Monitoring these events in lipid bilayers by NMR at atomic resolution has been challenging due to the large size of these systems. It is further exacerbated for large mammalian proteins that are difficult to express and label with NMR-active isotopes. Here, we synthesized and engineered ^{13}C ethyl groups on native cysteines to map the structural transitions of the sarcoplasmic reticulum Ca^{2+}-ATPase, a 110 kDa transmembrane enzyme that transports Ca^{2+} into the sarcoplasmic reticulum. Using magic angle spinning NMR, we monitored the chemical shifts of the methylene and methyl groups of the derivatized cysteine residues along the major steps of the enzymatic cycle. The methylene chemical shifts are sensitive to the ATPase conformational changes induced upon nucleotide and Ca^{2+} ion binding and are ideal probes for active and inactive states of the enzyme. This new approach is extendable to large mammalian enzymes and signaling proteins with native or engineered cysteine residues in their amino acid sequence.

3.1 Introduction

Cell signaling events are mediated by membrane-bound enzymes and proteins that transmit their messages across lipid membranes through chemical, structural, and/or dynamical changes. Since membrane proteins are difficult to crystallize in lipid membranes, solid-state NMR (ssNMR) spectroscopy is the ideal high-resolution spectroscopic technique to monitor structural changes in liquid crystalline lipid membranes.[77,78,228] When the proteins or protein complexes exceed 100 kDa, the analysis of structural transitions becomes cumbersome as the number of structural probes (resonances) crowds the NMR spectra. For solution NMR spectroscopy, Kay and co-workers introduced recombinant protein expression protocols that enable amino acid specific ^{13}C methyl labeling.[229,230] The higher gyromagnetic ratio of ^{13}C with respect to ^{15}N in concert with longer relaxation times of the methyl groups makes it possible to image the methyl fingerprint region of larger proteins.[229,231] For example, such a labeling technique was used to monitor the conformational transitions of large enzymes by solution NMR.[232] For larger globular proteins containing reduced cysteine residues, it is also possible to covalently link ^{13}C-labeled methyl groups by site-directed labeling, incubating the protein with ^{13}C methylmethanethiosulfonate (MMTS).[233] Similar approaches have been utilized to probe the conformational landscape of membrane proteins by modification of Lys side chains,[234-236] or by introducing ^{19}F probes.[237-240] To date, these studies have been limited to detergent micelles that can affect protein structure, topology, and function compared to native lipids.[241-244]

Larger eukaryotic membrane proteins are very challenging to express recombinantly in amounts required for NMR spectroscopy.[245] Nonetheless, their structural

and dynamic transitions could still be monitored by NMR using cysteine reductive methylation.[233] However, this method presents severe spectroscopic challenges as the ^{1}H signals of nondeuterated proteins are typically broad and unresolved.[246] Moreover, the ^{13}C background signals arising from natural abundance ^{13}C from proteins and lipids complicate the appearance of the spectra. To overcome these problems, we synthesized ^{13}C-ethylmethanethiosulfonate (^{13}C-EMTS) and used it to alkylate the native Cys side chains (**Fig. 1**). This approach has three major merits: (i) It enables one to filter out the natural abundance ^{13}C signals using dipolar assisted rotational resonance (DARR) experiments,[247] making it possible to study membrane proteins in native lipid bilayers. (ii) It provides better resolution of the engineered aliphatic resonances with respect to methyl groups. (iii) The ^{13}C-EMTS probe is small and relatively nonperturbing, and labeling can be carried out in the aqueous milieu, retaining enzymatic activity.

As a proof-of-principle, we used site-directed ethyl labeling to monitor the conformational transitions of the sarcoplasmic reticulum Ca^{2+}-ATPase (SERCA), EC:3.6.3.8, a 110 kDa integral membrane protein that plays a key role in muscle contractility.[248,249] To monitor SERCA's conformational transitions, we labeled the most reactive cysteine residues with ^{13}C-EMTS and followed the chemical shift changes of both CH_2 and CH_3 signals by ssNMR DARR experiments. To assign the resonances, we employed a combination of paramagnetic relaxation enhancement (PRE) experiments. We were able to obtain domain specific assignments for all of the resonances in the P and N domains of SERCA, including two unambiguous assignments for ethyl groups linked to C674 and C636 of the P domain, defining the NMR signatures for the different conformational states of the enzyme.

3.2 Materials and Methods

The synthesis of ^{13}C-EMTS was accomplished by refluxing equimolar amounts of ^{13}C bromoethane and potassium methanethiosulfonate for 5 h in ethanol (**Figs. 1** and **S1**). The resulting product was filtered, and the solvent was removed by evaporation. The final product was identified by solution NMR and used without further purification. To label the ATPase with EMTS, we incubated 9 μM $C_{12}E_8$-solubilized SERCA purified from rabbit skeletal muscle[250] in reconstitution buffer (20 mM HEPES, 100 mM KCl, 1 mM Mg^{2+}, 5% glycerol, 0.02% NaN_3) with 45 μM (5-fold molar excess) of EMTS for 3 h. Enzymatic activity of labeled SERCA was measured by ATP hydrolysis assay.[251] The incubation time and the EMTS concentrations were varied to minimize activity loss of SERCA. Under conditions of 5-fold excess of EMTS relative to SERCA and 3 h incubation, the ATPase retains full activity (**Fig. 1**). Additionally, we have tested SERCA labeling with 10-fold and 20-fold excess of EMTS to assess whether all the cysteine residues in the enzyme are accessible to the labeling reagent. The enzymatic assay does not show SERCA activity in the presence of large excess of EMTS, suggesting that the least reactive cysteines are essential for the SERCA function (**Fig. S2**).

For SERCA reconstitution in lipid membranes, 9 mg of DMPC-d_{54} were solubilized in 18 mg of $C_{12}E_8$ and added to the ATPase. Detergent was removed by incubation with a 30-fold weight excess of biobeads for 3 h. The sample was centrifuged at 100 000*g*, and the pellet was resuspended in reconstitution buffer, dialyzed twice to remove any unreacted EMTS, and pelleted down at 100 000*g*. The proteoliposome pellet was resuspended in 1 mL of reconstitution buffer with appropriate ligands, sedimented by ultracentrifugation at 350 000*g* for 20 h, and the resulting hydrated pellet was transferred

to a 3.2 mm MAS rotor for NMR experiments. The ligands used to induce the different SERCA conformations were: 5 mM $CaCl_2$ (E1-Ca^{2+}), 2.5 mM AMPPCP (E2-ATP), 5 mM $CaCl_2$, and 2.5 mM AMPPCP (E1-Ca^{2+}-ATP) or 5 mM $CaCl_2$, 2.0 mM $AlCl_3$, 2.5 mM ADP, and 20 mM NaF (E1-Ca^{2+}∼P∼ADP). To increase the resolution, a constant-time version of the DARR experiment, [^{13}C,^{13}C]-CT-DARR, was used.[247,252] The spectrum was acquired at 4 °C with a spinning rate of 10 kHz on a 600 MHz Varian spectrometer. Acquisition parameters were 4000 points with a spectral width of 100 kHz (direct dimension). The corresponding values in the indirect dimension were 36 points and 5 kHz. A total of 1024 scans were acquired with 800 μs CP transfer, 100 ms DARR mixing time, and $\omega_{RF}/(2\pi)$ = 100 kHz TPPM decoupling.

3.3 Results and Discussion

The spectrum of labeled SERCA in DMPC bilayers obtained with a 5-fold excess of EMTS is shown in **Figure 1**. The SERCA spectrum with nonhydrolyzable ATP analog AMPPCP without Ca^{2+} shows well-resolved cross peaks between CH_2 and CH_3 moieties of the probe. Importantly, these are the only off-diagonal signals in the spectrum, as DARR transfer occurs only between adjacent ^{13}C nuclei, eliminating the natural abundance ^{13}C resonances of lipids and SERCA, which dominate one-dimensional ^{13}C spectra.[253] Thus, the EMTS labeling strategy enables spectral editing in 2D, enhancing the resolution. Since the transfer of magnetization in the DARR experiment is mediated by dipolar couplings, it is sensitive toward the mostly rigid groups. The differential mobility of the NMR probes can lead to distinct efficiencies of magnetization transfer, manifested as the variations in the peak intensity. The dynamics of the NMR probes can be further evaluated and quantified

with the appropriate techniques.[254,255] The ethyl cross peaks are clearly visible in the spectrum at ~16 ppm (CH_3−) and ~34 ppm (−CH_2−) with much greater resolution in the −CH_2– resonances. To identify the ethylated Cys residues of SERCA, we utilized trypsin digestion in combination with electrospray ionization tandem mass spectrometry (LC-MS/MS). We detected small peptides corresponding to 16 out of 23 Cys residues of SERCA, covering all Cys in the cytoplasmic P, N, and A domains. A high yield of Cys ethylation was achieved at six sites: 364, 471, 498, 561, 636, and 674 (**Figs. S3–S5**). To estimate the labeling efficiency, a large excess of iodoacetamide was added to SERCA immediately after the ethylation reaction and prior to trypsin cleavage. For two of the modified Cys, we detected carbamidomethylated (CAM) peptides with higher relative abundance than of the ethylated peptides (**Fig. S5**). Thus, we conclude that these residues have much lower percentage of ethylation and the peaks in the [^{13}C–^{13}C]-CT-DARR spectrum correspond to Cys 364, 471, 498, 561, 674, and 636 (**Fig. 2**).

While the DARR experiment enables one to measure short-range distances between the probes,[247,256] the distance separation of greater than 10 Å between the labeled cysteines precludes its use for distance measurement in the case of SERCA. To obtain domain specific assignments of the ethyl group fingerprint, we incubated SERCA in the E2-ATP state with various spin labels to selectively quench the NMR signals based on their proximity to the unpaired electron using paramagnetic relaxation enhancement (PRE; **Fig. 3**). Specifically, we engineered the TEMPO spin-label coupled to the lipid headgroup or to the 3′/5′ hydroxyl groups of the nucleotide (**Fig. S1**). Additionally, we selectively attached iodoacetamide TEMPO to C674, as described previously,[257] and performed the experiments with the oxidized and reduced spin label. The NMR spectra of the ethyl group fingerprint and EPR spectra corresponding to the spin-labels are shown

in **Figure 3**. Both DOPE-TEMPO and C674-MTSL are close to the lipid–water interface and quench the ethyl groups of the Cys in the P domain. The spin labeled nucleotide, ADP-TEMPO, bound in the N domain away from the membrane, partially quenched residues both in the P and N domains. Based on the quenching pattern, we assigned the resonances between 33.5 and 34.5 ppm to the ethyl groups cross-linked to the cysteines in the N-domain, whereas the resonances that are in the range between 34.5 and 35 ppm and 32.5 and 33.5 ppm to those of the P domain. Furthermore, we employed 10 mM ascorbic acid to reduce the free radical of C674-MTSL to hydroxylamine. The quenched spin label does not exert any effect on NMR relaxation of the adjacent ^{13}C nuclei, and the only missing signal can be assigned to the ethyl group on C674. Indeed, the 34.8 ppm peak is absent in the NMR spectrum, and therefore it is assigned to C674. Consequently, the remaining P-domain resonance at 33.1 ppm is assigned to C636.

The labeled Cys in the P and N domains of SERCA are ideally positioned to probe the allosteric communication between Ca^{2+} binding in the TM domain and nucleotide binding in the cytoplasmic domain (**Figs. S6–S7**). It has been proposed that the enzymatic cycle of the ATPase comprises several different conformational states.[249,258] For example, the structures of SERCA in the Ca^{2+}-free nucleotide-bound (E2-ATP),[259] Ca^{2+}- and nucleotide-bound (E1-Ca^{2+}-ATP),[260] and Ca^{2+}-bound nucleotide-free (E1-Ca^{2+})[261] states show distinct conformations of the cytoplasmic domains.[262-264] To test whether the ^{13}C-EMTS labeled sites are sensitive to the conformational transitions of SERCA, we mimicked these major states of the enzymatic cycle,[150] saturating the enzyme with AMPPCP, ADP/AlF_4, or Ca^{2+}. The ethyl group signatures of the enzyme's states display pronounced differences. In the Ca^{2+}-free form, SERCA populates the E2 conformational state, while the addition of Ca^{2+} shifts the equilibrium to the E1 state.[150,258] Upon

Ca^{2+} addition, the P domain peaks of the E2 state spectrum change substantially (**Fig. 4**). These peaks are sensitive probes for tracing the enzyme's interconversion between the E1/E2 states.

The center of mass of the cytoplasmic domains has the largest separation in the E1-Ca^{2+}structure (**Fig. 4**), which has been predicted to be highly dynamic.[262,263] It is notable that the resonance pattern and signal intensity of SERCA in this state differ significantly from the rest of the spectra. We speculate this may be attributed to the distinct motion time scale of this state. During the E1/E2 transition, the N-domain undergoes rotation and translation, with the ATP molecule bridging the N and P domains, stabilizing the enzyme. Accordingly, in the E2-ATP state, we observed all of the Cys ethyl groups, suggesting reduced conformational dynamics. The crystal structures of the E1-Ca^{2+}-ATP and E1-Ca^{2+}~P~ADP states are nearly identical (1.2 Å RMSD), and one can expect the ethyl fingerprints to be similar. Nevertheless, the pattern differs in both N-domain signals as well as C636, indicating structural and/or dynamic changes of SERCA going from ATP-bound to the transition mimic ADP·P-bound state.

The activity of SERCA is regulated by several factors: lipids,[44] other proteins,[113,265] and post-translational modifications.[266] The associated structural changes have been monitored using site-directed spin labeling of SERCA's Cys residues.[257,267-275] Although most of the chemical modifications of SERCA's Cys residues did not completely inactivate this enzyme, their size and mobility represent a problem for the accurate distance measurement, or monitoring allosteric coupling between ATP hydrolysis and Ca^{2+} transport.[269-271,273,276,277] These problems are even more apparent when small molecule inhibitors or activators are screened for drug discovery.[278] In such cases, the

combination of ethylation and ssNMR can provide a powerful approach to monitor ligand-induced conformational changes with SERCA function in a native membrane environment.

In summary, we demonstrated that site-directed ethyl labeling in combination with paramagnetic spin-labeling and solid-state NMR is a powerful method to study SERCA in lipid bilayers under fully functional conditions. Paramagnetic relaxation enhancement strategy enabled domain-specific assignments of the spectra, with two resonances unambiguously assigned to the individual cysteine residues. Importantly, the ethyl chemical shifts are sensitive to conformational changes of the enzyme, giving distinct signatures for the major structural states and will constitute specific reporters for active and inhibited states of the ATPase. This method will be widely applicable to monitor the conformational states of large proteins or protein complexes, purified from natural sources. It can be easily extended to smaller proteins and receptors expressed recombinantly, including GPCRs, where site-directed mutagenesis can make the assignments unambiguous. Moreover, it can be utilized to monitor dynamic changes via nuclear spin relaxation experiments.

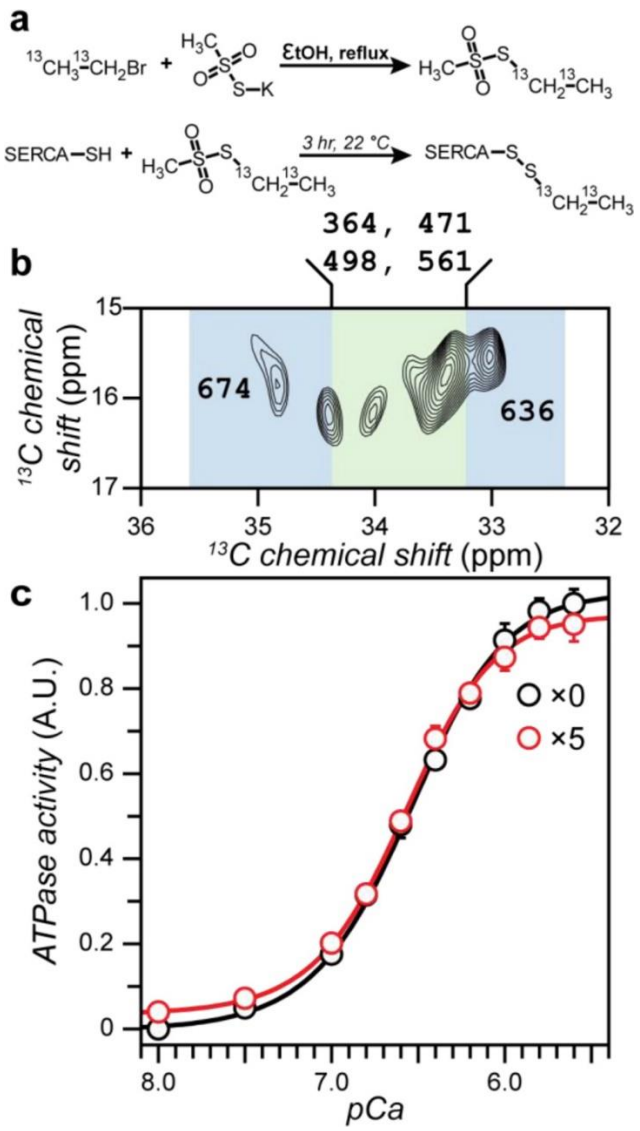

Figure 1. (**a**) Synthesis of ^{13}C EMTS and its usage for the labeling of cysteines of SERCA. (**b**) [^{13}C,^{13}C]-CT-DARR spectrum of ^{13}C-EMTS labeled SERCA. (**c**) Normalized ATPase activity of the ethylated SERCA: reaction with 5-fold excess of EMTS did not modify the activity of the enzyme.

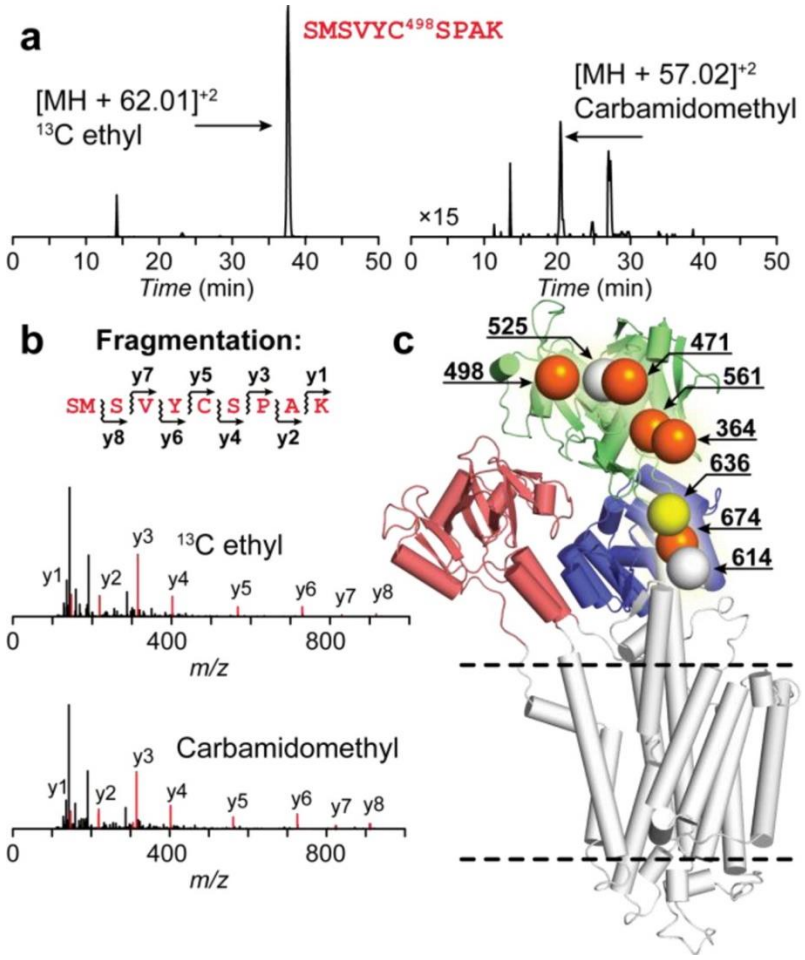

Figure 2. Mass spectrometry of ^{13}C-EMTS labeled SERCA. (**a**) Representative LC-MS chromatograms of a tryptic peptide with EMTS (+62) or CAM (+57) modifications. (**b**) MS2 fragmentation of the indicated peaks was used to confirm the peptide identity. (**c**) Cys in SERCA that are preferentially labeled (orange), partially labeled (yellow), and not labeled (white) with EMTS.

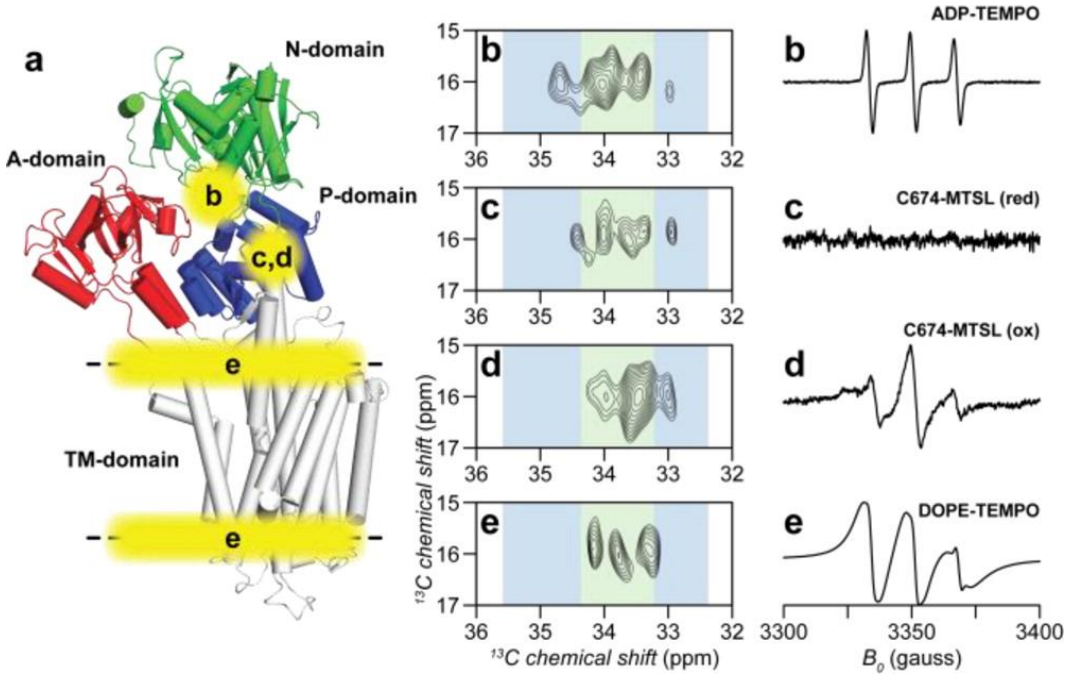

Figure 3. (**a**) Crystal structure of SERCA with the spin label positions indicated. (**b–e**) NMR and EPR spectra of the ethyl labeled enzyme with the spin labels indicated in **Panel a**. Residues in the proximity of the spin label are absent in NMR spectra due to paramagnetic relaxation enhancement. EPR acquisition conditions were identical to the ones described previously.[253]

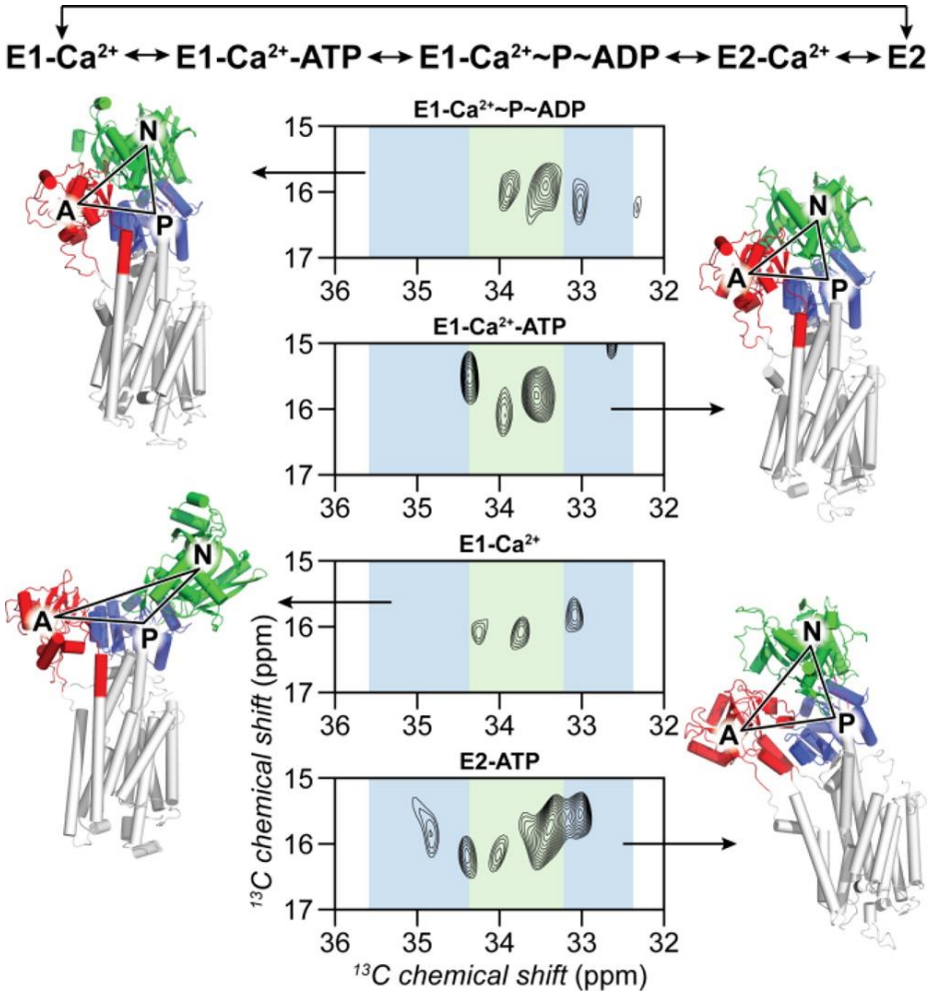

Figure 4. Enzymatic cycle[279] and conformations of SERCA by ethyl fingerprints. The crystal structures are Ca^{2+}-free E2 state (PDB ID: 1IWO), E1-Ca^{2+} (1SU4), E1-Ca^{2+}-ATP (1T5S), and E1-Ca^{2+}~P~ADP (2ZBD). Triangle vertices correspond to the centers of mass of the three cytoplasmic domains.

3.4 Supplemental Data

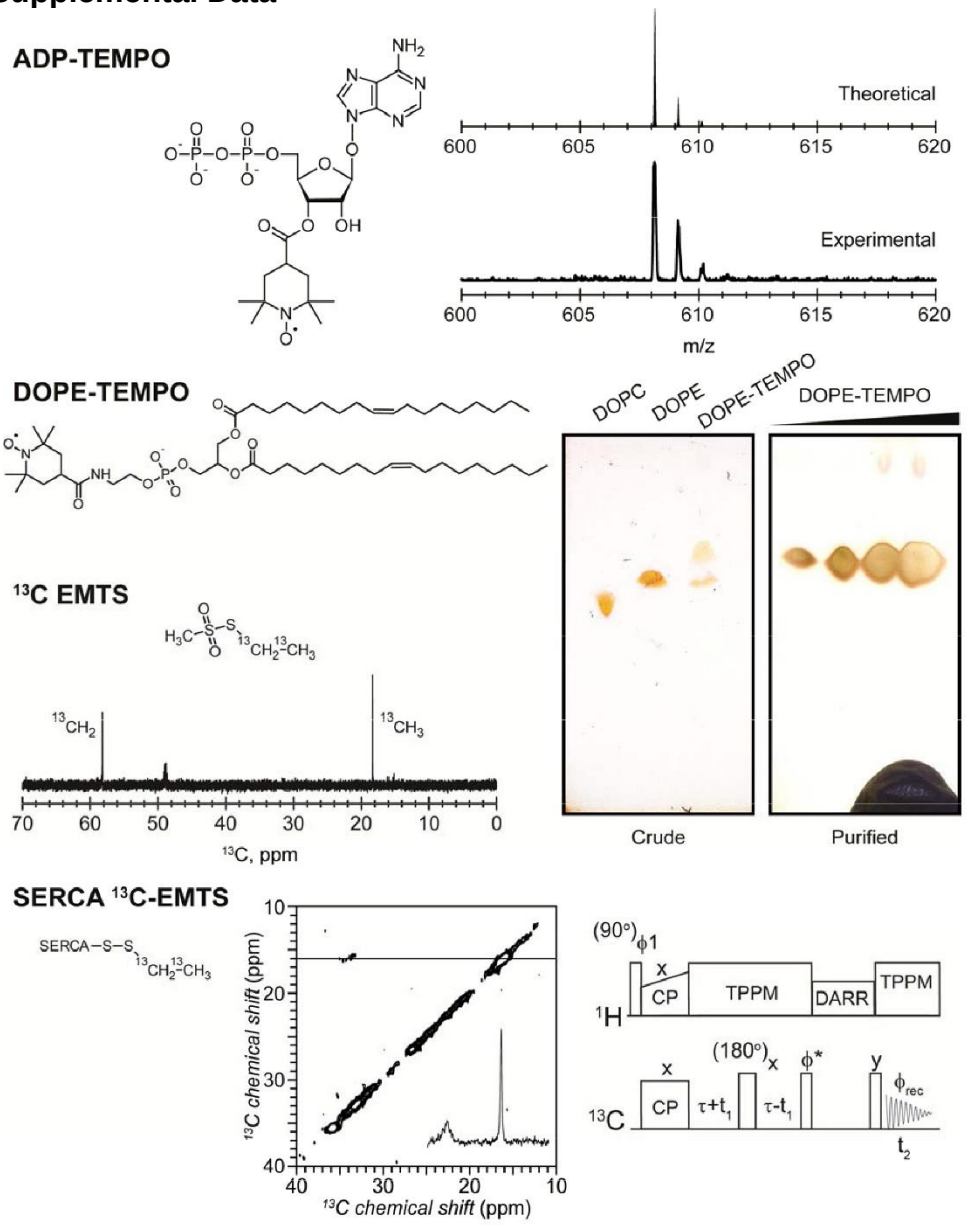

Figure S1. Synthesis confirmation of ADP-TEMPO, DOPE-TEMPO and ^{13}C EMTS. ADPTEMPO was synthesized with the spin label in either 3' or 5' positions, as seen in ESI-MS. DOPE-TEMPO spin label was synthesized from DOPE, and the crude product (left TLC) was purified by column chromatography, using chloroform:methanol:water 65:25:4 as eluent. Right TLC shows the increasing concentrations of the purified DOPE-TEMPO. Ethylating reagent, EMTS, was characterized by ^{13}C solution NMR.

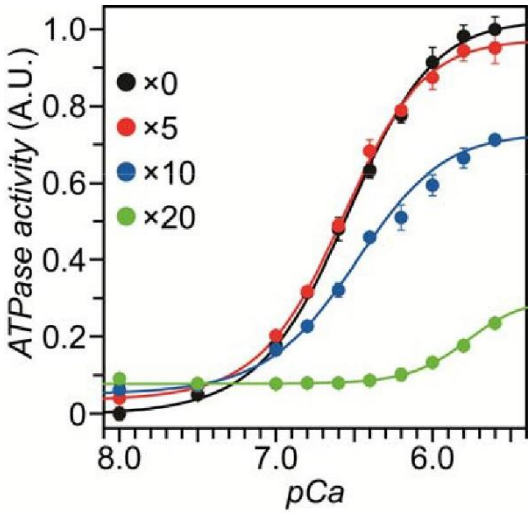

Figure S2. ATPase activity assays with varying amounts of ^{13}C EMTS. Molar excess of the ethylating reagent over SERCA is indicated in the legend. Out of 24 cysteine residues in SERCA1a, 16 are expected to be solvent exposed and accessible for labeling.

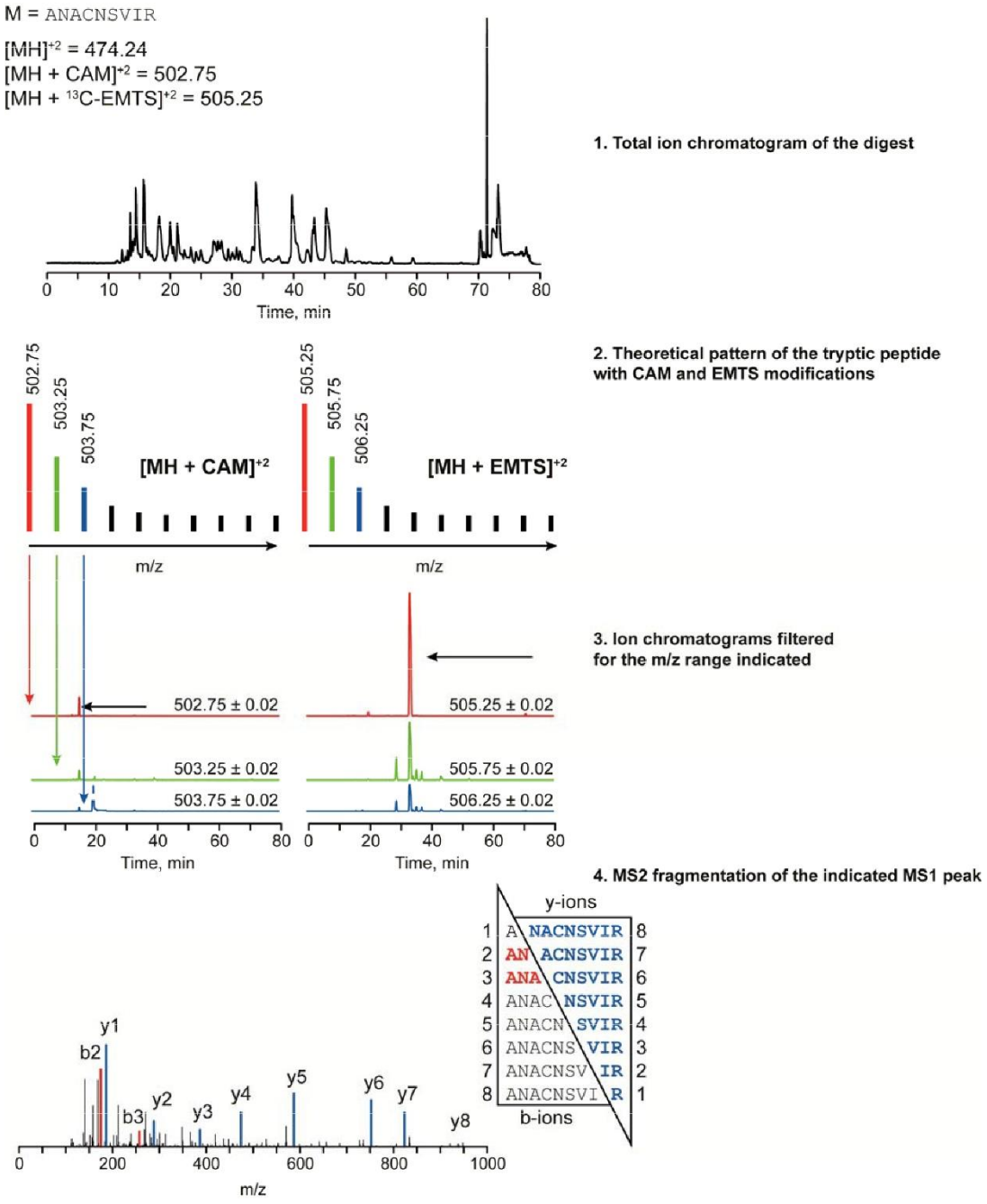

Figure S3. Identification of the modified peptides in the trypsin digest. Theoretical patterns of CAM and EMTS cysteine modifications were calculated using Protein Prospector, and the total ion chromatogram was filtered to include the three most intense signals from the envelope. The filtered ion chromatograms were used to identify the peaks corresponding to the target peptides, and their identities were further confirmed in the second fragmentation.

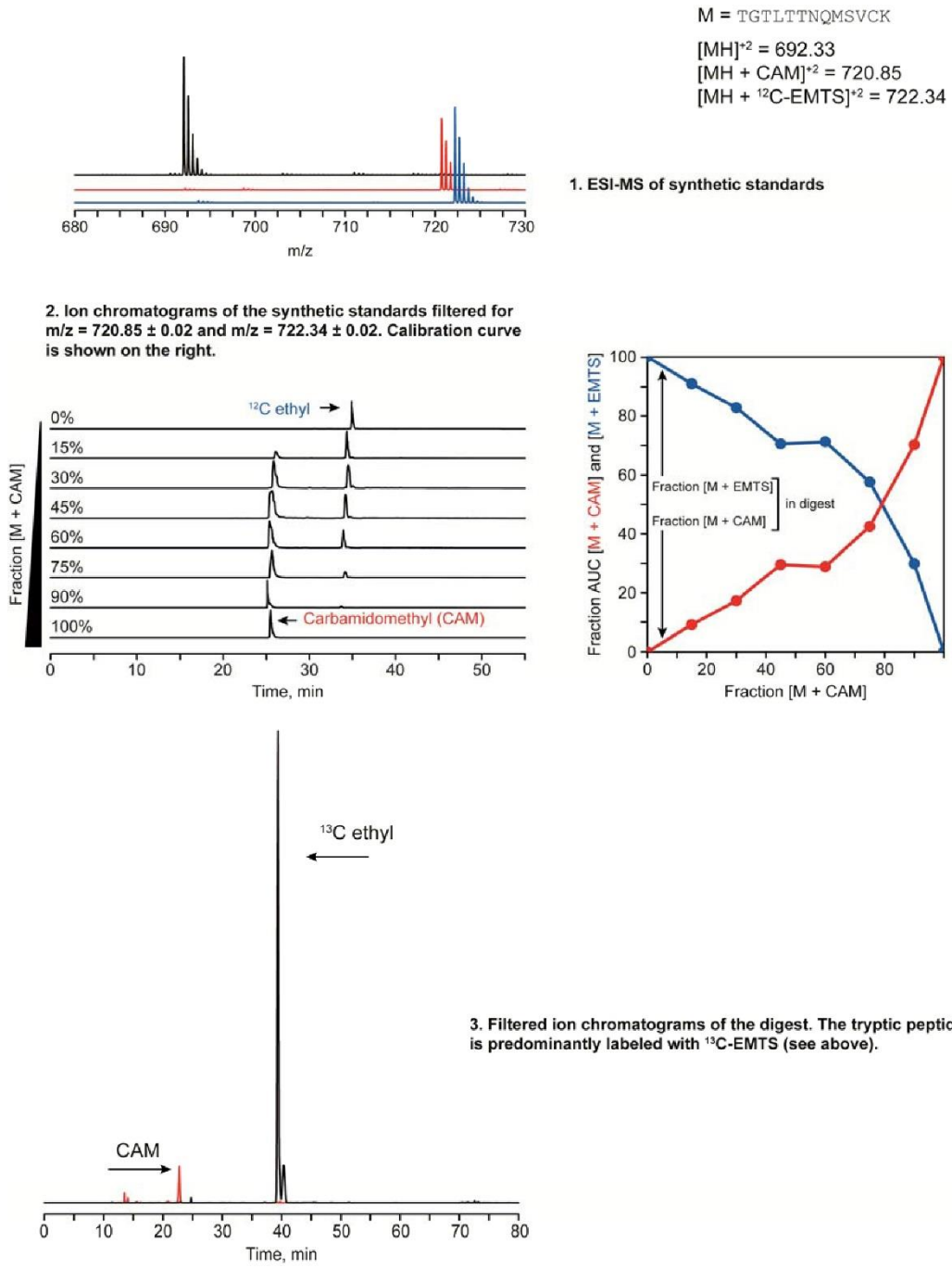

Figure S4. Quantification of tryptic digests using synthetic standards. Peptides corresponding to the detected fragments were synthesized and modified with either CAM, or ^{12}C-EMTS. Standard mixtures were prepared, and the calibration curves were plotted using the integrated ion chromatograms. The calibration plot was used to assess the relative ratio of CAM and ^{13}C-EMTS in the digests.

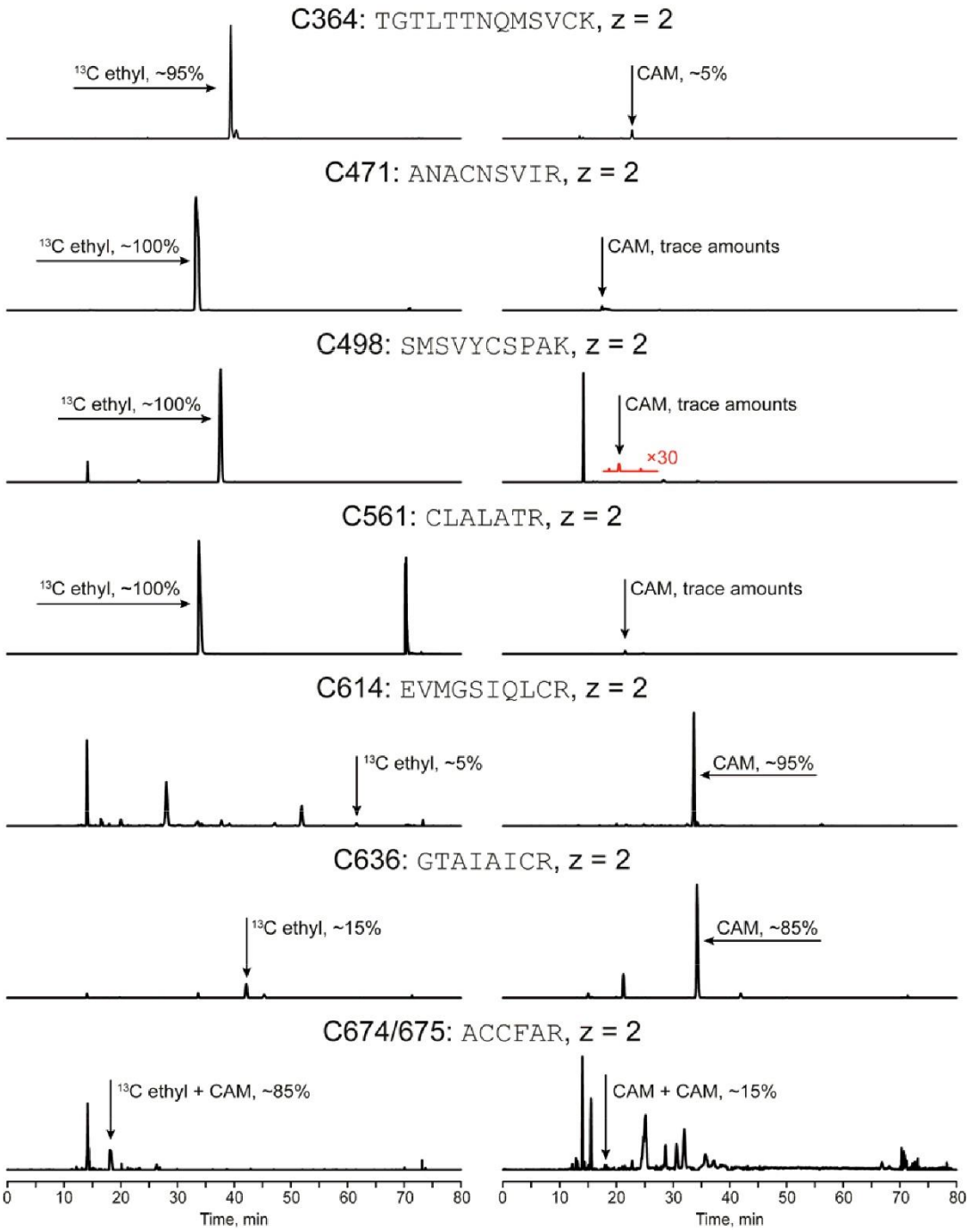

Figure S5. Evaluation of cysteine labeling in SERCA digests. Each tryptic peptide shown was processed according to the procedure exemplified in **Figs. S3-4**. Cysteines 364, 471, 498, 561 and 674/675 are the ones primarily labeled with EMTS; 636 is fractionally labeled, while 614 is mostly not labeled. Tryptic peptides for cysteines 12 and 52.

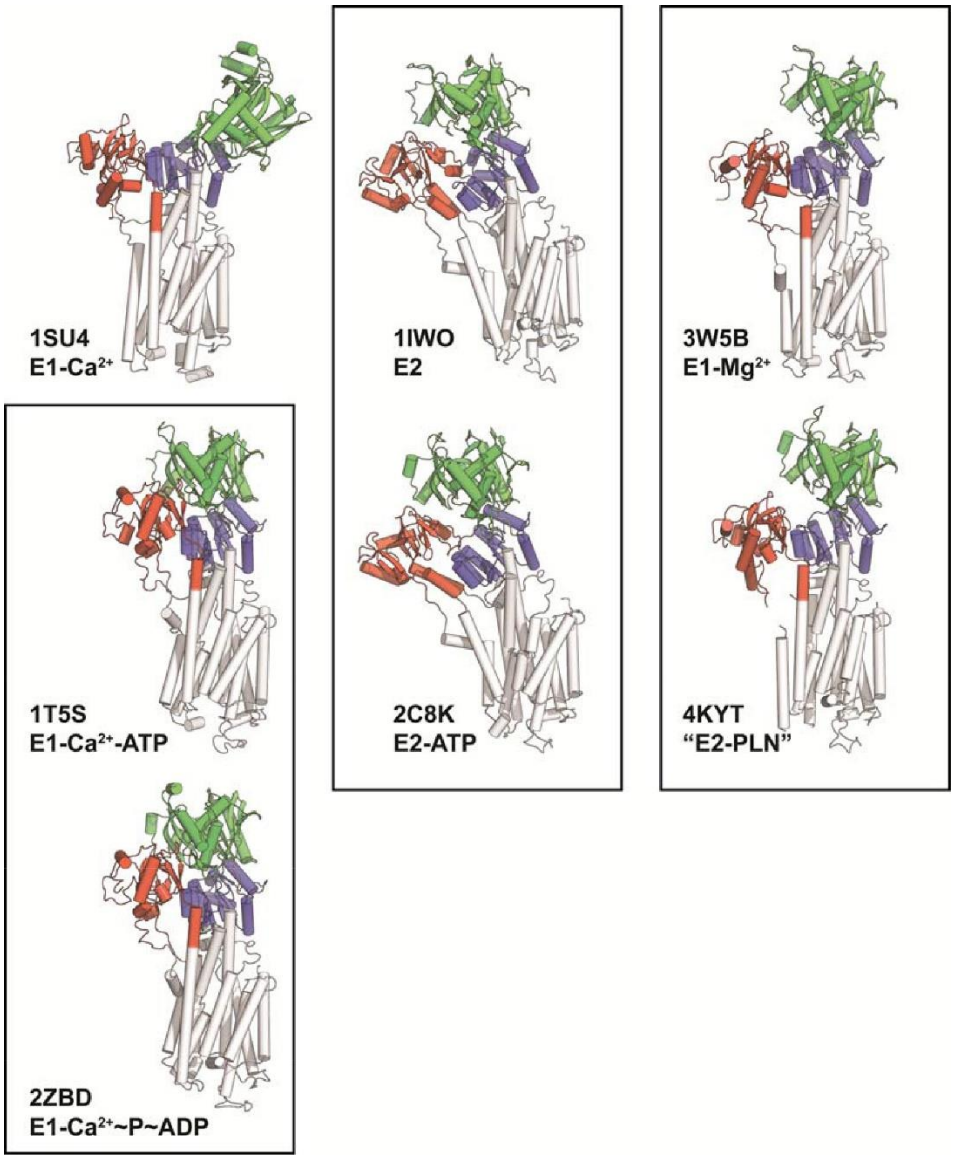

Figure S6. X-ray structures of SERCA1a. Conformational state and PDB codes are indicated. Domains are color coded as follows: A (red), N (green), P (blue), TM (white). Similar structures are indicated with rectangles.

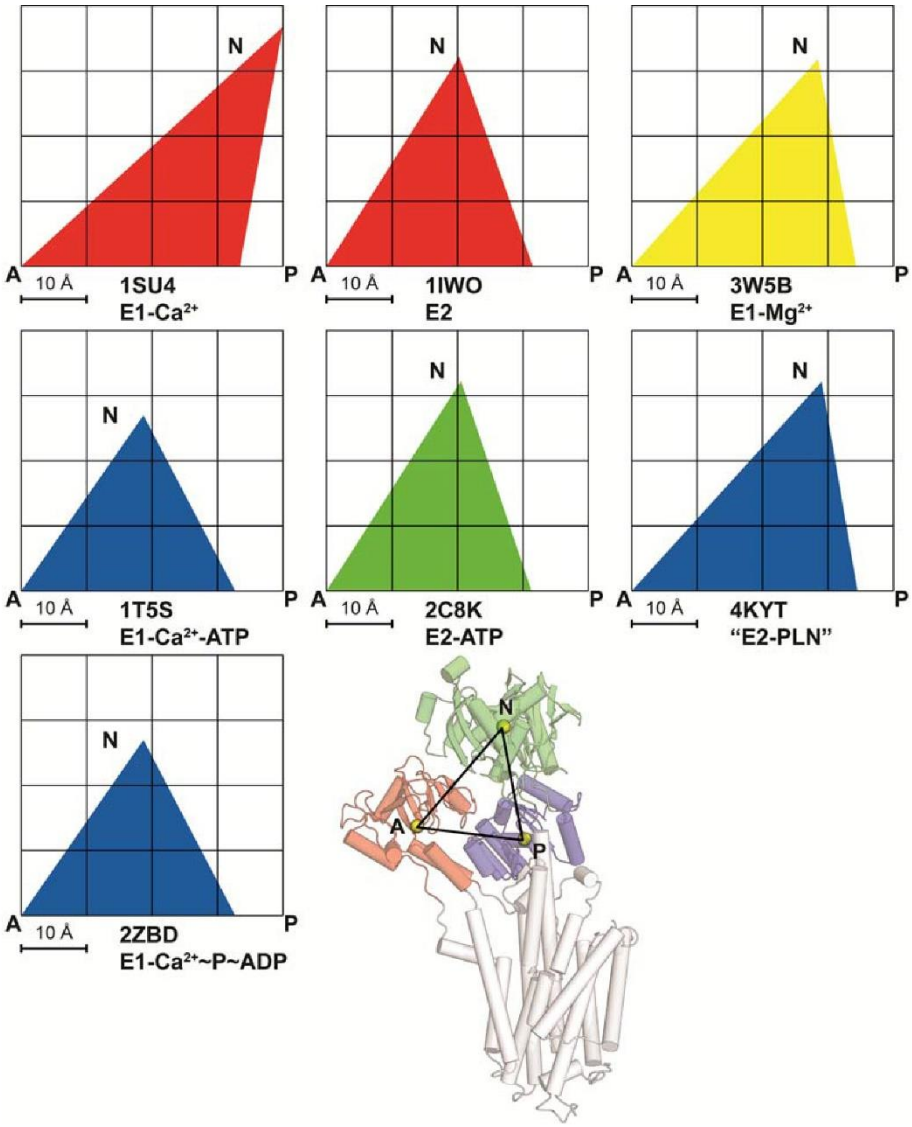

Figure S7. Distances and angles between the centers of mass of domains A, N and P for the structures of SERCA1a shown in **Figure S6**. The values used to construct the figures are tabulated below.

State	E1-ATP	$E1_{Ca}$-ATP	$E1_{Ca}$~P~ADP	E2	E2-ATP	$E1_{Mg}$-ATP	+PLN
PDB	1SU4	1T5S	2ZBD	1IWO	2C8K	3W5B	4KYT
A-N, Å	54.3	32.8	32.8	38.0	38.2	43.3	42.7
A-P, Å	33.4	32.7	32.7	31.5	31.3	34.5	34.3
P-N, Å	37.3	30.4	30.4	34.1	34.0	32.6	32.3
A-N-P, deg	37.2	62.1	62.3	51.4	51.0	51.7	52.2
N-P-A, deg	100.3	62.6	62.5	70.9	71.5	80.4	79.6
P-A-N, deg	42.6	55.3	55.2	57.8	57.5	47.9	48.2

Chapter 4 - Probing Residue-Specific Water–Protein Interactions in Oriented Lipid Membranes via Solid-State NMR Spectroscopy

Reprinted with permission from:

Alysha Dicke, T. Gopinath, Yingjie Wang, and Gianluigi Veglia. Probing Residue-Specific Water–Protein Interactions in Oriented Lipid Membranes via Solid-State NMR Spectroscopy. *J.Phys.Chem. B.* 2016; 120(42):10959–10968. Copyright (2016) American Chemical Society.

Abstract

Water plays a central role in membrane protein folding and function. It not only catalyzes lipid membrane self-assembly but also affects the structural integrity and conformational dynamics of membrane proteins. Magic angle spinning (MAS) solid-state NMR (ssNMR) is the technique of choice for measuring water accessibility of membrane proteins, providing a measure for membrane protein topology and insertion within lipid bilayers. However, the sensitivity and resolution of membrane protein samples for MAS experiments are often dictated by hydration levels, which affect the structural dynamics of membrane proteins. Oriented-sample ssNMR (O-ssNMR) is a complementary technique to determine both structure and topology of membrane proteins in liquid crystalline bilayers. Recent advancements in O-ssNMR involve the use of oriented bicellar phases that have improved both sensitivity and resolution. Importantly, for bicelle formation and orientation, lipid bilayers must be well organized and hydrated, resulting in the protein's topology being similar to that found in native membranes. Under these conditions, the NMR resonances become relatively narrow, enabling a better separation of ^{1}H–^{15}N dipolar couplings and anisotropic ^{15}N chemical shifts with separated local field (SLF) experiments. Here, we report a residue-specific water accessibility experiment for a small membrane protein, sarcolipin (SLN), embedded in oriented lipid bicelles as probed by new water-edited SLF (WE-SLF) experiments. We show that SLN's residues belonging to the juxtamembrane region are more exposed to the water–lipid interface than the corresponding membrane-embedded residues. The information that can be obtained from the WE-SLF experiments can be interpreted using a simple theoretical model based on spin-diffusion theory and offers a complete characterization of membrane proteins in realistic membrane bilayer systems.

4.1 Introduction

Water–protein interactions play an important role in driving the structural dynamics and functional properties of proteins.[280-284] Hydration forces mediate protein's packing via hydrogen bond networks and shape the structural integrity.[285,286] For membrane proteins, water has a dual role: it maintains the functional integrity of the domains that are more solvent-exposed (juxtamembrane and globular domains of membrane proteins) and plays an essential role in the structure and function of lipid membranes. In fact, in the absence of water, lipid membranes would not exist as their basic structural units self-assemble due to mainly hydrophobic effects.[287]

NMR is the only atomic resolution technique that can be used to study water–protein interactions in fully hydrated samples. Although NMR cannot visualize bound water molecules in active sites like X-ray crystallography, it can determine the relative exposure of atomic groups (e.g., backbone amides), monitoring either hydrogen/deuterium exchange[288] or using tailored pulse sequences.[289-292] Recently, these methodologies have been extended to magic angle spinning (MAS) solid-state NMR (ssNMR) of biological macromolecules.[293-295] These studies have demonstrated that the water–protein interactions in ssNMR can be probed by ^{1}H–^{1}H polarization transfer via chemical exchange, nuclear Overhauser effect (NOE), or dipolar spin diffusion between water and the surface of the protein.[296] However, high sensitivity and resolution of MAS samples often require low levels of hydration[297] with high protein:lipid ratios. Ideal hydration levels for MAS samples were found to be between 30 and 40%, as determined for the integral membrane protein diacylglycerol kinase (DAGK).[297] Nonetheless, the critical hydration level required for protein function may change from system to system, and low hydration

levels are likely to affect both the structural dynamics and function of membrane-embedded enzymes.[287,298]

A synergistic ssNMR approach is oriented-sample ssNMR (O-ssNMR), which provides direct topological information of membrane proteins in more realistic membrane models.[54,58,299] In fact, the formation of lipid phases, either mechanically or magnetically oriented, requires high hydration levels to reach liquid crystalline lipid phases.[299] These systems are suitable for characterizing water–protein interactions under native-like conditions.[241,300-303] Currently, the water–protein interactions of oriented membrane proteins require the comparison of the separated local field (SLF) spectra of protein samples reconstituted by using protonated and deuterated buffer conditions.[304,305] In this approach, the residues exchanging with deuterated water cannot be detected in the SLF spectrum and are flagged as water-exposed.[304,305] A drawback of this method is the preparation of two separate samples and/or the manipulation of the sample to exchange proton with deuterium.

In this work, we propose a spectral-editing technique for oriented membrane proteins to map the residue-specific water–protein interactions in oriented samples. We designed a water-edited (WE) SLF experiment that enables us to determine residue-specific exposure of the amide groups in oriented lipid membranes. In principle, this new approach can be applied to both mechanically and magnetically aligned samples. However, the more favorable spectroscopic properties of lipid bicelles[63,306] coupled with the sensitivity-enhanced (SE) method[149,307] make this approach much more powerful. The experiment is designed as a pseudo-three-dimensional (3D) experiment to obtain a protein fingerprint (polarity index slant angle wheel)[308] as a function of mixing time and determine the water exposure for each resolved site. As a benchmark, we used uniformly ^{15}N-labeled

sarcolipin (SLN), a single-pass membrane protein, whose structure has been fully characterized by solution NMR in micelles[141,142] and in lipid membranes using both MAS and oriented ssNMR.[143,145] SLN represents a prototypical transmembrane domain, with a membrane-embedded hydrophobic domain (domain II), a juxtamembrane region (domain Ib), and two hydrophilic termini comprising basic and aromatic residues that anchor SLN in the lipid membrane. H/D exchange factor measurements[309] using solution NMR studies indicate that both N- and C-termini and the juxtamembrane region (domain Ib) are water-exposed, whereas domain II is buried in the membrane bilayer and is virtually inaccessible to water. The WE-SLF data agree with the exchange factor data and can be interpreted with a simple theoretical model based on spin-diffusion theory[310], providing a new, general approach to test water accessibility for oriented NMR samples.

4.2 Materials and Methods

4.2.1 Sample Preparation

Uniformly ^{15}N-labeled SLN was expressed as a fusion protein with maltose-binding protein (MBP) in *Escherichia coli*, as previously described.[311,312] SLN was purified via amylose affinity chromatography, and MBP was cleaved using tobacco etch virus protease. The cleaved proteins were dialyzed in water, and the SLN precipitate was further purified using reverse-phase high-performance liquid chromatography. The purified SLN was lyophilized overnight. The lipids, 31 mg deuterated 1,2-dimyristoyl-*sn*-glycero-3-phosphocholine (DMPC) and 6.7 mg deuterated 1,2-dihexanoyl-*sn*-glycero-3-phosphocholine (D6PC), were dried and lyophilized overnight. The lyophilized SLN (1.9 mg) was co-dissolved with the deuterated DMPC using 500 µL of 1:1 ratio of methanol and water. The methanol was evaporated under a stream of N_2 gas, and the mixture was

lyophilized overnight to ensure removal of any remaining trace of organic solvent. The SLN/DMPC mixture was resuspended in 70 μL NMR buffer (20 mM *N*-(2-hydroxyethyl)piperazine-*N*′-ethanesulfonic acid, 50 mM KCl, 2.5 mM $MgCl_2$, 0.02% NaN_3) and sonicated. D6PC dissolved in 50 μL NMR buffer was then added. To prepare bicelles that align with the membrane normal parallel to the direction of the static field, $YbCl_3$ was added to a final concentration of 5 mM. Bicelles were formed after 3–5 freeze/thaw cycles, which resulted in a nonviscous solution between 0 and 15 °C and a viscous and clear solution above 30 °C. The final volume was adjusted to 160 μL by addition of NMR buffer, giving a final lipid concentration of 28% (w/v). Bicelles were transferred to a flat-bottom glass tube (New Era Enterprises) and tightly sealed with a polytetrafluoroethylene cap.

4.2.2 NMR Spectroscopy

All of the NMR experiments were performed on a Varian NMR System spectrometer operating at a ^{1}H frequency of 700 MHz equipped with a low-E bicelle probe built by the RF program at the National High Magnetic Field Laboratory in Florida.[313] A 90° pulse of 5 μs that corresponds to 50 kHz was used for both ^{15}N and ^{1}H channels, and a cross-polarization (CP) time of 500 μs was applied at ^{1}H and ^{15}N radio frequency (RF) field strengths of ~50 kHz. For WE experiments, the τ value was set to 1.8 ms that acts as a T_2 filter and dephases ^{1}H magnetization of the protein and lipid molecules, while retaining the water magnetization. Water–protein polarization transfer was achieved by varying the τ_{mix} value. For heteronuclear correlation (HETCOR) and SE-HETCOR experiments,[148] the windowless isotropic mixing (WIM) pulse sequence[314] was used for heteronuclear polarization transfer. During SE-polarization inversion spin exchange at the

magic angle (PISEMA),[307] the t_1 frequency-switched Lee–Goldburg (FSLG)[315] homonuclear decoupling was applied on the proton channel with a 50 kHz effective field,[316] whereas phase-switched spinlock pulses on the ^{15}N channel were Hartmann–Hahn[317] matched with a 50 kHz RF amplitude during t_1 evolution. For sensitivity enhancement, the τ delay was set to 75 μs, which corresponds to three cycles of FSLG with an effective RF amplitude of 80 kHz. Small phase incremental alteration 64 (SPINAL64) decoupling was used during acquisition with 50 kHz ^{1}H RF amplitude.[318] All of the data were processed using NMRPipe[199] and analyzed using *SPARKY*.[200]

4.2.3 Theory and Analysis of ssNMR Data

To interpret the spin diffusion in our system, we started from the general treatment of the diffusion of *z* magnetization $M(\vec{r}, \tau_m)$[310] at time τ_{mix}

$$\frac{\partial M(\vec{r},\tau_{mix})}{\partial \tau_{mix}} = \vec{\nabla} \cdot \left\{ D(\vec{r}) \vec{\nabla} M(\vec{r}, \tau_{mix}) \right\} \quad (1)$$

where $D(\vec{r})$ stands for diffusion coefficients. For a two-phase system, the magnetization is initially homogeneously distributed in phase A (water) and zero in phase B (protein). As the magnetization transfers from phase A to B, the buildup of exchange intensity I_B can be simplified as follows

$$\frac{I_B(\tau_{mix})}{I_B(\tau_{mix\to\infty})} = \sqrt{\frac{D\tau_{mix}}{\pi}} \frac{1}{f_A f_B} \frac{S_{AB}^{tot}}{V^{tot}} - O\left(\sqrt{\tau_{mix}^2}\right) \quad (2)$$

in which f_A and f_B represent the volume fractions of phases A and B, respectively. S_{AB}^{tot} denotes the total area of all interfaces between phases A and B,

and V^{tot} stands for the total sample volume. Assuming $f_A \approx 1$, and neglecting the quadratic terms $O\left(\sqrt{\tau_{mix}^2}\right)$, we obtain

$$\frac{I_B(\tau_{mix})}{I_B(\tau_{mix\to\infty})} \approx \sqrt{\frac{D\tau_{mix}}{\pi}}\frac{S_{AB}^{tot}}{V_B} \quad (3)$$

in which V_B denotes the volume of phase B. The magnetization transfer between water and a membrane-embedded protein results in a slow spin diffusion at the water–protein interface (WP) and a much faster intramolecular spin diffusion within the protein (PP). Therefore, we use an effective diffusion coefficient D_{eff} to account for the observed magnetization transfer in this more complex system

$$\frac{M_P(\tau_{mix})}{M_P(\tau_{mix\to\infty})} \approx \sqrt{\frac{D_{eff}}{\pi}}\frac{S_{WP}}{V_P}\sqrt{\tau_{mix}} \quad (4)$$

where S_{WP} stands for the total area of the water–protein interface, and V_P is the volume of protein. For $M_P(\tau_{mix}{}^s) = M_P(\tau_{mix} \to \infty)$, we obtain

$$\sqrt{\tau_{mix}^s} = \sqrt{\frac{\pi}{D_{eff}}}\frac{V_P}{S_{WP}} \quad (5)$$

Therefore, the magnetization of each residue along the protein sequence goes to saturation with different values of $\sqrt{\tau_{mix}^s}$ depending on their water exposure. Specifically, the TM domain of SLN can be approximated as a cylinder of volume $V_P = \pi R_{TM}^2 h$, where R_{TM} and h are the radius and height of the TM domain, respectively. Therefore, the residue-specific $\sqrt{\tau_{mix}^s}$ becomes linearly dependent on the position of each residue with respect to the helix

$$\sqrt{\tau_{mix}^s} \sim \sqrt{\frac{\pi}{D_{eff}}}\frac{\pi R_{TM}^2 h}{S_{WP}} \quad (6)$$

4.3 Results

The new SLF pulse sequences used to probe the water accessibility for SLN are depicted in **Figure 1**. **Figure 1A** shows the one-dimensional (1D) WE-CP experiment that uses water as a source of polarization for recording ^{15}N signals from SLN's amide backbone. The pulse sequence has an initial water-filter element identical to the MAS experiments.[293,294,296] An initial 90° pulse is followed by a spin-echo (~2 ms) that serves as a T_2 filter to dephase the protein as well as the lipid magnetization. The mobile water molecules, with longer T_2 relaxation, retain their magnetization, which is then flipped to the *z*-direction by another 90° pulse. A subsequent longitudinal mixing period (τ_{mix}) enables the transfer of ^{1}H polarization from water to protein, which is then transferred to ^{15}N using a 90° pulse followed by Hartmann–Hahn CP.[317] During CP, only the immobilized residues are subjected to heteronuclear polarization transfer via dipolar couplings. **Figure 1B** shows the implementation of the T_2 water-filter HETCOR experiment, WE-HETCOR. In this case, the t_1 evolution before τ_{mix} encodes the ^{1}H chemical shift of water. After the ^{1}H–^{1}H transfer, the amide proton magnetization is selectively transferred to the corresponding amide ^{15}N by the WIM24-CP[314] sequence followed by t_2 acquisition under SPINAL heteronuclear decoupling.[318] **Figure 1C** shows the two-dimensional (2D) WESE-PISEMA experiment, where the initial τ period, preceded by a 90° pulse, retains ^{1}H polarization from water, while dephasing the ^{1}H coherences arising from the protein and lipids. The protons of the protein are polarized via homonuclear zz transfer during the τ_{mix} period followed by a SE-PISEMA sequence.

The application of WE-CP to a U–^{15}N SLN sample reconstituted in lipid bicelles is shown in **Figure 2A** at different ^{1}H–^{1}H mixing times. Overall, the buildup is similar to that observed for the MAS experiments, with a sigmoidal trend.[293,294,296] At zero mixing time

(**Fig. 1A**), no signal is detected, confirming that the protein magnetization is completely dephased due to the initial spin-echo period. At short mixing times, we observe only a few selected signals. As the mixing time increases, the intensity of several other peaks builds up and reaches saturation at approximately 100 ms (**Fig. 2B**). A comparison between 2D SE-HETCOR and WE-HETCOR experiments is reported in **Figure 2C**. A ^{1}H–^{15}N correlation spectrum obtained with the SE-HETCOR experiment in the absence of the T_2 filter is shown in red. The spectrum acquired using the WE-HETCOR experiment with a 1.8 ms T_2 filter and 100 ms mixing time (τ_{mix}) is reported in black. As expected, the ^{15}N resonances of SLN's backbone are correlated with the water resonance at 4.7 ppm in the indirect dimension, whereas no correlations are obtained with amide or lipid protons, demonstrating that the T_2 filter retains only water magnetization.

To obtain site-specific water–protein interactions for the U–^{15}N SLN sample in lipid bicelles, we incorporated the T_2 filter into the SE-PISEMA experiment. SLN is a 31-residue helical membrane protein with short N- and C-terminal tails and is anchored to the lipid membrane via positively charged arginines.[141,143,319] MAS and oriented ssNMR experiments carried out in our laboratory have revealed the high-resolution structural topology of SLN in lipid bicelles.[145] The structure of SLN consists of a regular α-helix, flanked by several aromatic amino acids on both the luminal and cytoplasmic sides of the membrane bilayer. The SE-PISEMA spectra are well-resolved and enabled residue-specific assignments using both 2D and 3D experiments.[145] **Figure 3** shows the SE-PISEMA and WESE-PISEMA spectra of SLN, where τ_{mix} was set to 100 ms for ^{1}H–^{1}H transfer. As expected, at 100 ms mixing time, almost all of the residues are polarized by water via the spin-diffusion mechanism. Using a WESE-PISEMA sequence coded as a pseudo-3D experiment, we monitored the spin-diffusion kinetics, with τ_{mix} values

spanning from 1 to 100 ms. **Figure 4** shows the resultant spectra at various mixing times. At short mixing times, the WESE-PISEMA spectra display very low signal-to-noise ratios. For this reason, the 2D spectra with mixing times less than 10 ms were acquired with 512 scans, whereas 96 scans were sufficient for spectra acquired at longer mixing times (**Fig. 4**). For comparison, all of the spectra were plotted at the same noise level, and peaks corresponding to a signal-to-noise ratio greater than eight were picked. To interpret the spin diffusion of the *z* magnetization, we utilized the spin-diffusion theory described by Schmidt-Rohr and Spiess.[310] Assuming a simple geometric model for the single transmembrane domain of SLN, we modified the master equation to obtain **Equation 5** (see Theory and Analysis of ssNMR Data). The buildup plots of the intensities of SLN residues as a function of the square root of mixing time are shown in **Figure 5**. Note that due to dynamics, both N- and C-terminal residues are not sensitive to CP-based experiments and are not visible in the PISEMA spectra.[144] As for the integrated 1D spectrum of the WE-CP and MAS WE experiments,[296] the individual curves follow a sigmoidal behavior. The initial rate of polarization, 1–7 ms, is relatively fast for residues in domain Ib, including N11, T13, I14, and V15. Based on our model, this depends on the fast kinetics of polarization transfer from water to protein. This pattern is in agreement with previous solution NMR data carried out on SLN reconstituted in dodecylphosphocholine micelles, showing that the juxtamembrane domain Ib of SLN (residues 7–14) is more dynamic and has a higher solvent accessibility.[142] Note that the CP transfer is also influenced by protein dynamics and mosaic spread, as reflected by the nonuniform intensities of the peaks.[320] Because of its lower sensitivity, N11 could only be detected at 7 ms mixing time. In addition, residues T13 and L24 are overlapped in the 2D SE-PISEMA spectrum. To resolve this ambiguity, we ran a WE-CP experiment on a selectively leucine-labeled sample using 3 ms mixing time (**Fig. 6**). None of the leucine peaks were detected

in the WE-CP spectrum. The latter confirms that leucine residues in domain II of SLN are embedded within the core of the membrane and are not water-accessible. Nonetheless, these residues show clear peaks at longer mixing times, showing that spin diffusion is dominant and all of the residues can be polarized. On the basis of **Equation 6** in the previous section, the residue-specific mixing time $\sqrt{\tau_{mix}^{S}}$ was fitted against the height of residue in the TM regions. Overall, we found a linear relationship, where most of the residues lie within the 99% confidence intervals, supporting the theoretical model (**Fig. 7**). The small deviations from the theoretical model found for residues L16 and I17 are due to the low signal-to-noise ratio that is unavoidable for these sample preparations. **Figure 8** summarizes the site-specific water accessibility for SLN as obtained from the WE experiments. The backbone sites that are dynamic and not visible in the WESE-PISEMA spectra are represented in red. The other sites with increasing protection from the solvent are reported in yellow, green, cyan, and blue. The presence of resonances for the most protected residues in the PISEMA experiments at longer mixing times is due to water → protein → protein spin diffusion, which reaches complete saturation at mixing times greater than 100 ms. Overall, there is very good agreement between the exchange factors measured for SLN by solution NMR in micelles[142] and WESE-PISEMA spectra in lipid bicelles.

4.4 Discussion

For soluble proteins, water accessibility provides important insights into structural stability and dynamics.[321] On the other hand, for membrane proteins, it also provides a ruler to establish their insertion and topology within lipid membranes. In spite of the significant progress made by hydrogen/deuterium mass spectrometry,[322] NMR remains

the technique of choice to determine the relative water accessibility of protein residues at atomic resolution. Although solution NMR is able to map both kinetics and thermodynamics of membrane proteins in micelles, there is mounting evidence that micelles do not mimic membrane environments.[241,323,324] Both MAS and O-ssNMR utilize lipid environments to reconstitute membrane protein samples. Unlike in MAS, the samples used in O-ssNMR contain more than 70% water; hence, this method is ideal for probing water–protein interactions in a residue-specific manner. In particular, bicelles are emerging as a robust membrane-mimetic system for both small and large membrane proteins.[63,65] The self-assembly of lipid molecules for bicelle formation requires high hydration levels to form oriented phases.[325] A significant advantage of bicelles is the long relaxation in the dipolar dimension of the SLF experiments that enable the implementation of sensitivity-enhancement schemes[146] and boost the sensitivity of the static NMR experiments. The new experiments reported here make it possible to monitor the water exposure of amide resonances with relatively high sensitivity. As for the previous MAS experiment, water–protein polarization transfer is mediated by chemical exchange, NOE, and spin-diffusion mechanisms.[281,296] These studies have demonstrated that, although the rate of ^{1}H–^{1}H transfer depends on these mechanisms, the shorter mixing times used make it possible to select the residues most accessible to water. The behavior of the polarization transfer in our static WE experiments follows the same trend and could also be utilized as a spectral-editing technique.[326,327] From an experimental point of view, a key parameter is the mixing time, τ_{mix}, which needs to be optimized for polarization transfer from water to protein. For SLN, we found that even at short mixing times (1–3 ms), the residues of the juxtamembrane domain Ib are polarized, indicating the close proximity of water molecules.

Although there have been several advancements in the field of O-ssNMR,[54] there are still limitations for larger membrane proteins that present significant overlap of resonances in the SLF experiments. WE experiments under MAS conditions have been successfully used for studying G protein-coupled receptor, potassium channel, and M2 channel membrane proteins,[293] but the spectral simplification via the WE experiments presented in this article could be a turning point for new methodological developments to determine the 3D structure of larger, oriented membrane proteins.

4.5 Conclusions

We demonstrated the ability of O-ssNMR to investigate residue-specific hydration of membrane proteins reconstituted in oriented lipid bicelles. The relative exposure of the residues to water provides a ruler to establish the location and the structural topology of the transmembrane segments in fully hydrated liquid crystalline membranes. Indeed, these results demonstrate that the water molecules are indeed an intrinsic part of the membrane protein environment and can be further exploited to study protein function. In the case of SLN, the accessibility of the juxtamembrane domain Ib supports the plasticity of this protein and the importance of this domain in the regulation of the Ca^{2+}-ATPase, supporting previous studies carried out in detergent micelles. Together with the recent advancements in sample preparation and NMR methodology, the WE experiments presented here will bring a new dimension in O-ssNMR to study membrane proteins.

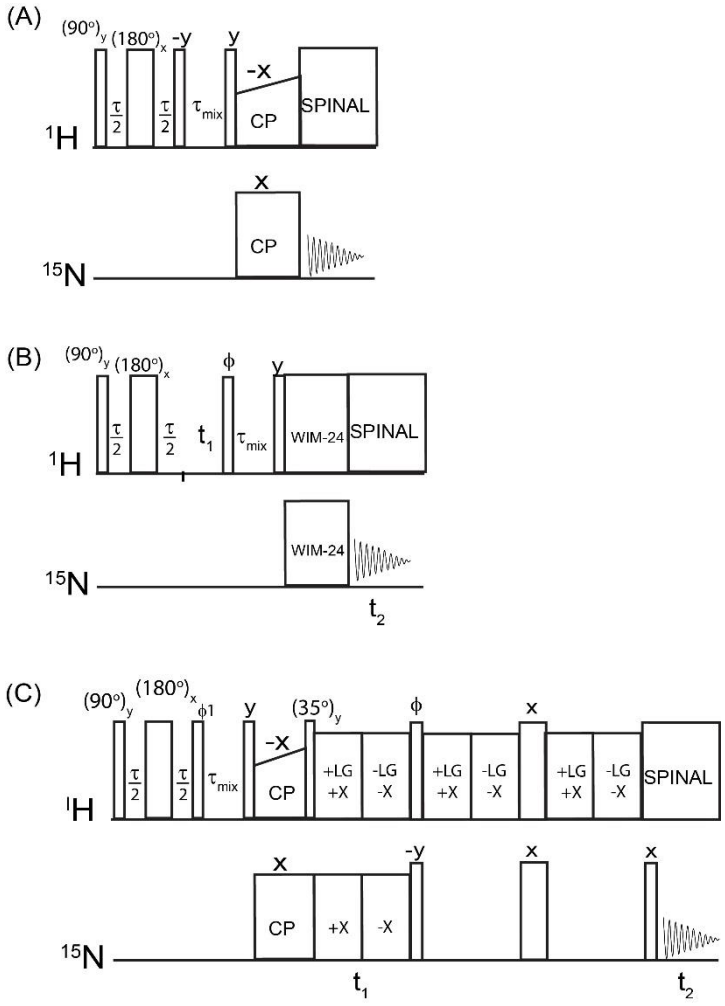

Figure 1. WE-oriented ssNMR. Pulse sequences for (**A**) WE CP, (**B**) 2D HETCOR experiment for water–protein correlation, and (**C**) WESE-PISEMA that can be used as pseudo-3D by varying the τ_{mix} value.

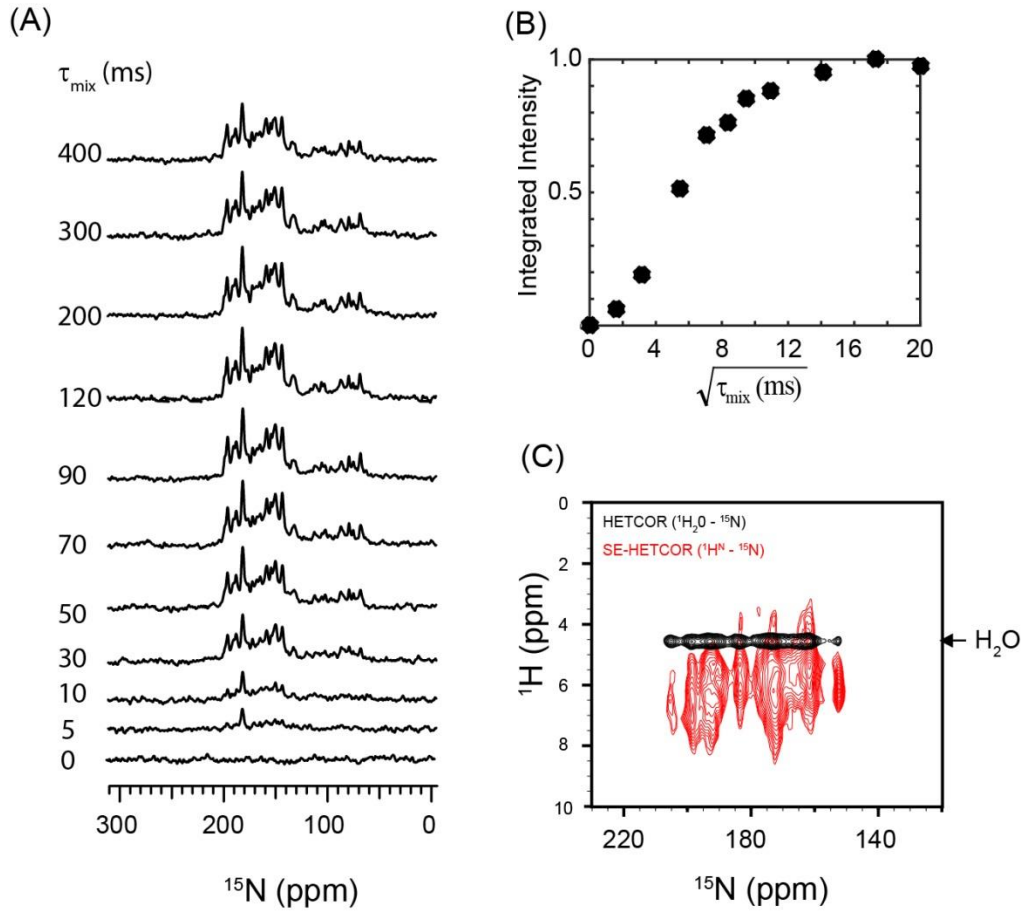

Figure 2. (**A**) WE-CP spectra obtained at various mixing times using the pulse sequence of **Figure 1A**. (**B**) Integrated intensity of the 1D spectra between 130 and 210 ppm is plotted with respect to the square root of mixing time. (**C**) 2D HETCOR spectrum (black) between water and protein residues obtained from the pulse sequence shown in A using 100 ms mixing time and $^{1}H^{N}$–^{15}N correlation (red) of the protein backbone obtained from the SE-HETCOR experiment.

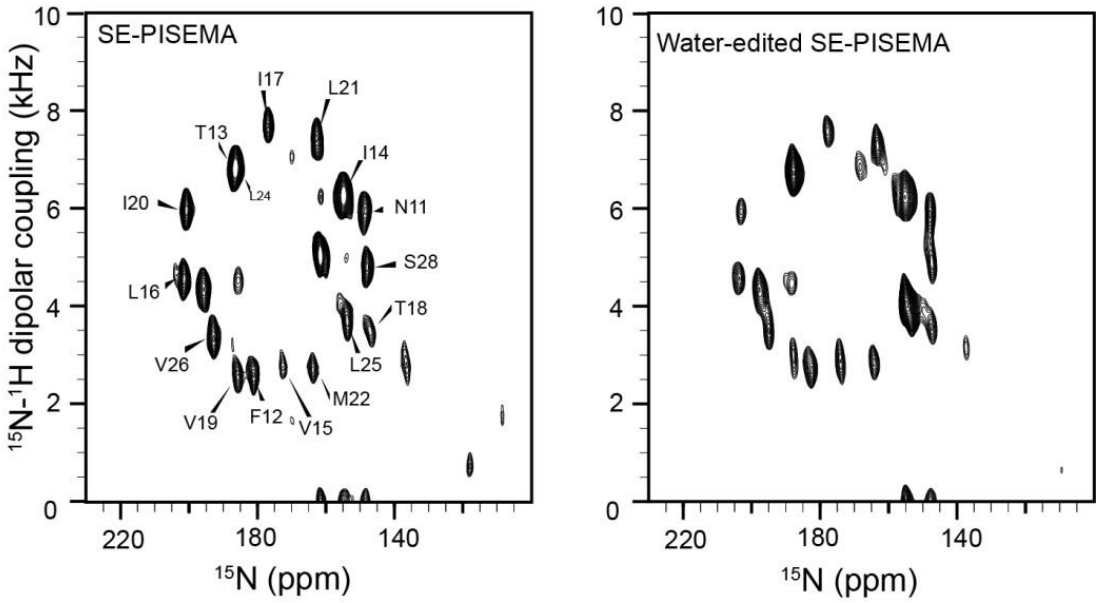

Figure 3. 2D SE-PISEMA and WESE-PISEMA spectra of uniformly ^{15}N-labeled SLN in oriented flipped bicelles. A mixing time of 100 ms was used for WESE-PISEMA.

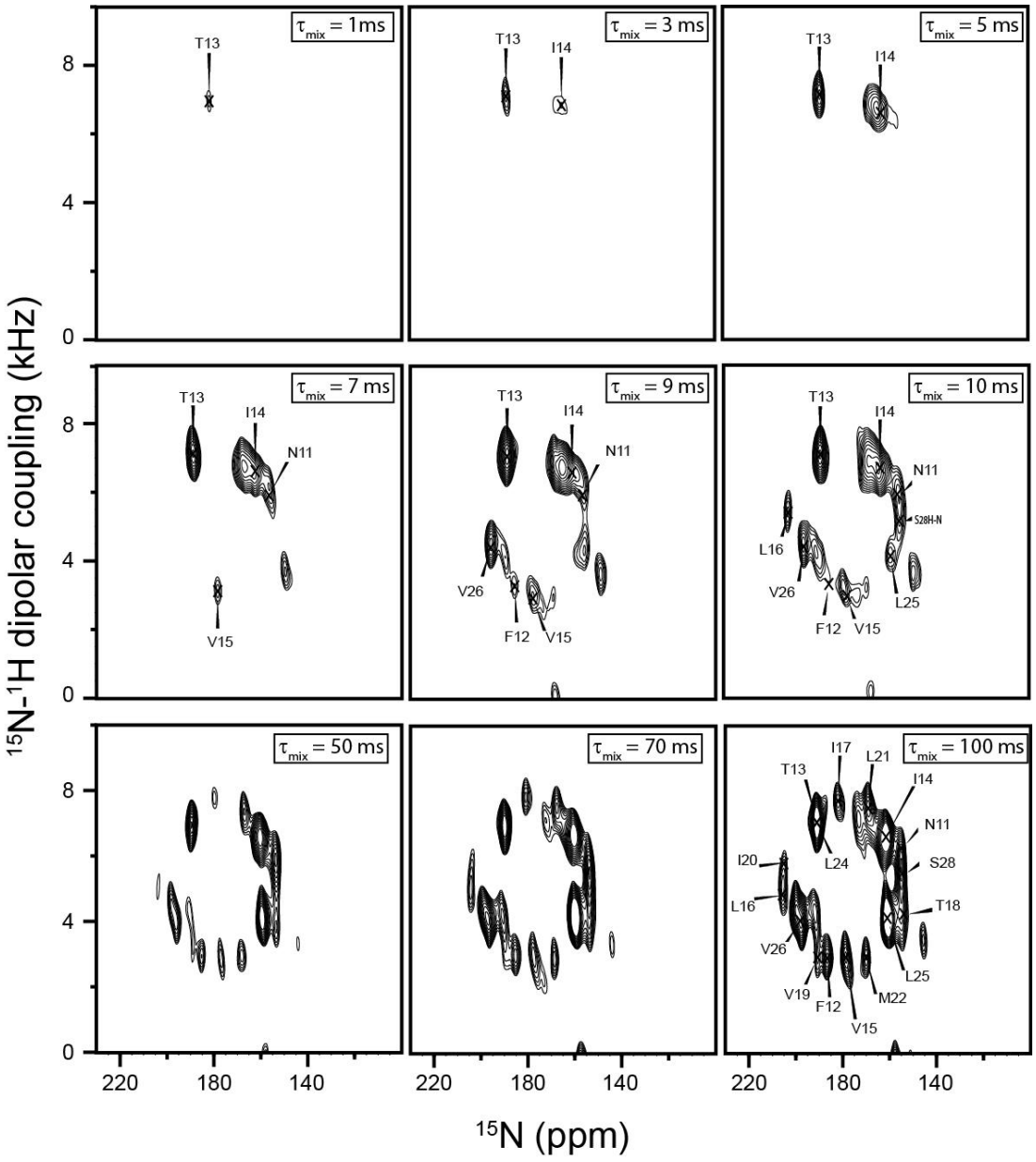

Figure 4. WESE-PISEMA spectra of SLN obtained at various mixing times using the pulse sequence of **Figure 1C**. All of the spectra are plotted at the same noise level. The τ_{mix} values were 1, 3, 5, 7, 9, 10, 50, 70, and 100 ms. The spectra at τ_{mix} values less than 10 ms were acquired with 512 scans. The remaining spectra were acquired with 96 scans. For comparison, all of the spectra are plotted using the same noise level.

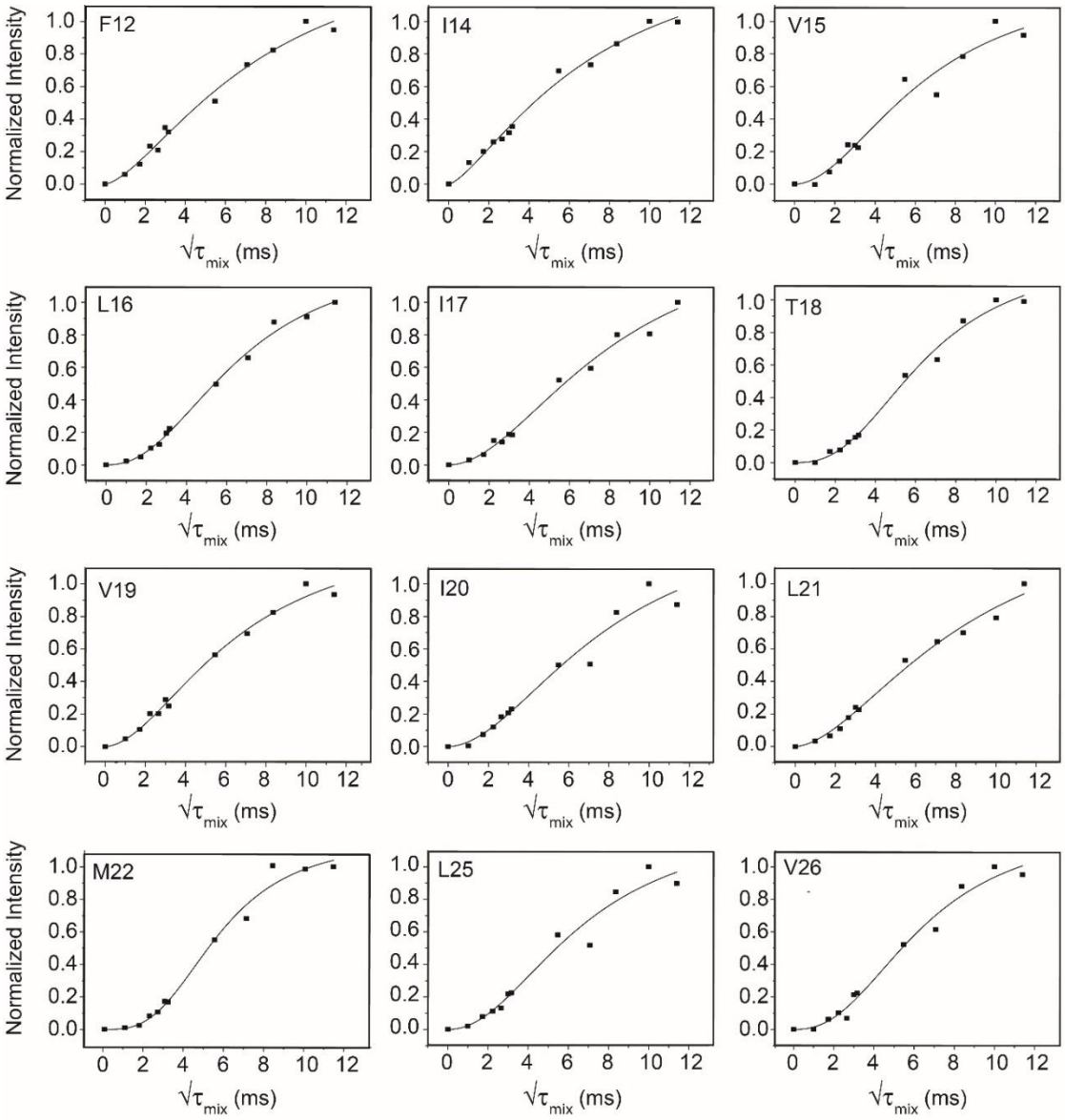

Figure 5. Peak intensities of each residue obtained from **Figure 4** plotted with respect to the square root of mixing time. The intensity of each peak was normalized relative to its SE-PISEMA intensity. The residues near the termini build up faster than those within the transmembrane region. The residues with peaks that are overlapped, such as T13, are not plotted.

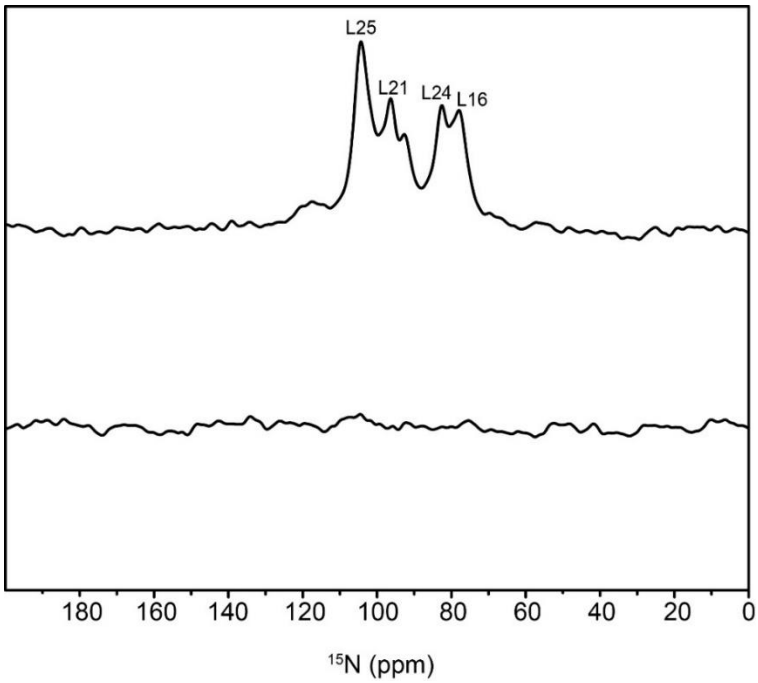

Figure 6. CP (**top**) and WE-CP (**bottom**) spectra of selectively leucine-labeled SLN. WE-CP was acquired with a mixing time of 3 ms. No peaks are observed, indicating that L24 is not accessible to water at 1–3 ms mixing time.

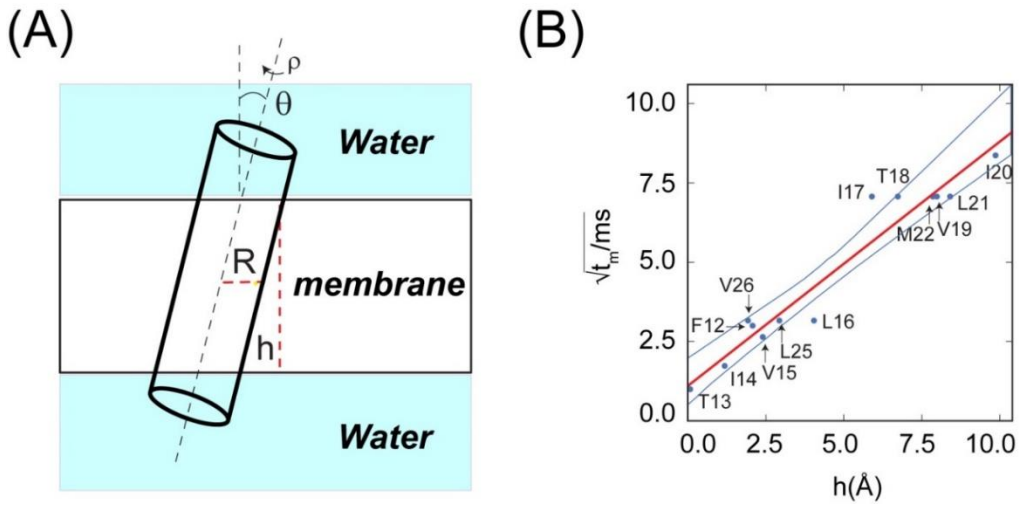

Figure 7. Model of residue-specific magnetization transfer from water to SLN. (**A**) Schematic illustration of the membrane protein complex. SLN's helical structure can be approximated as a tilted cylinder with a radius R. The height, h, is the distance of the residue in the TM region from the water–protein interface. (**B**) Linear fitting (red) of the residue-specific against h of each residue. The boundary of the 99% confidence intervals is shown as blue lines.

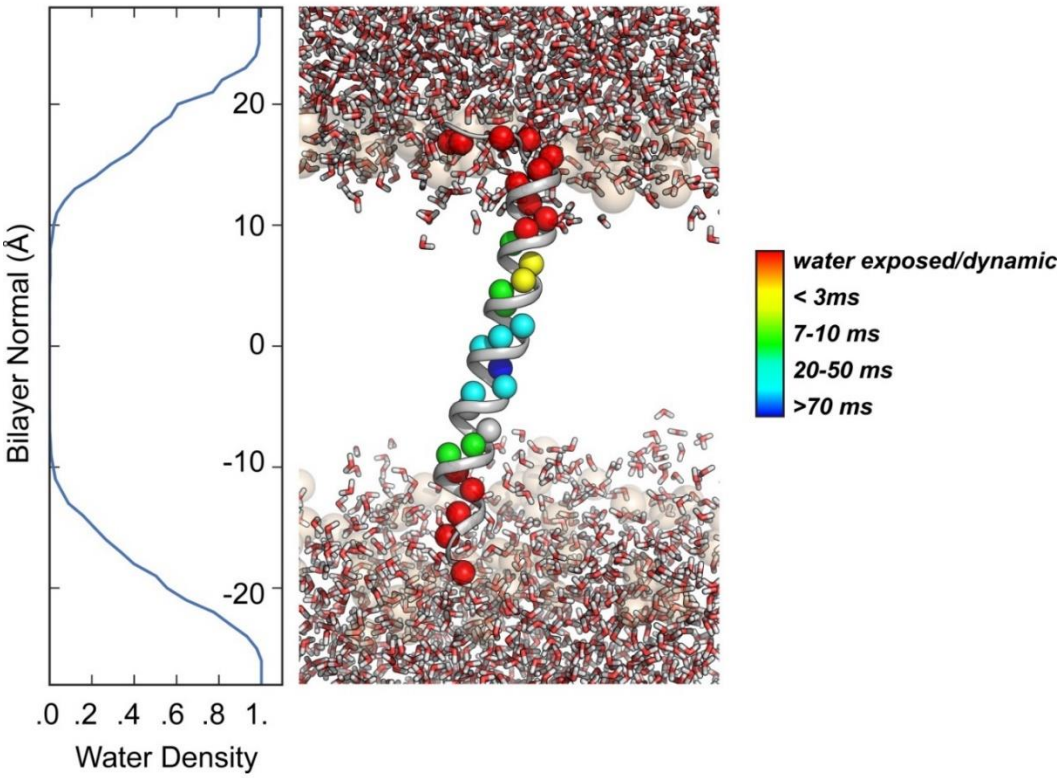

Figure 8. Water-exposed residues highlighted on the SLN structure obtained from molecular dynamics simulations.[319] **Left**: distribution of the water molecules as mapped during the molecular dynamics trajectories. **Right**: structure of SLN in lipid membranes. Red indicates residues that are too mobile to be observed in PISEMA but are assumed to be water-exposed. Otherwise, the residues are colored according to the mixing time (1–70 ms) at which the peak has a signal-to-noise ratio of eight or greater.

Chapter 5 - Mapping of SLN Conformational States Along the Enzymatic Pathway of SERCA

5.1 Introduction

The sarco(endo)plasmic reticulum Ca^{2+}-ATPase (SERCA) is a membrane transporter that is an essential component of muscle function. SERCA uses energy from ATP hydrolysis to pump two Ca^{2+} ions from the cytosol of muscle cells into the sarcoplasmic reticulum causing muscle relaxation.[150,248,328] This process is tightly regulated by interactions with peptides encoded by small open reading frames (smORFs) including sarcolipin (SLN),[116] phospholamban (PLN),[119] and the more recently identified myoregulin,[104] DWORF,[105] and sarcolambans (in *Drosophila*).[106] Significantly, mutations and abnormal expression of SLN and PLN can lead to pathological conditions in humans as they result in poor Ca^{2+} handling by SERCA,[110-114,125] and further research may also unveil similar outcomes for the newly identified regulators of SERCA.

Given the potential pathological impact of Ca^{2+} mishandling, understanding how these peptides interact with and regulate SERCA is important; especially crucial is discerning how their structural differences lead to disparate effects on SERCA's activity. Both SLN and PLN inhibit SERCA, decreasing its apparent calcium affinity[119,120,329,330] and bind within the groove formed by TM helices M2, M4, M6, and M9 of SERCA.[123,158,159,331-333] However, SLN, but not PLN, also uncouples SERCA's Ca^{2+} transport and ATP hydrolysis activities.[121-123] These functional differences between SLN and PLN have physiological relevance. PLN is primarily expressed in cardiac muscle[119] and regulates SERCA2a.[101,102] Phosphorylation of PLN by protein kinase A (PKA) through the β-adrenergic response relieves inhibition, allowing SERCA to pump more Ca^{2+} enhancing cardiac relaxation.[113,330] SLN on the other hand is expressed in skeletal muscle and in the heart atria.[109,117,118] SLN regulates both SERCA1a and SERCA2a, as SERCA1a is expressed in fast-twitch skeletal muscle[99,100] and SERCA2a in cardiac and slow-twitch

skeletal muscle.[101,102] Compared to PLN, less is known about SLN's role in modulating cardiac function, but cardiac relaxation is impaired by SLN overexpression in atria and improved in SLN-knockout mice.[124-126] Likewise, although inhibition of SERCA by SLN can also be reversed through phosphorylation, the physiological role for this is much less clear than for PLN, however, it is known that preventing phosphorylation at Thr-5 of SLN by CaMKII in cardiac muscle can have adverse effects in mice and rats.[124-126] In skeletal muscle, SLN's uncoupling of SERCA's Ca^{2+} transport and ATPase activities leads to increased heat production,[121,122] which may play a key role in muscle-based thermogenesis as well as compensating for metabolic overload.[123,127,334]

SLN and PLN are functionally distinct, and while they are structurally similar in many ways, they accordingly have key structural differences.[123,335-337] Both peptides consist of a single-pass transmembrane helix with two domains, one of which is more hydrophilic.[142,338,339] The transmembrane helix of PLN crosses the bilayer with a tilt angle of ~15–20°,[256,340,341] while SLN has a tilt angle of ~24°.[144,145] Significantly, PLN is larger at 52 amino acids compared to SLN's 31 amino acids.[120] Their difference in length is largely due to PLN's cytoplasmic helix, whereas SLN has a much shorter cytosolic region that is unstructured.[142,341-343] PLN's conformational equilibrium and cytoplasmic domain play a key role in regulating SERCA. There are three main states of PLN: a ground state (T state), an excited state (R state), and a SERCA-bound state (B state).[253,332,333,344] In the T state, the cytoplasmic domain is bound to the lipid membrane, but in the R state, the cytoplasmic domain is detached from the membrane and unfolded. Both states inhibit SERCA. In the B state, the cytoplasmic domain is bound to SERCA, and PLN is no longer inhibitory. Phosphorylation of PLN at Ser-16 by PKA shifts the equilibrium to the B state reversing inhibition.[345] SLN is phosphorylated at Thr-5, but there is no model equivalent to

that of PLN that describes the structural effects of phosphorylation on SLN. Recent studies have suggested that the N-terminus of SLN, where Thr-5 is located, interacts with SERCA to cause uncoupling,[164,165] but more information is needed to verify how/if the N-terminus is involved in uncoupling for all species of SLN (this region is not highly conserved[120]). However, SLN does have a highly-conserved C-terminus/luminal tail that is critical for inhibiting SERCA's activity.[120] Overall, it is at least clear that the mechanisms of how SLN and PLN modify SERCA have distinctions.

Studies of SERCA by itself have led to a structural understanding of the changes SERCA undergoes during Ca^{2+} transport, as it has been crystallized at several different stages of the transport cycle.[150,259,261,346-348] And while there are several hypotheses as to how the interactions of SERCA with regulatory peptides affect SERCA's activity,[120,158,159,165,349] a detailed description of the molecular mechanism of action remains elusive. Here, preliminary data on the effects of phosphorylated SLN on SERCA's activity suggest that the N-terminus may have a role in modulating uncoupling. Furthermore, the structure of SLN bound to SERCA in different conformations has been further characterized using solid-state NMR spectroscopy (ssNMR) to enhance our understanding of the molecular mechanism of regulation.

5.2 Materials and Methods

5.2.1 Protein Preparation

Unlabeled, uniformly ^{15}N-labeled, and uniformly ^{13}C, ^{15}N-labeled human sarcolipin were purified from *E. coli* using methods described previously.[311,312] For selectively-labeled samples, the ML12 auxotrophic strain was utilized,[350] and SLN was expressed in

minimal media containing 100 mg/L of the desired unlabeled or isotopically-labeled amino acid(s) (leucine, valine, isoleucine, and tyrosine). SERCA1a from rabbit hind-leg muscle was purified into $C_{12}E_8$ detergent using reactive red affinity chromatography also as described previously.[250] Phosphorylated human SLN was synthesized using a microwave synthesizer (CEM Corporation). Phosphothreonine [Fmoc-Thr(PO(OBzl)OH)-OH (Merck, Darmstadt, Germany)] was coupled at 50 °C; subsequent deprotection steps were performed at room temperature and amino acids 1–4 were coupled at 50 °C to reduce the risk of dephosphorylation. The peptide was purified using reverse-phase HPLC similar to the recombinant SLN.

5.2.2 ATP Hydrolysis Assays

Reconstitution of SERCA with and without SLN as well as the coupled enzyme assays were completed following well-established protocols.[44,120,351-357] To reconstitute SERCA and SLN for use in the assays, 200 µg lipids (4:1 DOPC:DOPE) in chloroform were dried-down under N_2. The lipids were re-suspended with 1.3:1 (w/w) octaethylene glycol monododecyl ether ($C_{12}E_8$), 25 mM imidazole, 100 mM KCl, 5 mM $MgCl_2$, and 10 % glycerol. As needed, 14 µg SLN or phosphorylated SLN (pSLN) solubilized in $C_{12}E_8$ were added. Once the lipids were fully dissolved, 40 µg of SERCA in 0.1% (w/v) $C_{12}E_8$ was added. The samples were incubated with 70:1 w/w Biobeads SM2 (Bio-Rad, Cat. No. 152-3920) to $C_{12}E_8$ for 3 h at room temperature with gentle stirring to remove the detergent.

The ATPase activity of SERCA was measured by a coupled enzyme assay[44,351] that monitored the decrease in absorbance of NADH at 340 nm using a Spectramax plate

reader (Molecular Devices). For each well, 0.56 µg of the reconstituted SERCA with and without SLN or pSLN was used. For the assays where the crude SR was used in place of the reconstituted system, there was approximately 0.13 µg SERCA per well. The activity was measured as a function of calcium concentration at 37 °C. The assays with SR were also performed as a function of magnesium concentration. The assays were performed in triplicate and averaged. Data were fit to the Hill equation to obtain the V_{max} and K_{pCa}.

5.2.3 In vitro phosphorylation of SLN

Aliquots of 4 µg of SLN in methanol were dried down under a stream of N_2. The SLN was resuspended in kinase reaction buffer containing 2 mM DTT, 5 mM $MgCl_2$, 2 mM ATP, 40 mM HEPES, pH 7.5 and either 3% (w/v) $C_{12}E_8$, 2 mM DPC (*n*-dodecylphosphocholine), 1% (w/v) OG (*n*-octyl-β-D-glucopyranoside), 1% (w/v) DDM (*n*-dodecyl-β-D-maltoside), or 0.5% (w/v) OG. To initiate the phosphorylation reaction, 0.8 µL CaMKII was added. The reaction was incubated overnight at 33 °C. SDS-PAGE was performed with 2 µg of SLN from each reaction followed by a Western blot transfer. Phosphorylation was detected with an anti-phosphothreonine antibody.

5.2.4 MAS ssNMR Sample Preparation

All lipids were purchased from Avanti Polar Lipids (Alabaster, AL). SLN alone samples were prepared by co-dissolving 1.2 mg uniformly ^{13}C,^{15}N-labeled SLN in methanol with 14 mg deuterated DMPC lipids. The methanol was evaporated off under a stream of N_2, and the dried down lipids and SLN were lyophilized overnight. The lipids and SLN were resuspended in 1 mL of MAS Buffer (20 mM HEPES, pH 7.0, 10 mM KCl, 2.5

mM $MgCl_2$, and 2.5% glycerol). The resuspension was centrifuged for 16 hrs at 4 °C and 70,000xg. The pellet was transferred to a MAS rotor.

For the samples with SERCA, 0.35 mg uniformly ^{13}C,^{15}N-labeled SLN in methanol was dissolved with 14 mg deuterated DMPC lipids. Again, the methanol was evaporated off under a stream of N_2, and the dried down lipids and SLN were lyophilized overnight. The lipids/SLN were re-solubilized with $C_{12}E_8$ and added to 8 mg SERCA in MAS Buffer. Bio-beads at a ratio of 30:1 with the detergent were added, and the solution was stirred gently at room temperature for 3 hours. The solution was placed on ice, removed from the Bio-beads, and centrifuged at 30,000 RPM at 4 °C for 1 hour. The pellet was resuspended in 1 mL of MAS Buffer with 2 mM EGTA and 2 mM AMPPCP or 2 mM $CaCl_2$ and 2 mM AMPPCP to promote the E2-AMPPCP and E1-AMPPCP states of SERCA, respectively. The vesicles were then centrifuged for 16 hrs at 4 °C at 70,000xg. The pellet was transferred to a MAS rotor.

5.2.5 Oriented Sample Preparation (Bicelles)

SERCA (8 mg) was dialyzed two times into 2x O-ssNMR buffer (20 mM HEPES, 50 mM KCl, 2.5 mM $MgCl_2$, 2.5%glycerol, and 0.02% NaN_3) with 200 µM EGTA to remove any Ca^{2+} still present after purification. Uniformly- or selectively-labeled ^{15}N SLN (0.25 mg/sample) was co-dissolved in MeOH with the lipids, 38.6 mg DMPC/POPC/DMPE-PEG2000 (4:1:0.01 molar ratio), and lyophilized overnight. The lipids/SLN were re-solubilized with $C_{12}E_8$ and added to SERCA in O-ssNMR Buffer. Bio-beads (30:1 ratio with detergent) were added and the solution was stirred gently at room temperature for 3 hours. The solution was placed on ice and removed from the Bio-beads via aspiration. The

solution was centrifuged at 50,000xg at 4 ˚C for 2 hours to pellet the vesicles. The vesicles were re-suspended with ~300 µL of buffer. Once the solution was homogeneously re-suspended, 6.1 mg of D6PC dissolved in 50 µL of O-ssNMR Buffer was added and mixed thoroughly. The sample was then concentrated to 160 µL using a 0.5 mL 10 kDa cutoff concentrator at 4ºC. Any compounds to modify the concentration of SERCA were added when the solution was ~400 µL This includes 2 mM EGTA, 2 mM $CaCl_2$, and 2 mM AMPPCP. The sample was transferred to a flat-bottom glass tube (New Era Enterprises) and tightly sealed with a polytetrafluoroethylene cap.

5.2.5 NMR spectroscopy

All the O-ssNMR NMR experiments were performed on a Varian VNMRS spectrometer with an ^{1}H operating frequency of 700 MHz. The spectrometer was equipped with a low-E bicelle probe built by the RF program at the National High Magnetic Field Laboratory (NHMFL) in Florida.[313] All spectra were acquired at 25 °C following previous parameters used for PISEMA experiments of SLN in DMPC-POPC-DHPC bicelles.[144] The MAS ssNMR data were acquired on a 600 MHz Varian spectrometer with a 3.2 mm BioMAS™ probe (Agilent Technologies) at a spinning speed of 12.0 kHz and a temperature of 2 °C, unless otherwise mentioned in figure captions. DARR and NCA spectra were acquired using a dual acquisition pulse sequence as previously described.[145,358] All of the NMR data were processed using NMRPipe[199] and analyzed using *SPARKY*.[200]

5.3 Results and Discussion

Phosphorylated SLN

We assessed whether CaMKII can phosphorylate human SLN in order to use the pSLN in further structural studies. To this end, SLN was incubated in kinase reaction buffer with ATP and CaMKII, and phosphorylation was detected with an anti-phosphothreonine antibody. The presence of bands in the lanes with CaMKII and SLN in **Figure 1** demonstrated that human SLN was phosphorylated by CaMKII, which is in agreement with a previous study.[124] Given that there is only one threonine in the N-terminus, phosphorylation was likely at Thr-5 (there are two other threonines, Thr-13 and Thr-18, but they are embedded within the membrane). Additionally, the extent of phosphorylation of SLN was dependent on the type of detergent used for solubilization, which highlights the importance of the specific type of membrane mimetic used to study membrane proteins. SLN in $C_{12}E_8$ displayed the highest level of phosphorylation based on signal intensity (all the reaction lanes were loaded with the same amount of SLN). Detergents can affect the structure of proteins, so it may be that Thr-5 is more accessible to CaMKII in $C_{12}E_8$ compared to the other detergents. In fact, previous NMR studies have shown that the unstructured length of the N-terminus varies depending on the detergent/lipid.[141,142,145] This experiment could have also been affected by the solubility of SLN in the detergents, but the samples were clear prior to initiating the kinase reaction and SLN does not dissolve readily in $C_{12}E_8$ suggesting another factor is the cause for the detergent-dependent phosphorylation. The low levels of phosphorylation could also be due to inhibition of CaMKII by certain detergents rather than the accessibility of SLN's N-terminus, but PLN in OG is readily phosphorylated by CaMKII whereas SLN in OG is not (**Fig. 1**). It would be interesting to see if using lipids could increase the level of phosphorylation enough to be

amenable to studying pSLN via NMR, which would be a step forward in determining the mechanism of pSLN's effect on SERCA.

Several studies do agree that Thr-5 is the site of phosphorylation.[124-126] (This distinction was more important for these studies as they used mouse and rabbit sequences of SLN, so Ser-4 was a potential site of phosphorylation.[124-126] In the human sequence, this residue is an asparagine.) However, both CaMKII and STK16 have been proposed as the responsible kinase based on 1) *in vitro* assays showing that CaMKII phosphorylated SLN[124] or 2) changes in the Ca^{2+} uptake of microsomes co-expressing SERCA and NF-SLN (tagged with a FLAG epitope at the N-terminus) with and without STK16.[359] This data provides further evidence that CaMKII can phosphorylate SLN, but the physiological mechanism and potential role of STK16 remains unclear.

To further investigate the potential role of SLN phosphorylation, the effects of synthetic pSLN on the ATP hydrolysis activity of SERCA were observed and compared to unphosphorylated SLN for the first time (**Fig. 2**). *In vitro* assays with the proteins reconstituted in lipids were performed with and without the calcium ionophore, A23187. The presence of the ionophore prevents the formation of a Ca^{2+} gradient across the vesicle membrane, which can cause back inhibition of SERCA. When there was no Ca^{2+} gradient present, pSLN did not alter SERCA's apparent calcium affinity (K_{pCa}) compared to SERCA by itself, whereas unphosphorylated SLN decreased the apparent calcium affinity (**Fig. 2B**). Thus, it appears that pSLN does not inhibit SERCA like SLN. SERCA's V_{max} was slightly affected by SLN compared to SERCA alone, but phosphorylation of SLN did not affect the V_{max} relative to SLN (**Fig. 2C**). Interestingly, in the absence of the ionophore (i.e. a Ca^{2+} gradient was present, which better mimics physiological conditions), SLN still decreased SERCA's apparent Ca^{2+}-affinity, but this apparent affinity was only partially

restored by phosphorylation (**Fig. 2B**). However, pSLN did restore the V_{max} to SERCA-alone levels whereas SLN actually increased SERCA's V_{max} (**Fig. 2C**).

Thus far, studies investigating pSLN have mostly tested the effects of SLN phosphorylation via monitoring the cardiac myocyte contractility, which is several functional steps beyond the biochemical reaction performed by SERCA,[124,359] but one study did observe changes in Ca^{2+} uptake for microsomes isolated from HEK-293 cells.[359] Their data also showed a decrease in the K_{pCa} with SLN compared to SERCA alone, and that expressing STK16 with SLN and SERCA (presuming that STK16 phosphorylated SLN) reversed the inhibition by SLN. Even though the data presented here show only partial restoration of the apparent calcium affinity by pSLN when a Ca^{2+} gradient is present, the overall effects are consistent despite the differences in the assays used. The microsome-based assay by Gramolini et al.[359] measured the Ca^{2+} uptake whereas the assays here measured ATP hydrolysis. Significantly, the change in the apparent calcium affinity (ΔK_{pCa}) due to SLN as measured by other ATP hydrolysis assays is similar to the change observed here (~0.2 pCa units),[120,142,312,360,361] whereas previously reported Ca^{2+} uptake assays are not as consistent with the ΔK_{pCa} ranging from -0.15 to about -0.4 pCa units.[119,359] The decrease observed here in SERCA's apparent calcium affinity combined with the increase of the V_{max} in the presence of SLN and a Ca^{2+} gradient is suggestive of SLN's uncoupling of SERCA's Ca^{2+} transport and ATP hydrolysis activities. These preliminary data suggest that pSLN only partially restores the apparent calcium affinity while bringing the V_{max} back to SERCA alone levels and indicate that phosphorylation of Thr-5 in SLN could have a role in modulating the uncoupling of Ca^{2} transport and ATP hydrolysis in SERCA, but further studies are needed to validate these findings.

The effects of Mg^{2+} on SERCA's activity

In addition to studying the role of phosphorylation of SLN on SERCA's activity, the effect of Mg^{2+} was also studied. Both of the crystal structures of SLN in complex with SERCA were crystallized under high levels of Mg^{2+} at ~75 mM and 40 mM Mg^{2+} (PDB IDs: 3W5A and 4H1W, respectively),[158,159] which are much higher than the estimated physiological concentration of Mg^{2+} of ~1 mM in cardiac myocytes.[362] To examine whether SERCA is functional under those high Mg^{2+} conditions, the ATP hydrolysis of purified crude SR from rabbit was measured under several concentrations of Mg^{2+} using the same coupled enzyme assay as the reconstituted system. As **Figure 3** demonstrates, SERCA is essentially fully inhibited under the concentrations of Mg^{2+} used to crystallize the complex. Consistent with this observation, inhibition of SERCA by Mg^{2+} was reported previously with assays that measured Ca^{2+} uptake under concentrations of up to 10 mM free Mg^{2+}.[363,364] Inhibition of SERCA by high levels of Mg^{2+} is not surprising, as it was already known that Mg^2 can interact with the Ca^{2+} binding sites[365] but is not transported.[366] In fact, both of the published X-ray structures have Mg^{2+} bound in the Ca^{2+} binding sites of the transmembrane region. This raises questions as to how much these structures can tell us about the physiological mechanism of Ca^{2+} transport and inhibition by SLN. Both structures are interpreted as representing intermediates more similar to the $2Ca^{2+}$-E1 state than the E2 state.[158,159,161] Molecular dynamics studies support that this is not likely to be a state that is populated under physiological conditions.[349] Lastly, neither of these crystal structures had strong electron density for the terminal regions of SLN,[158,159] which do play a role in regulation and/or inhibition of SERCA.[120,124,126] Overall the finding that high concentrations of Mg^{2+} inhibit SERCA strongly suggest that more structural/activity studies are required on samples prepared under physiological conditions. In this regard, ssNMR

should be well-suited to these goals, as the samples can be prepared in a manner that maintains the proteins in environments that are more similar to physiological conditions, and these conditions can be dynamically altered to induce different states of SERCA and test the various structural models for those states.

MAS Sample Comparisons

MAS samples of SLN alone as well as the SLN+SERCA complex were prepared under conditions different than previously-published SLN alone samples in effort to overcome the limitations of previous sample preparations. As such, an understanding of the differences between both the SLN alone sample described here and the previously-published SLN alone sample[145] is needed to assess the resulting spectra. The SLN alone MAS sample described here included glycerol in the buffer as it is used to help stabilize SERCA in the complex samples, whereas the previous sample did not contain glycerol.[145] This sample was also pelleted at a much lower centrifuge speed than the previous sample. Significantly, there were clear differences in the SLN alone spectra from these two methods as shown in **Figure 4**. Several possible factors could contribute to the differences in peak appearance, but comparison of the DARR spectra for these samples (**Fig. 5**) does not indicate that the difference is likely due to aggregation as the linewidths for the hydrophobic residues are similar (**Fig. 5**), and aggregation would cause the lines to broaden. Furthermore, the peaks corresponding to isoleucines, leucines, and valines overlay well indicating that SLN is still in an α-helical conformation and not misfolded, as the peaks would then shift substantially. It should be noted that some peaks (e.g. Glu-7, Phe-9, Phe-12) were not visible in the DARR spectrum from the SLN alone sample prepared here compared to the published sample.[145] Many factors can alter the exact

appearance of the final spectra in this type of experiment. It has been an observed in the lab that even the spinning speed and duration of pelleting the sample can significantly affect the spectra. A hypothesis for this observation is that the amount of water (and thus level of hydration) in the sample will decrease as the pellet is more tightly packed when centrifuged longer or at a higher speed, and the degree of hydration will influence these types of spectra.[297] There is also evidence that the glycerol content can affect spectra probably due to changes in the sample viscosity,[367] but this may not account for the differences here as increased viscosity should lead to broader lines. Interestingly, the peaks that were not observed in the DARR spectra presented here are part of the same region of SLN (near the N-terminus of the TM region or domain Ib), which is known to be more dynamic than the rest of the TM region,[71,142] so it may be that differences in hydration have altered the dynamics of this region compared to the previous sample, decreasing the efficiency of the cross-polarization. Clearly, further studies should be completed to elucidate the reasons for these differences.

Like the SLN alone sample, the SLN+SERCA complex samples may also have more conformational heterogeneity compared to the previously-published SLN alone sample.[145] The NCA spectra for these samples are more similar to each other (**Fig. 6**) than to the published SLN alone NCA spectrum. Furthermore, the peaks in these NCA spectra shifted between the SLN alone spectrum and both of the SLN+SERCA (E1-AMPPCP and E2-AMPPCP) spectra, which was expected as each of these samples are different. However, it is not possible to make assignments as they are not similar enough to the previously assigned spectra. Importantly, the DARR spectra (**Fig. 7**) for these samples do not indicate that aggregation is an issue for the SLN+SERCA samples either as they have similar linewidths to the SLN alone sample. Significantly, both of these spectra had

reasonable signal intensity compared to the SLN alone spectra when accounting for the decreased quantity of labeled SLN in the complex samples. Thus, although the NCA spectra indicated there was conformational heterogeneity in these samples, it may be that this is a current limitation of preparing samples with SERCA.

Structural Studies of the SLN and SERCA Complex

While more studies are required to reconcile the differences in the MAS data as already discussed, the preliminary findings from the other spectra acquired with these samples still indicated several interesting points about the SLN+SERCA complex. SLN has historically been assumed to behave the same as PLN, so when cross-linking data with PLN suggested that elevated Ca^{2+} levels (16 μM or less) caused PLN to dissociate from SERCA,[332,368,369] a model was proposed in which both PLN and SLN dissociate from SERCA when Ca^{2+} binds causing the relief of inhibition.[368] A former student in the lab hypothesized that Ca^{2+} binding to SERCA instead caused structural changes that affected the efficiency of cross-linking at the specific sites previously used.[370] As such, collaborators in the Periasamy lab monitored cross-linking between two alternate sites in SLN: L8C-SLN to W932C-SERCA and S936C-SERCA (Periasamy lab, data not shown). The cross-linking efficiency was not only immune to high Ca^{2+} concentrations (100 μM), but even showed a small increase. A later paper from the Periasamy lab showed that other sites in SLN cross-link to SERCA more efficiently compared to PLN at high Ca^{2+} concentrations (100 μM) as well.[123] One caveat from the studies by the Periasamy lab is that all of their experiments utilized the mouse SLN, and assay data has indicated that there are functional differences between the human and mouse SLN.[120,123,142,164,312,360,361] As such, we sought to determine whether human SLN is bound to E1-AMPPCP SERCA

under our ssNMR sample conditions. The signal intensity for the experiment in **Figure 8** is dependent upon the dynamics of the protein, which should be different for SLN alone (3.8 kDa) compared to SLN bound to the 110 kDa SERCA. The intensity of the signal for the SLN alone sample changed between 2 °C and 25 °C, but the intensity did not change when SERCA with Ca^{2+} and AMPPCP was present (**Fig. 8**). Thus, the dynamics of SLN have changed in the presence of SERCA, which suggests that even with Ca^{2+} and nucleotide present, SLN still binds to SERCA rather than dissociating. It should be noted that this is not the ideal method to observe binding as other factors could be influencing the signal intensity; the viscosity and hydration of the sample with SERCA were both likely very different than the SLN alone sample (an additional 8 mg of protein were packed into the 30 µL sample), and these are both factors that could also affect the dynamics. A gel shift assay was attempted under the conditions used in the ssNMR sample, but the amount of lipids caused too much smearing. While there is not yet a definitive answer for whether human SLN binds to SERCA with Ca^{2+} present, these data are congruent with the model that SLN behaves more like a subunit of SERCA and that relief of inhibition is not due to dissociation upon Ca^{2+} binding.

Preliminary INEPT data, which provides information about mobile residues, was also acquired for these MAS samples. Overlaying the SLN alone sample here with the previously published data[145] further indicated that aggregation was not an issue as the spectra overlaid well (**Fig. 9**). For the SLN alone spectra, the residues of SLN's N- and C-termini are observed (**Figs. 9 and 10**). When SERCA is present in either the E2-AMPPCP or E1-AMPPCP states, the peaks corresponding to the C-terminal/luminal tail residues, e.g. Tyr-31 and Glu-30, decrease in intensity indicating that they have become immobilized and are likely bound to SERCA (**Fig. 10**). However, the N-terminal residues

are still observed, and thus do not seem to interact strongly with SERCA in these states. A previous study observed that the luminal tail is immobilized when SLN is bound to SERCA,[163] and another study's assay and mutagenesis data found that the luminal tail was critical to SLN's inhibition of SERCA, which led to their conjecture that it binds to the loop between M1 and M2 of SERCA.[120] These interactions would lead to inhibition through limiting the motion of these helices, which undergo significant structural rearrangements during Ca^{2+} transport. Both of those studies are consistent with the interpretation of the INEPT spectra shown here in **Fig. 10**, however other recent studies have suggested that the N-terminus of SLN also interacts with SERCA to cause uncoupling,[164,165] which is not consistent with the data presented here as these residues are still visible in the INEPT spectra. While these INEPT experiments should be repeated and verified, there are factors that could account for this discrepancy. The studies that found interactions between the N-terminus and SERCA did not use human SLN, but rabbit[165] and mouse[164] SLN, which have key differences (**Fig. 11**). Significantly, both studies found important salt bridges between Glu-2 of SLN with Arg-324 of SERCA[164] or Arg-324 and Lys-328.[165] The study by the Periasamy lab also found a salt-bridge between Arg-3 of SLN and Glu-34 of SERCA.[164] However, in human SLN the amino acids at positions 2 and 3 are glycine and isoleucine, respectively (**Fig. 11**); neither of these residues would form a salt-bridge. Further indication that there may be important differences in SLN depending on these sequence differences is that the biochemical assay data are also not consistent between human and other species' SLN. In our data, we see a decrease of ~0.2 pCa units in SERCA's apparent calcium affinity (**Fig. 2**), which agrees with several other studies that measured ATP hydrolysis in the presence of human SLN by other labs.[120,142,312,360,361] However, the Periasamy lab sees no change in the apparent calcium affinity of SERCA compared to mouse SLN and SERCA.[123,164] In addition to using mouse SLN rather than

human SLN, the Periasamy lab also uses microsomes from HEK293 cells instead of fully reconstituting the proteins, and they measure ATP hydrolysis with the Biomol green reagent whereas many of the other studies used the NADH-based coupled-enzyme assay as we do.[120,123,142,164,312,360,361] A significant difference between the NADH-based coupled-enzyme assay and the Biomol green method is that ATP is not regenerated in the Biomol green assay, and ADP is known to have a regulatory effect on SERCA,[371] therefore its accumulation could affect activity. Lastly, mutagenesis experiments demonstrate that the luminal tail is critical for SLN's inhibition of SERCA,[120] and it is highly conserved (with 100% identity) among mammals whereas the N-terminus is much more variable (see **Fig. 11** and ref. 120), so it seems highly likely the luminal tail would have the more important role in the fundamental mammalian processes of uncoupling and heat production. Overall, the role each terminus plays in how SLN affects SERCA is still not fully clear and more detailed studies need to be completed to elucidate the mechanism of uncoupling, however, the data presented here are consistent with the model that the luminal tail is key for this process.

In addition to using MAS ssNMR to investigate the SLN+SERCA complex, O-ssNMR was also used to monitor the topology of SLN bound to SERCA under different conditions. With the PISEMA experiment, both the tilt and rotation angle of SLN in bicelles can be determined. Previously, the high-resolution structure of SLN in lipid bilayers using O-ssNMR was calculated to have a tilt angle of 24˚±1˚ with respect to the membrane normal and a rotation angle of 57°± 5°.[145] This topology is conserved with different membrane mimetic systems[144] as well as the presence of nucleotide or Ca^{2+}.[370] This is likely due to stringent restrictions placed on the tilt and rotation angle by the interfacial residues W23, R27, and R6.[144,145] Here, uniformly ^{15}N-labeled SLN was reconstituted with

SERCA in bicelles with EGTA and AMPPCP to mimic the E2-ATP state of SERCA, and then Ca^{2+} was added to induce the E1-ATP state of SERCA (**Fig. 12**). The tilt and rotation of SLN are similar in presence of both states of SERCA; however, there are clear changes between the spectra. To assess these changes, we used selectively-labeled samples to be able to assign the PISA wheel for the SLN+SERCA complex. Three main labeling schemes were used: 1) ^{15}N-labeled leucines 2) ^{15}N-labeled isoleucines and 3) all residues were ^{15}N-labeled except leucines, isoleucines, and valines. Spectra from these selectively-labeled samples were compared to the uniformly ^{15}N-labeled SLN alone spectrum (**Fig. 13**) prior to being used to make samples with SERCA and matched the previous assignments. These labeled SLN peptides were then used for complex samples prepared the same way as the uniformly ^{15}N-labeled SLN complex sample, in which 1) EGTA and AMPPCP were added to the bicelle, and 2) the PISEMA spectrum acquired, then 3) $CaCl_2$ was added, and 4) the spectrum was re-acquired. These samples helped identify changes that would not have been observed easily otherwise. For example, in the ^{15}N-leucine labeled sample, an extra peak was observed upon the addition of $CaCl_2$ (**Fig. 14A**), which is likely L10 based on both a previous assignment[147] and on the periodicity of the PISA wheel (the only other leucine is Leu-8, which would appear on the opposite side of the wheel). This indicates that the N-terminus of the TM region of SLN becomes more helical when Ca^{2+} binds to SERCA. As **Figure 14B** shows, with the ^{15}N-Ile-labeled SLN+SERCA samples, no extra peaks were observed, but there were slight changes in the spectra. The selectively-labeled samples allowed us to make estimated assignments of the uniformly ^{15}N-labeled SLN+SERCA samples (**Fig. 15,** see also **Table 1**). While these assignments cover most of the TM region of SLN and therefore, the PISA wheel, some of the peaks outside the wheel (110-125 ppm and ~0.8 kHz) show the most significant changes (**Fig. 15**). These were not able to be assigned using the labeling schemes

described here, but future studies should use other labeling schemes to assign these residues, as they may help to further elucidate how SLN interacts differently with SERCA (with AMPPCP bound) depending on whether Ca^{2+} is also bound or not.

Unfortunately, these data cannot tell us about the changes in SERCA's structure due to SLN binding or how SERCA changes with and without Ca^{2+} with SLN bound. Structural studies of SERCA reveal that when SERCA transitions from the E2 to E1 states, the groove formed by M2, M4, M6, and M9 collapses due to the movements of M1 and M2.[150] This observation contributed to the hypothesis that PLN and SLN dissociate from SERCA when Ca^{2+} is bound, but the MAS and O-ssNMR data presented here as well as other published data[123] indicate that SLN does not dissociate from SERCA when Ca^{2+} binds. Furthermore, structural transitions in the TM region must occur for SERCA to transport Ca^{2+} from the cytosol to the lumen. As SLN remains bound to SERCA[123] and seems to maintain the same tilt and rotation angles whether Ca^{2+} is bound to SERCA or not (**Fig. 15**), the interactions of SERCA's TMs 2,4,6 and 9 with SLN must change in some manner. Indeed, the change in the efficiency at different cross-linking sites due to the presence of Ca^{2+} (Periasamy lab, data not shown) supports that SLN's interactions with SERCA are different with and without Ca^{2+}. Some studies have suggested that SLN stabilizes an E2 state of SERCA[120] whereas other studies suggest that SLN stabilizes an E1 state.[158,159,165] As such, it seems reasonable to propose that SLN forms a wedge that interferes with the movement of M1 and M2 contributing to the decrease in SERCA's apparent calcium affinity (**Fig. 16**). Further studies investigating the changes in the interactions between SLN and SERCA in different states, including molecular dynamics simulations with experimental data from ssNMR, may help illuminate some of the remaining questions.

Additionally, the roles of the termini and the mechanism of uncoupling are still unclear. Normally, after nucleotide and Ca^{2+} binding to SERCA, the phosphoryl transfer causes changes in the cytoplasmic domains, which are connected to conformational changes in the TM region leading to Ca^{2+} occlusion.[150,348] This results in the tight coupling between ATP hydrolysis and Ca^{2+} occlusion.[150,348] It is unclear whether SLN disrupts this process causing slippage of the Ca^{2+} back into the cytosol or whether it promotes the SERCA-mediated passive leak of Ca^{2+} from the lumen to the cytosol without the concurrent production of ATP.[96,122,372,373] Recent studies proposed that salt-bridges between the N-terminus of SLN and the cytosolic portion of M4 in SERCA cause the uncoupling of ATP hydrolysis and Ca^{2+} transport through altering Ca^{2+}-binding site II[165] or interfering with TM sliding.[164] However, the conclusions from those studies do not entirely account for the fact that the N-terminus of human SLN could not form salt-bridges quite like the rabbit or mouse sarcolipin sequences used in the studies, nor do they consider the 100% sequence conservation in the luminal tail of SLN among mammals. Furthermore, the preliminary INEPT data suggested that the N-terminus does not interact with SERCA, but that the luminal tail does. It should be noted that the study by Autry et al. indicated that the Glu-2 salt bridge to SERCA could be replaced by Glu-7, which is highly conserved and present in the human sequence.[165] However, more studies are needed to elucidate how SLN uncouples Ca^{2+} transport and ATP hydrolysis in SERCA as well as if there are differences depending on the species-specific N-terminal sequences. Lastly, although SLN alters SERCA's activity differently than PLN and there is no evidence yet that SLN has T, R, and B states like PLN, phosphorylation of SLN's N-terminus does appear to reverse inhibition, indicating it does play a regulatory role similar to the cytoplasmic helix of PLN. It is likely that structural studies of pSLN will help to elucidate

both the role of the N-terminus and the mechanism of uncoupling. Overall, much remains to be understood about how SERCA's activity is regulated by SLN.

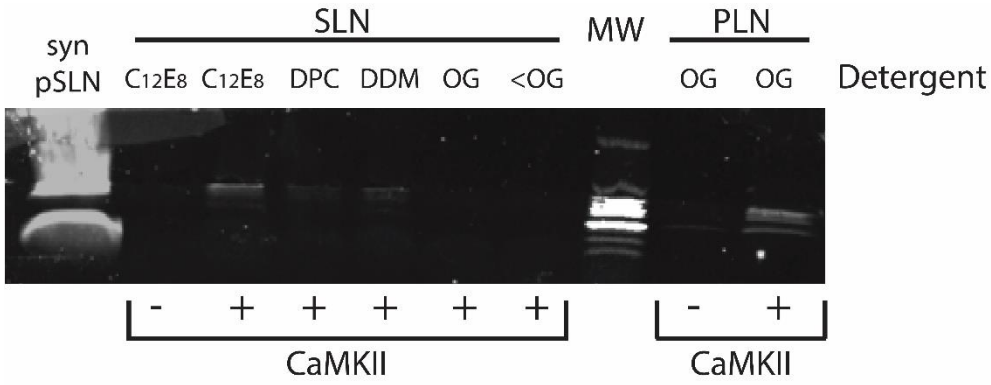

Figure 1. Phosphorylation of SLN by CaMKII. The phosphorylation reaction was carried out overnight at 33 °C and detected using an anti-phosphothreonine antibody. Synthetic pSLN (syn pSLN) was included as a control for ensuring the antibody detected pSLN. PLN was also included as a control to ensure that the CaMKII was active. The remaining reactions contained SLN solubilized in different detergents. Without CaMKII, no phosphorylation was detected, but with CaMKII, phosphorylation was detected in the $C_{12}E_8$ reaction, and there is also a faint band for the reaction in DDM (*n*-dodecyl β-D-maltoside). No phosphorylation was detected for the reactions in DPC or the two different concentrations of OG (*n*-octyl-β-D-glucoside).

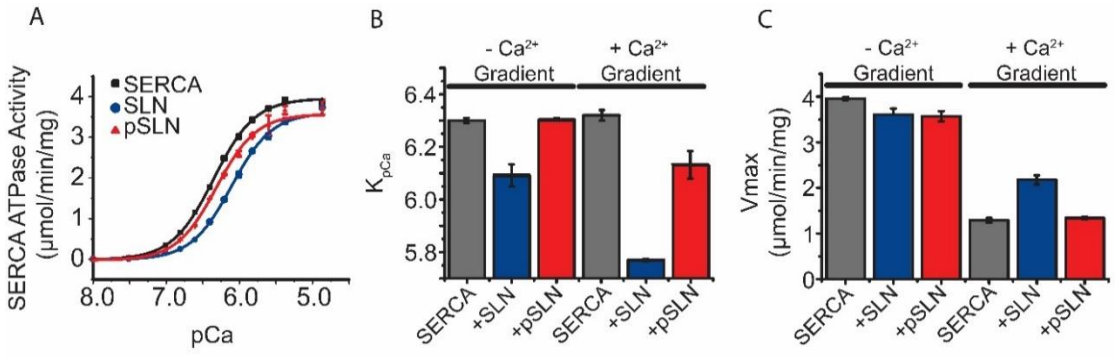

Figure 2. ATP hydrolysis assays with pSLN. **A**) The raw data for the ATP hydrolysis assay when the ionophore A23187 is present. The data from the assays with and without ionophore were fit to the Hill equation to extract the **B**) K_{pCa} and **C**) V_{max} values.

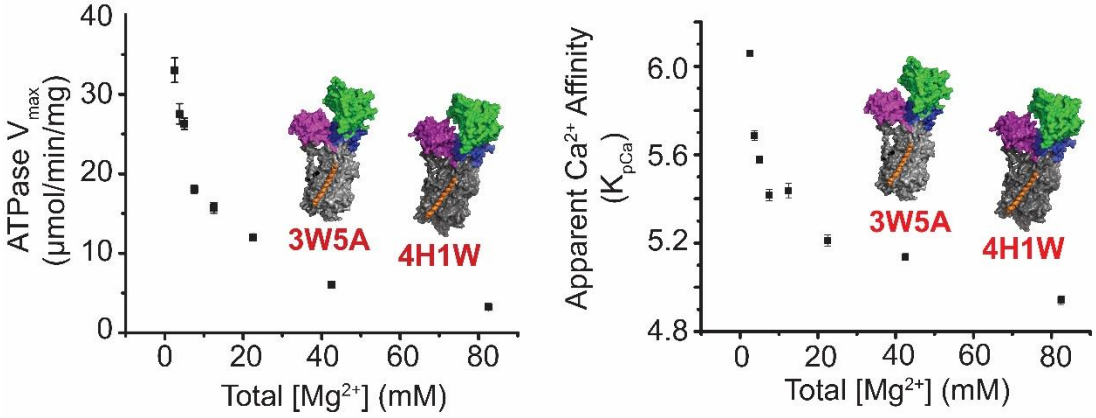

Figure 3. ATP hydrolysis assays at various concentrations of Mg^{2+}. The ATPase activity of SERCA was measured using the normal range of pCa values, but under several concentrations of $MgCl_2$ as well. These data were fit to the Hill equation to obtain the V_{max} and K_{pCa} values for a range of Mg^{2+} concentrations including those near to what was used to crystallize the SLN and SERCA complex (3W5A and 4H1W at 40 mM[158] and ~75 mM[159] [Mg^{2+}], respectively).

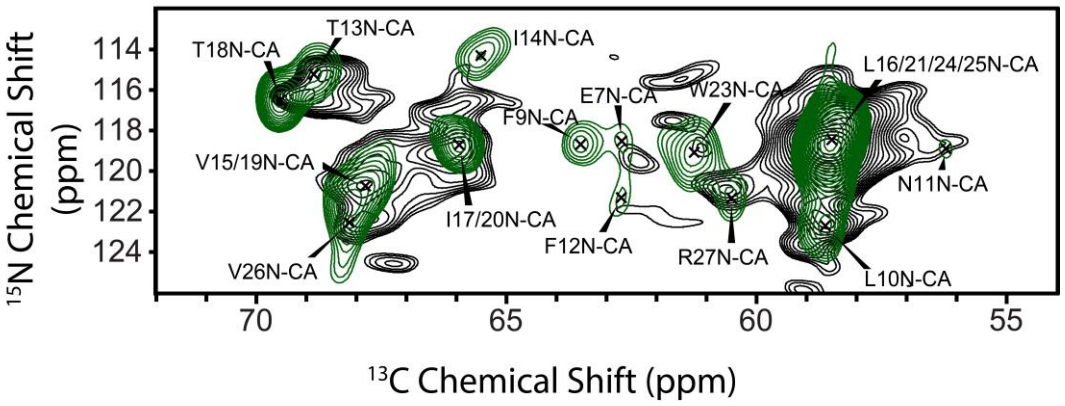

Figure 4. Comparison of NCA spectrum for SLN alone to previously published data. The data from glycerol/low centrifuge speed preparation are presented here in black whereas the previously published data (including previously proposed assignments)[145] are in green. These spectra do not overlay well suggesting that the data here represent a sample that has more conformational heterogeneity, which could be due to several factors related to the sample preparation.

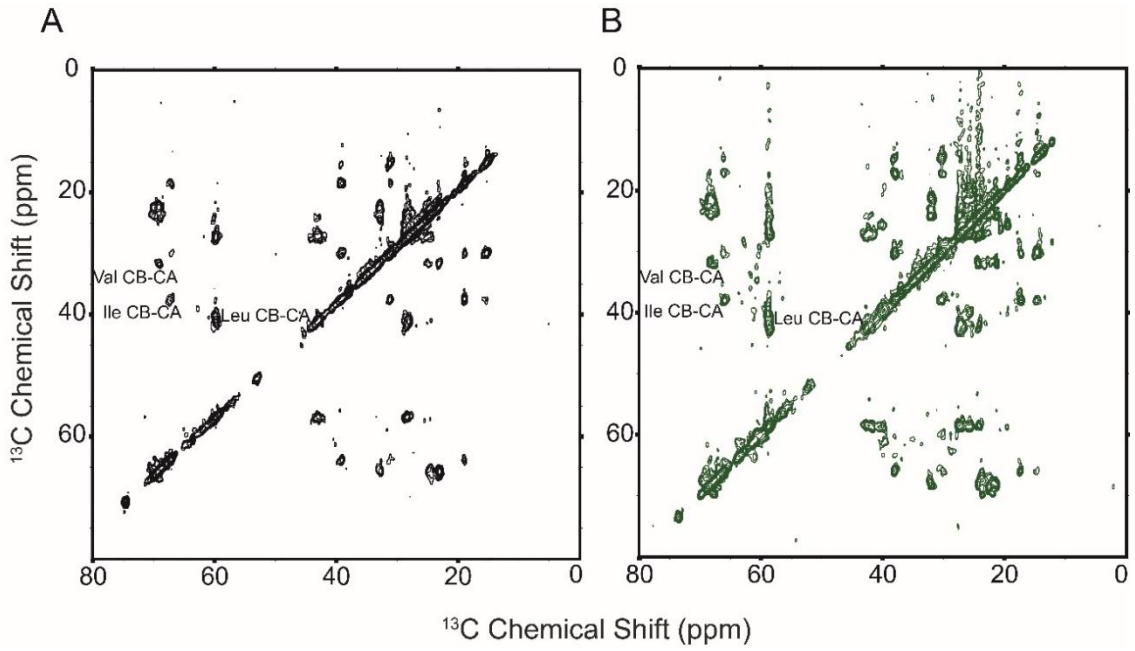

Figure 5. Comparison of the DARR data for the SLN alone sample from this work (**A**) as well as the previously published data[145] (**B**). The peaks corresponding to valines, isoleucines, and leucines overlay well, but there are differences in the number of peaks observed in this area of the spectra. For example, the spectrum in **B** has more peaks that were assigned to Glu-7, Phe-9, and Phe-12. However, the linewidths of the hydrophobic residues remain narrow (see associated table) indicating that the sample in (**A**) is not aggregated compared to (**B**). However, these spectra cannot be compared completely head-to-head as they were acquired using different mixing times (40 ms for **A** and 100 ms for **B**) and using different magnetic fields (600 MHz for **A** and 700 MHz for **B**), all of which can affect the parameters of the components being discussed.

	Linewidths	Linewidths
Leu CB-CA	125 Hz	106 Hz
Ile CB-CA	121 Hz	137 Hz
Val CB-CA	121 Hz	149 Hz

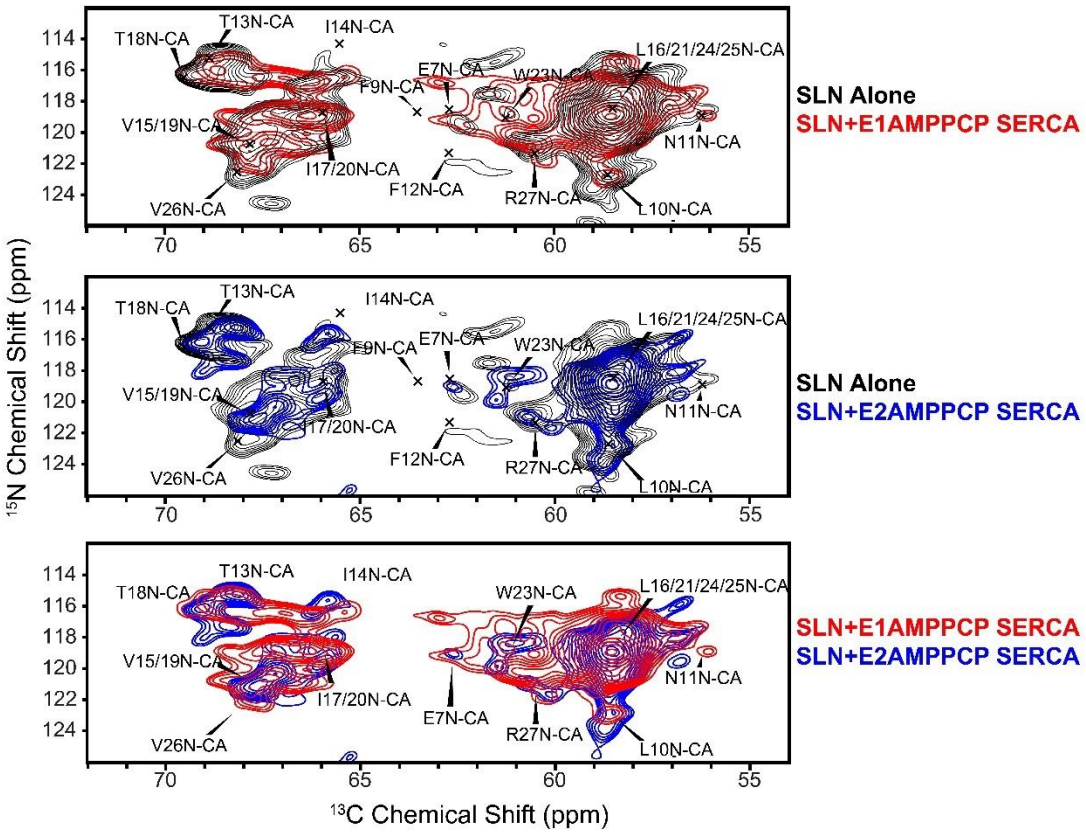

Figure 6. Comparison of all the NCA spectra for the samples prepared herein. The assignments based on the previously-published SLN alone sample[145] are marked by x's (also see **Fig. 4**). The SLN+E1AMPPCP SERCA and SLN+E2AMPPCP SERCA spectra are similar in appearance to the SLN alone spectrum (**Top** and **Middle**) indicating that they may all have conformational heterogeneity. Interestingly, there are shifts in some of the peaks (**Top**, **Middle**, and **Bottom**), which is congruent with the structure of SLN changing when it binds to different states of SERCA. However, these peaks cannot be assigned as the spectra are so different from the published assignments.

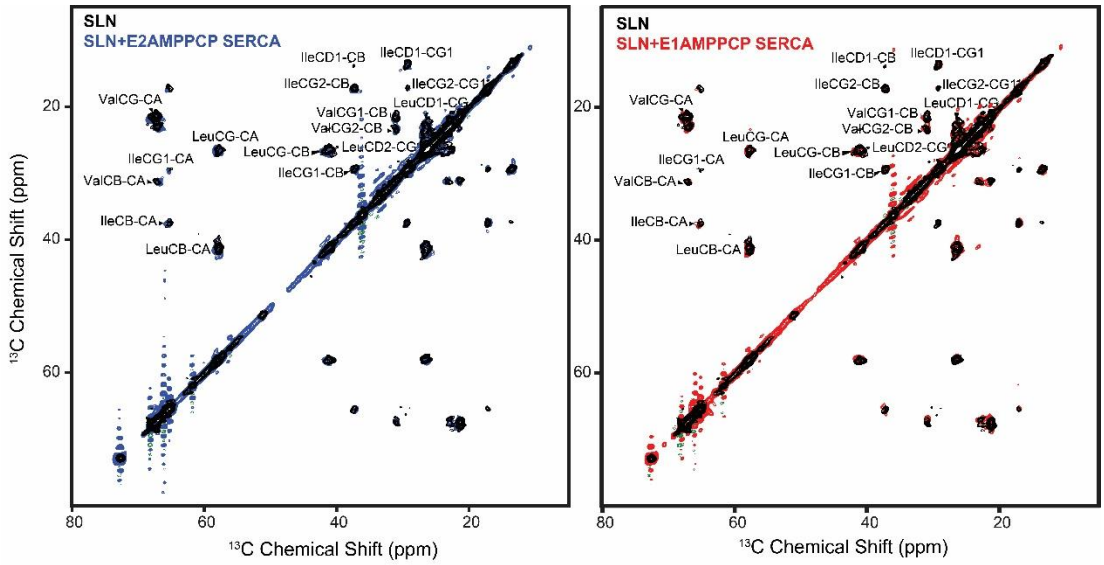

Figure 7. Comparison of the DARR data for the SLN alone sample with SLN+SERCA samples from this work. The peaks corresponding to the valines, isoleucines, and leucines overlay well, but the same peaks are missing the in the SLN+SERCA samples as the SLN alone sample compared to the previously published data[145] (**Fig. 5**). However, the linewidths of the hydrophobic residues are similar indicating that none of the samples are aggregated. All the spectra were acquired with a 20 ms mixing time.

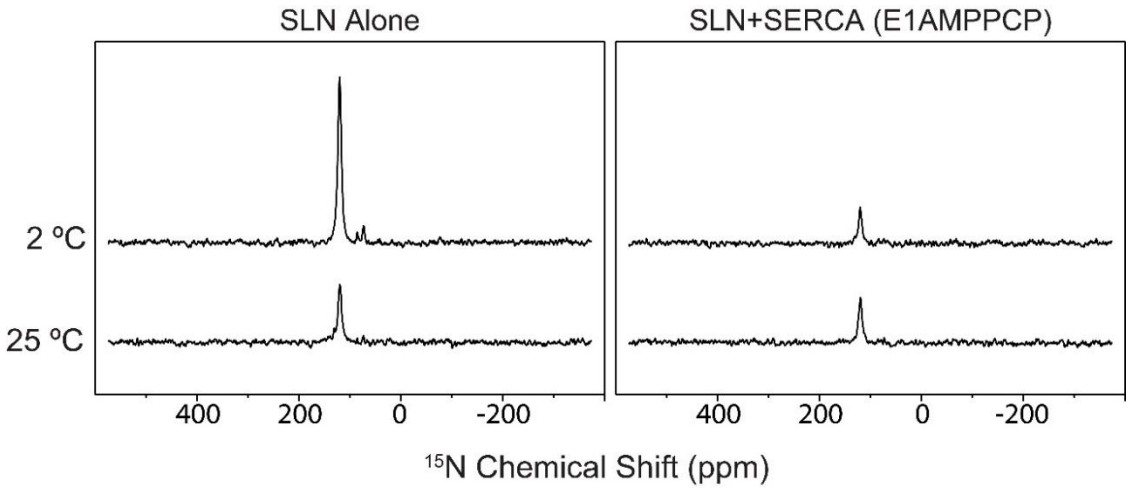

Figure 8. 1D MAS cross polarization spectra of SLN alone and SLN bound to SERCA in the E1-AMPPCP state. The signal intensity decreases from 2 °C to 25 °C for SLN by itself, which indicated that at 25 °C SLN has become more dynamic decreasing the efficiency of the cross-polarization. However, when SERCA (E1AMPPCP) is present, no such change in signal intensity is observed suggesting that even with Ca^{2+} and nucleotide present, SLN still binds to SERCA. This is not the ideal method to observe binding as other factors could be influencing the signal intensity. As such, other experiments should be completed to confirm that SLN is bound to E1-AMPPCP SERCA under our conditions.

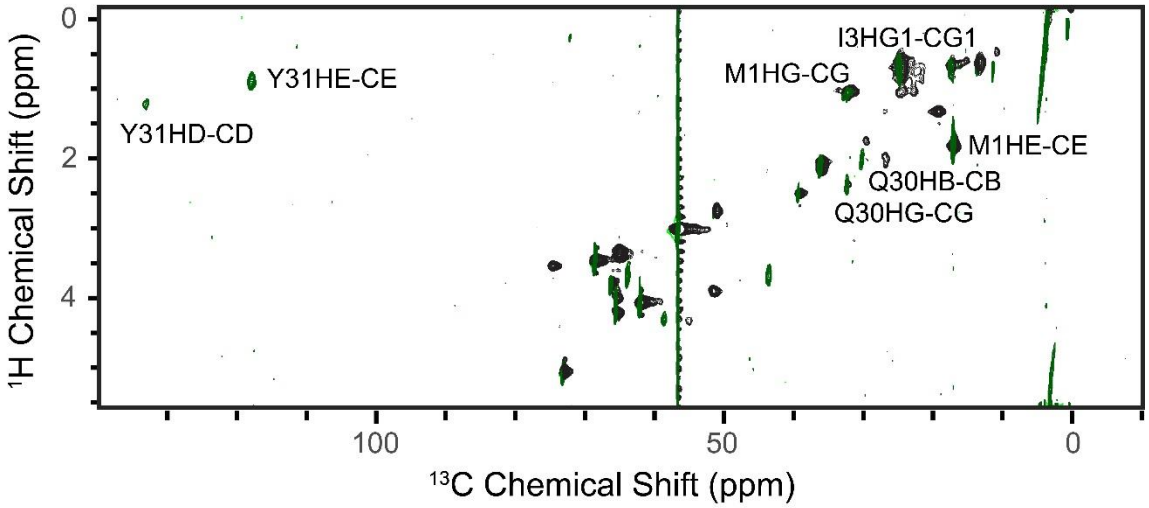

Figure 9. Comparison of SLN alone ref-INEPT (black) to previously published ref-INEPT (green).[145] The peaks corresponding to the N-terminus (I3 and M1) as well as the C-terminus/luminal tail (Q30) overlay well. Note that the Y31 peaks do not overlay as the published spectra was acquired with a smaller spectral width causing these peaks to be folded in the spectrum.

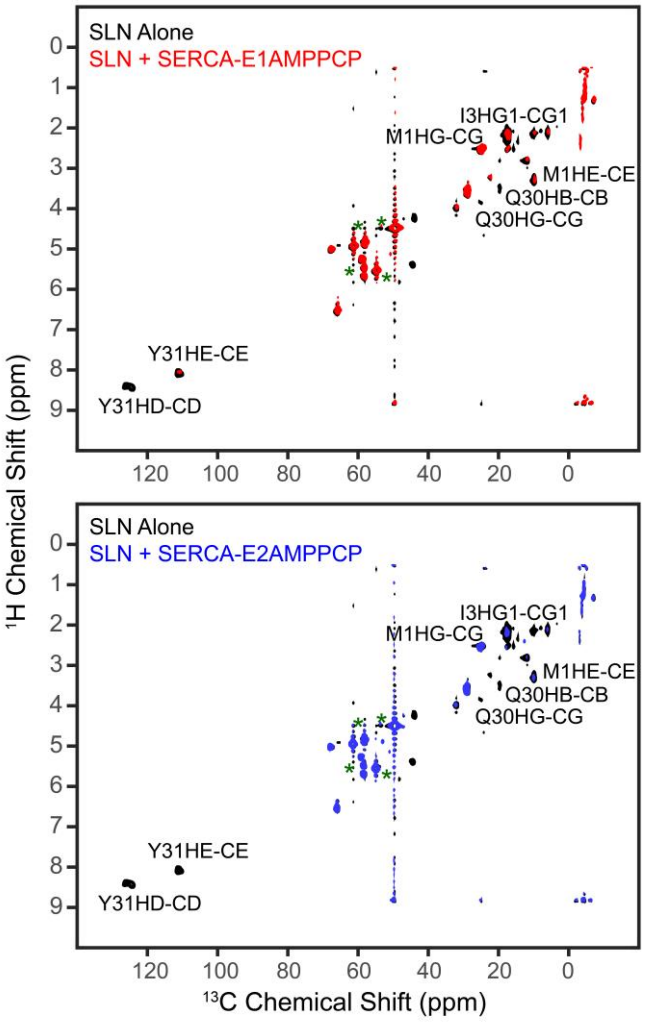

Figure 10. Overlays of the ref-INEPT spectra of SLN alone (black) and bound to SERCA either in the E1- (red, **Top**) or E2-AMPPCP (blue, **Bottom**) states. The spectra were acquired at 25 °C. The mobile residues of both the N- and C-termini are observed when SLN is by itself. However, when SERCA is present, the peaks corresponding to the residues in the C-terminus/luminal tail, e.g. Y31 and Q30, decrease in intensity (there is no blue left for either of these peaks, and only a small red peak for Y31HE-CE). This indicates that they are less mobile, and thus, likely binding to SERCA. In both states, the residues of the N-terminus are still visible indicating that they remain mobile and not bound to SERCA. These data were plotted at the same noise level to account for the different amounts of SLN used in the samples using a MATLAB script kindly provided by Dr. Manu Subrahmanian.

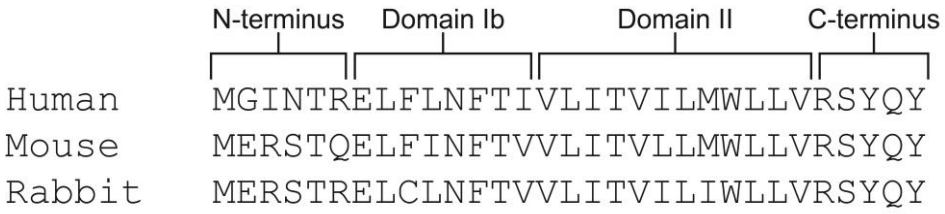

Figure 11. Sequence alignment of SLN for human, mouse, and rabbit. Although the C-terminus/luminal tail is perfectly conserved, the N-terminus is more variable.

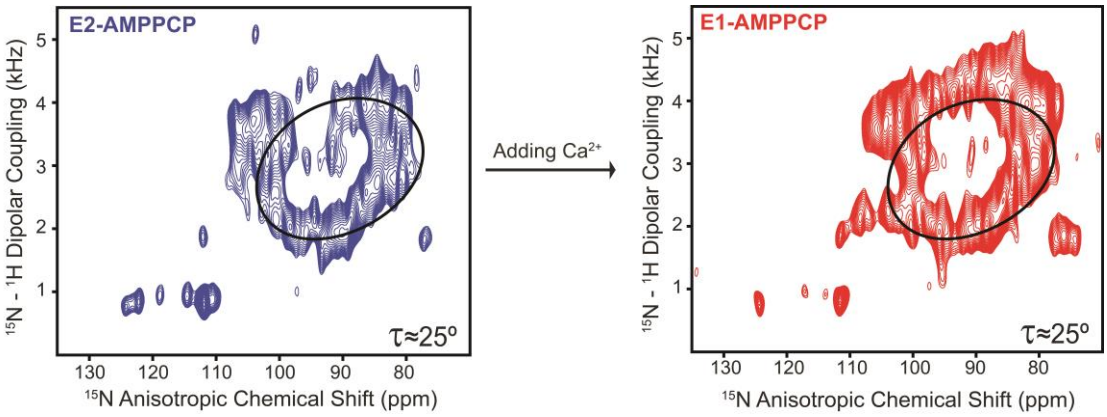

Figure 12. PISEMA spectra for SLN bound to SERCA in the E2-AMPPCP state and then with Ca^{2+} added (E1-AMPPCP). With this sample, and all subsequent complex samples, the bicelle sample was taken out of the probe, $CaCl_2$ was quickly added, and the sample was placed back into the instrument. Addition of Ca^{2+} clearly altered the appearance of the spectra, even though the tilt angle is similar between the two spectra, indicating that the Ca^{2+} is interacting with SERCA and affecting SLN. The free concentrations of ATP, Mg^{2+}, Ca^{2+}, and EGTA in these samples were calculated using the CHELATOR program[374] and are shown in the table below. Although EGTA and ATP have some affinity for Mg^{2+} and Ca^{2+}, respectively, the Mg^{2+} is predominantly bound to ATP and the Ca^{2+} to EGTA. There is enough free [Ca^{2+}] to bind to SERCA to form the E1-AMPPCP state.

	SLN+E2-AMPPCP	SLN+E1-AMPPCP
Total [ATP*]	2.0 mM	2.0 mM
Free [ATP*]	0.3 mM	0.1 mM
Total [Mg2+]	2.5 mM	2.5 mM
Free [Mg2+]	0.8 mM	1.3 mM
Total [Ca2+]	0 mM	4.0 mM
Free [Ca2+]	0 mM	1.3 mM
Total [EGTA]	2.0 mM	2.0 mM
Free [EGTA]	2.0 mM	0.001 mM

*****The CHELATOR program uses ATP, but the dissociation constants of AMPPCP for Ca^{2+} and Mg^{2+} are similar to ATP,[375] so this change should not dramatically affect the calculated free concentrations of these ions.

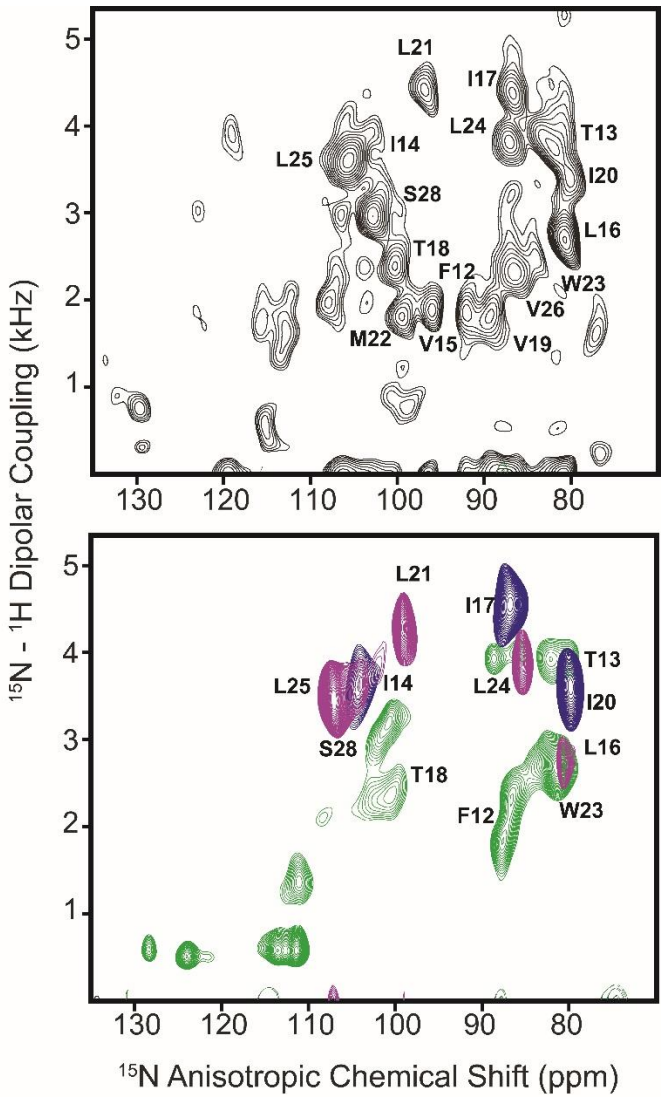

Figure 13. PISEMA spectra of SLN alone for the three labeling schemes (**Bottom**) compared to the uniformly-labeled sample (**Top**). The ^{15}N-Leu sample (purple) had 4 peaks as expected (Leu-16, Leu-21, Leu-24, and Leu-25), and the ^{15}N-Ile sample (blue) had three peaks as expected (Ile-14, Ile-17, and Ile-20). The last sample, in which all residues except leucine, isoleucine, and valine are ^{15}N-labeled, also matched well. Thus, the SLN from these purifications was used in studies with SERCA.

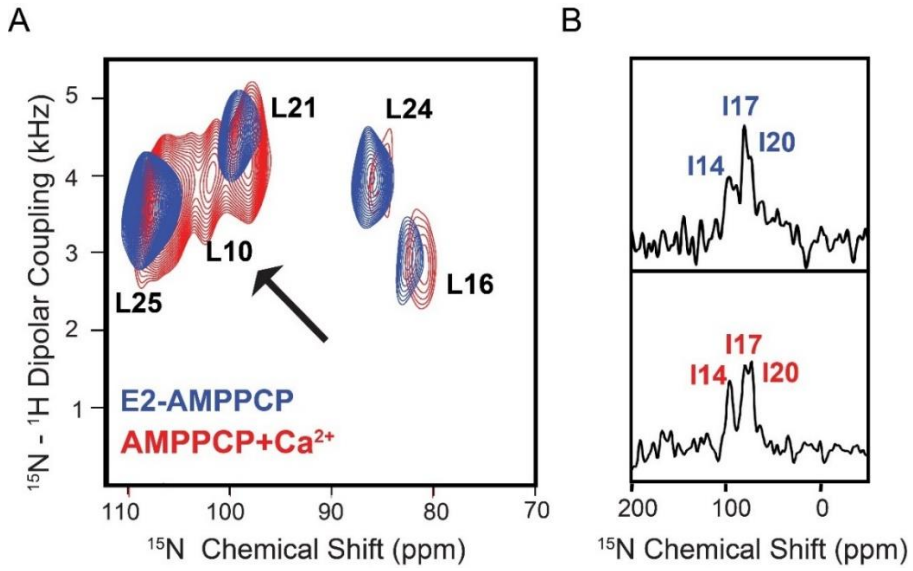

Figure 14. Comparison of selectively-labeled SLN bound to SERCA in the E2- and E1-AMPPCP states. (**A**) Overlaying the ^{15}N-Leu SLN bound to the E2- and E1-AMPPCP states demonstrates that SLN's structure does change. Initially, the sample was prepared as the E2AMPPCP state, but after that spectrum was acquired, 4 mM $CaCl_2$ was added to promote the E1-AMPPCP state. Addition of $CaCl_2$ changed the spectrum, further verifying that SLN is bound to SERCA, and that Ca^{2+} interacted with SERCA. Significantly, a new peak appeared upon addition of Ca^{2+}. Based on a previous assignment[147] and the periodicity of the PISA wheel, this peak is likely Leu-10. (**B**) Comparison of the ^{15}N-Ile SLN bound to the E2- and E1-AMPPCP states also shows slight changes upon the addition of Ca^{2+}.

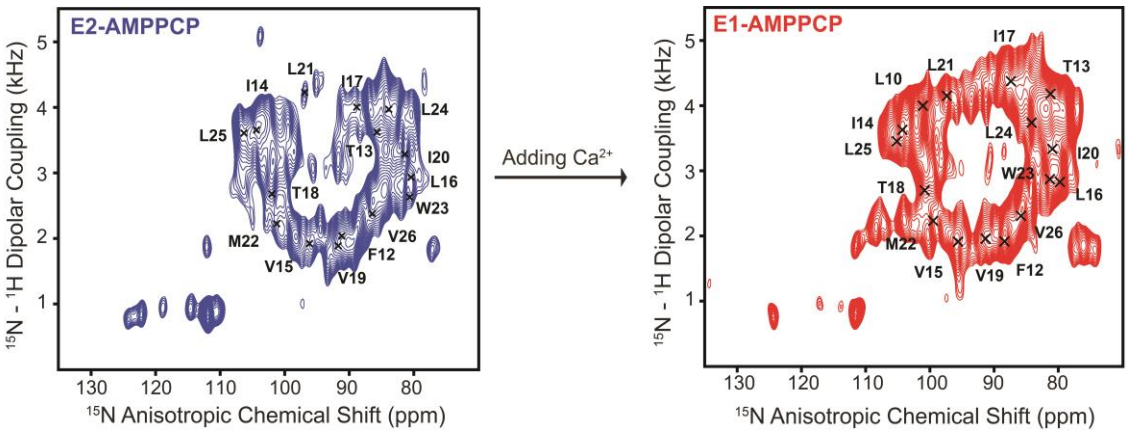

Figure 15. Estimated assignment of uniformly ^{15}N-labeled SLN bound to SERCA in the E2- AMPPCP state and with 4 mM $CaCl_2$ added. Although the overall tilt and rotation angle is similar between the two states, the addition of $CaCl_2$ caused the overall appearance and many peaks to change. Based on the selectively-labeled samples, the N-terminal end of the TM helix is more structured bound to SERCA in the E1-AMPPCP state compared to the E2-AMPPCP state. Changes in the peaks is especially apparent for the terminal residues that are outside of the wheel from ~110 to 125 ppm and 0.8 kHz. Additional labeling schemes could help to identify what residues these peaks correspond to.

Table 1. Estimated chemical shifts and dipolar couplings from the oriented SLN+SERCA samples.

	E1-AMPPCP		**E2-AMPPCP**	
	Chemical Shift (ppm)	Dipolar Coupling (kHz)	Chemical Shift (ppm)	Dipolar Coupling (kHz)
L10	100	4		
N11				
F12	88	2	91	2
T13	81	4.2	86	3.6
I14	104	3.6	105	3.6
V15	96	1.9	96	1.9
L16	80	2.8	81	2.9
I17	87	4.3	89	4
T18	101	2.7	102	2.6
V19	91	1.9	92	1.9
I20	81	3.3	82	3.3
L21	97	4.2	98	4.2
M22	100	2.2	101	2.1
W23	81	2.9	81	2.6
L24	84	3.7	84	3.9
L25	105	3.4	106	3.5
V26	86	2.3	86	2.3
R27				
S28				

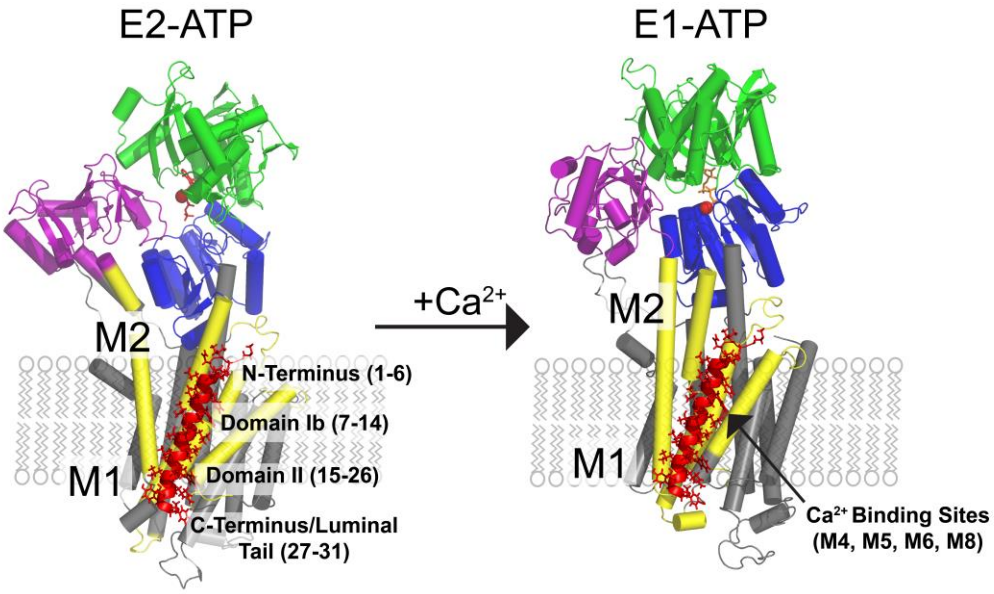

Figure 16. Proposed model in which SLN acts as a wedge inhibiting the movement of SERCA's TM helices. The topologies of M1 and M2 change significantly depending on whether Ca^{2+} is bound, and these changes are propagated to the cytoplasmic domains. SLN (red) binds to the groove formed by M2, M4, M6, and M9 (in yellow), thus it likely interferes with their movements, which may be the explanation for the decrease in SERCA's apparent calcium affinity. Further experiments are needed to better understand the role of SLN's terminal residues. (PDB IDs: 1T5S, 2C8K. Note that SLN's position is merely approximated to illustrate how it could interfere with SERCA.)

Chapter 6 – Conclusions
Biophysical Characterization of Interactions Between Two Membrane Proteins: SERCA and Sarcolipin

6.1 Conclusions

In summary, the work included in this thesis has focused on the biophysical characterization of membrane proteins. Chapter 2 illustrates the use of several biophysical methods including solution-state NMR spectroscopy to characterize the antimicrobial peptide, chionodracine (Cnd).[376] The results demonstrate that Cnd is largely unstructured until it interacts with lipid membranes, at which point it becomes α-helical and forms pores, thereby fragmenting the bacterial membrane and killing the bacteria. The labeling via ethylation of cysteines as described in Chapter 3 can be utilized to study large, functional proteins that cannot be labeled though conventional methods. The utility of this site-directed labeling method was illustrated in studies of SERCA conformational transitions.[377] In Chapter 4, water-edited O-ssNMR experiments were used to examine the residue-specific hydration of SLN within a lipid bilayer system (bicelles).[71] This method may be expanded to other systems to study the hydration of membrane proteins and may even help simplify the spectra for the structural determination of larger proteins. Finally, the OssNMR and preliminary MAS characterization of the SERCA+SLN complex discussed in Chapter 5 indicate that SLN does not appear to dissociate from SERCA when Ca^{2+} binds, but may form a wedge inhibiting conformational changes required for Ca^{2+} transport by SERCA. One of the main challenges in studying the SERCA+SLN complex by ssNMR is that we currently do not have the tools to isotopically label SERCA like we do for SLN. To this end, the methods described in Chapters 3 and 4 could be applied to further investigate the SERCA+SLN complex as well as other peptide regulators of SERCA. For example, the ethyl labeling of SERCA could enable following of changes in SERCA's cytoplasmic domains when SLN is bound compared to when SERCA is free. Given that SLN affects coupling between ATP hydrolysis and Ca^{2+} transport, it seems likely that

structural changes from SLN binding to the TM domain would propagate to the cytoplasmic domains of SERCA resulting in a different signature of the ethyl chemical shifts (preliminary data from a previous student supports this[370]). Moreover, these changes would also probably be different than the peptide regulators of SERCA that do not cause uncoupling. Further development of ssNMR methods will aid greatly in elucidating the molecular mechanism of regulation of SERCA by SLN and other peptides.

Discoveries are still being made about SERCA and its regulation, which is exciting especially as SERCA is one of the most well-studied membrane proteins. Within the last several years, both novel post-translational modifications for SLN and PLN as well as several new regulators of SERCA have been found. SLN from rabbit and pig was found to be both *S*-palmitoylated and *S*-oleoylated at Cys-9, which appears to affect ATP hydrolysis by SERCA.[378] While both rabbit and pig SLN have cysteines at position 9, in humans this residue is replaced by phenylalanine, so human SLN would not be modified in this manner. Modification of PLN by *N*-acetylglucosamine (*O*-GlcNAc) was also recently reported with the site of the modification likely being Ser-16 (it is not yet conclusive that the site of glycosylation is Ser-16 rather than Thr-17)[379] (**Fig. 1A and 1B**). Increased *O*-GlcNAcylation is linked to hyperglycemia, one of the contributing factors to diabetic cardiomyopathy.[380] Given the importance of the SERCA+PLN complex to proper Ca^{2+} homeostasis and ventricular function,[112,248,381-383] it will be crucial to understand how the *O*-GlcNAcylation of PLN contributes to ventricular dysfunction in diabetic cardiomyopathy. The modification of PLN by O-GlcNAc undoubtedly interferes with phosphorylation at both possible phosphorylation sites (PLN can be phosphorylated by PKA at Ser-16 and CaMKII at Thr-17) resulting in glycosylation interfering with the reversal of PLN's inhibition of SERCA. As such, we began to study this system and performed *in vitro* assays to modify

PLN with *O*-GlcNAc for the first time. **Figure 1C** shows the preliminary data indicating that the cytoplasmic domain of PLN is indeed *O*-GlcNAcylated by O-linked β-N-acetylglucosamine transferase (OGT). Although this was only clear for the cytoplasmic domain, that is likely because the cytoplasmic domain is soluble, so no detergents were needed. The wild-type (WT) and monomeric (AFA) versions of PLN require detergent, which can interfere with the activity of the enzymes in the assay as well as the quantification by the assay reagents. In fact, one of the controls indicated that $C_{12}E_8$ decreased the activity of the coupling phosphatase. Thus, more assays are needed to fully understand whether AFA and WT PLN are glycosylated or if detergent interfered with this assay. However, the information gained from studies with O-GlcNAc-PLN would be highly useful as the effects of *O*-GlcNAcylation are generally not well understood at the molecular level:[380,384,385] does *O*-GlcNAcylation merely prevent phosphorylation?[386] By PKA and CaMKII? Or does it have its own effect on PLN's structure and thus SERCA's activity as structural changes have been observed for other proteins?[386] It will be very interesting to carry out further characterization of the *O*-GlcNAc-PLN+SERCA complex as well as the palmitoylation and oleoylation of SLN, which may shed light on how different species have evolved to regulate SERCA's activity according to their own needs.

Also fascinating is the recent discovery of several new regulators of SERCA: myoregulin (MLN),[104] DWORF,[105] the sarcolambans (SCL) in *Drosophila,*[106] endoregulin (ELN) and another-regulin (ALN),[107] as well as small Ankyrin 1.[108] Thus, regulating SERCA through peptides seems to be a conserved mechanism for controlling Ca^{2+} dynamics.[106,107] These studies have already revealed functional differences. MLN, ELN, ALN, and likely the SCLs all inhibit SERCA similar to SLN and PLN,[104,106,107] whereas DWORF counteracts the effects of inhibitory peptides.[105] Furthermore, while most of these peptides are

expressed in either cardiac and/or skeletal muscle,[104,106,107] ALN is also expressed in other tissues including the epidermal epithelium, salivary gland, and brown fat.[107] ELN was expressed almost entirely in non-muscle tissue where it would regulate SERCA3, so perhaps regulation is isoform-specific.[107] Interestingly, these peptides display a high conservation of several amino acids within the transmembrane region, but exhibit greater variability in their terminal regions.[107] It will be curious to see if these different termini have disparate effects on SERCA's activity and/or whether they relate to regulation of the peptide (e.g. through reversal of inhibition via phosphorylation like PLN and SLN). Further characterization of these peptides with SERCA will undoubtedly help elucidate the mechanism of regulation and its variations. In turn, this will aid in the design of new therapeutics to help modulate Ca^{2+} cycling through SERCA in associated diseases such as dilated cardiomyopathy, Brody's disease, and obesity.

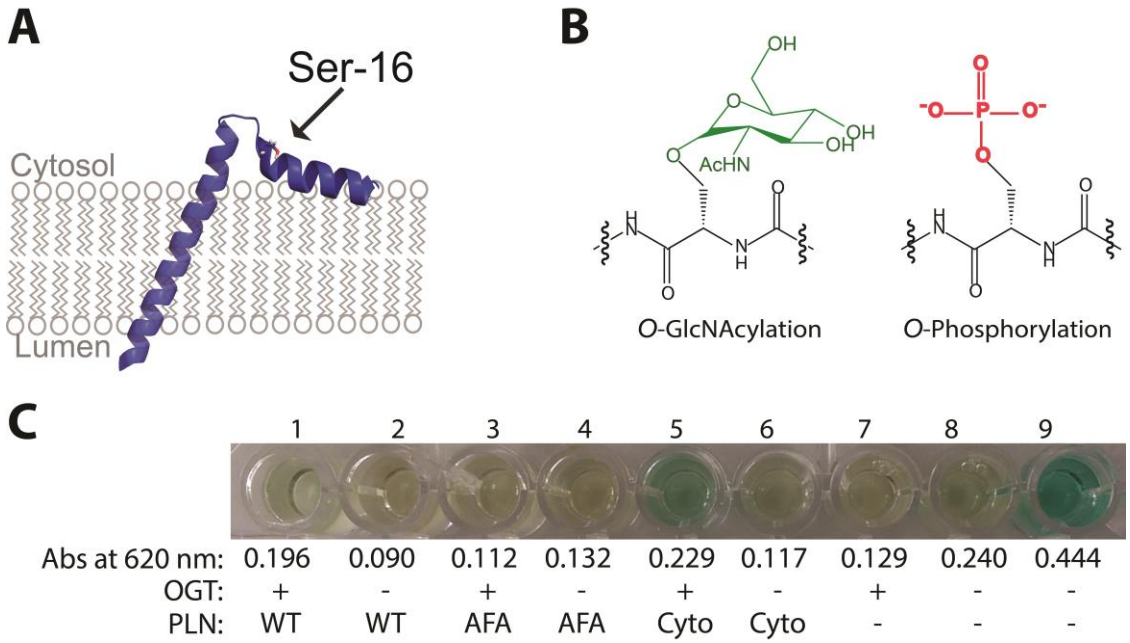

Figure 1. O-GlcNAcylation of PLN by O-linked β-N-acetylglucosamine transferase (OGT). (**A**) NMR structure of PLN (PDB ID:2KB7) with the position of Ser-16 indicated. (**B**) *O*-GlcNAcylation and *O*-phosphorylation of serine. (**C**) Data indicating that the cytoplasmic domain of PLN can be *O*-GlcNAcylated. Assay was performed using a kit from R&D Systems (Catalog #EA001) that measures the activity of glycosyltransferases via a coupled-enzyme assay that quantifies inorganic phosphate via malachite green. Comparing wells 1 and 2 indicated that some WT PLN may have been glycosylated by OGT, whereas glycosylation of AFA is not evident (wells 3 and 4). The cytoplasmic domain of PLN (residues 1-19) showed the clearest evidence of glycosylation (well 5). Wells 7-9 were controls to determine whether the detergent, $C_{12}E_8$, affected the assay. Well 7 included all of the assay components except PLN to ensure the detergent did not introduce a significant background. Wells 8 and 9 compared the effects of $C_{12}E_8$ on the coupled enzyme (coupling phosphatase 1). They contained the phosphatase and its substrate, UDP, but well 8 included $C_{12}E_8$, whereas well 9 was detergent free. The phosphatase was less active in the presence of $C_{12}E_8$.

References

1. Anfinsen, C.B. & Haber, E. Studies on the reduction and re-formation of protein disulfide bonds. *J. Biol. Chem.* **236**, 1361-3 (1961).

2. Hensen, U. et al. Exploring protein dynamics space: the dynasome as the missing link between protein structure and function. *PLoS One.* **7**, e33931 (2012).

3. Kim, J. et al. Dysfunctional conformational dynamics of protein kinase A induced by a lethal mutant of phospholamban hinder phosphorylation. *Proc. Natl. Acad. Sci. U. S. A.* **112**, 3716-21 (2015).

4. Krogh, A., Larsson, B., von Heijne, G. & Sonnhammer, E.L. Predicting transmembrane protein topology with a hidden Markov model: application to complete genomes. *J. Mol. Biol.* **305**, 567-80 (2001).

5. Wallin, E. & von Heijne, G. Genome-wide analysis of integral membrane proteins from eubacterial, archaean, and eukaryotic organisms. *Protein Sci.* **7**, 1029-38 (1998).

6. Stevens, T.J. & Arkin, I.T. Do more complex organisms have a greater proportion of membrane proteins in their genomes? *Proteins.* **39**, 417-20 (2000).

7. Arinaminpathy, Y., Khurana, E., Engelman, D.M. & Gerstein, M.B. Computational analysis of membrane proteins: the largest class of drug targets. *Drug Discov. Today.* **14**, 1130-5 (2009).

8. Singh, S., Malik, B.K. & Sharma, D.K. Molecular drug targets and structure based drug design: A holistic approach. *Bioinformation.* **1**, 314-20 (2006).

9. Bakheet, T.M. & Doig, A.J. Properties and identification of human protein drug targets. *Bioinformatics.* **25**, 451-7 (2009).

10. Bull, S.C. & Doig, A.J. Properties of protein drug target classes. *PLoS One.* **10**, e0117955 (2015).

11. White, S.H. Biophysical dissection of membrane proteins. *Nature.* **459**, 344-6 (2009).

12. von Heijne, G. Membrane-protein topology. *Nat. Rev. Mol. Cell. Biol.* **7**, 909-18 (2006).

13. Hohlweg, W., Kosol, S. & Zangger, K. Determining the orientation and localization of membrane-bound peptides. *Curr. Protein Pept. Sci.* **13**, 267-79 (2012).

14. Lee, S.C. & Pollock, N.L. Membrane proteins: is the future disc shaped? *Biochem. Soc. Trans.* **44**, 1011-8 (2016).

15. White, S.H. The progress of membrane protein structure determination. *Protein Sci.* **13**, 1948-9 (2004).

16. Brown, L.S. & Ladizhansky, V. Membrane proteins in their native habitat as seen by solid-state NMR spectroscopy. *Protein Sci.* **24**, 1333-1346 (2015).

17. Kintzing, J.R., Filsinger Interrante, M.V. & Cochran, J.R. Emerging Strategies for Developing Next-Generation Protein Therapeutics for Cancer Treatment. *Trends Pharmacol. Sci.* **37**, 993-1008 (2016).

18. Jacobs, I. et al. Monoclonal Antibody and Fusion Protein Biosimilars Across Therapeutic Areas: A Systematic Review of Published Evidence. *BioDrugs.* **30**, 489-523 (2016).

19. Fosgerau, K. & Hoffmann, T. Peptide therapeutics: current status and future directions. *Drug Discov. Today.* **20**, 122-128 (2015).

20. Lin, W.J. et al. Epinecidin-1, an antimicrobial peptide from fish (*Epinephelus coioides*) which has an antitumor effect like lytic peptides in human fibrosarcoma cells. *Peptides* **30**, 283-90 (2009).

21. Brogden, K.A. Antimicrobial peptides: pore formers or metabolic inhibitors in bacteria? *Nat. Rev. Microbiol.* **3**, 238-50 (2005).

22. Gobl, C., Kosol, S., Stockner, T., Ruckert, H.M. & Zangger, K. Solution structure and membrane binding of the toxin fst of the par addiction module. *Biochemistry.* **49**, 6567-75 (2010).

23. Grossauer, J., Kosol, S., Schrank, E. & Zangger, K. The peptide hormone ghrelin binds to membrane-mimetics via its octanoyl chain and an adjacent phenylalanine. *Bioorg. Med. Chem.* **18**, 5483-8 (2010).

24. Bechinger, B. & Gorr, S.U. Antimicrobial Peptides: Mechanisms of Action and Resistance. *J. Dent. Res.* (2016).

25. Vaara, M. New approaches in peptide antibiotics. *Curr. Opin. Pharmacol.* **9**, 571-6 (2009).

26. Roscia, G., Falciani, C., Bracci, L. & Pini, A. The development of antimicrobial peptides as new antibacterial drugs. *Curr. Protein Pept. Sci.* **14**, 641-9 (2013).

27. Wimley, W.C. & Hristova, K. Antimicrobial peptides: successes, challenges and unanswered questions. *J. Membr. Biol.* **239**, 27-34 (2011).

28. Singer, S.J. & Nicolson, G.L. The fluid mosaic model of the structure of cell membranes. *Science.* **175**, 720-31 (1972).

29. Engelman, D.M. Membranes are more mosaic than fluid. *Nature.* **438**, 578-580 (2005).

30. Nagle, J.F. & Tristram-Nagle, S. Structure of lipid bilayers. *Biochim. Biophys. Acta.* **1469**, 159-195 (2000).

31. Razi Naqvi, K., Gonzalez-Rodriguez, J., Cherry, R.J. & Chapman, D. Spectroscopic technique for studying protein rotation in membranes. *Nat. New. Biol.* **245**, 249-51 (1973).

32. Edidin, M. Rotational and translational diffusion in membranes. *Annu. Rev. Biophys. Bioeng.* **3**, 179-201 (1974).

33. Zwaal, R.F., Comfurius, P. & van Deenen, L.L. Membrane asymmetry and blood coagulation. *Nature.* **268**, 358-60 (1977).

34. Newton, A.C. Regulation of the ABC kinases by phosphorylation: protein kinase C as a paradigm. *Biochem. J.* **370**, 361-71 (2003).

35. Goni, F.M. The basic structure and dynamics of cell membranes: an update of the Singer-Nicolson model. *Biochim. Biophys. Acta.* **1838**, 1467-76 (2014).

36. Lee, A.G. How lipids affect the activities of integral membrane proteins. *Biochim. Biophys. Acta.* **1666**, 62-87 (2004).

37. Fattal, D.R. & Ben-Shaul, A. A molecular model for lipid-protein interaction in membranes: the role of hydrophobic mismatch. *Biophys. J.* **65**, 1795-1809 (1993).

38. Yeagle, P.L., Bennett, M., Lemaître, V. & Watts, A. Transmembrane helices of membrane proteins may flex to satisfy hydrophobic mismatch. *Biochim. Biophys. Acta.* **1768**, 530-537 (2007).

39. Baldwin, P.A. & Hubbell, W.L. Effects of lipid environment on the light-induced conformational changes of rhodopsin. 2. Roles of lipid chain length, unsaturation, and phase state. *Biochemistry.* **24**, 2633-2639 (1985).

40. Pilot, J.D., East, J.M. & Lee, A.G. Effects of Bilayer Thickness on the Activity of Diacylglycerol Kinase of Escherichia coli. *Biochemistry.* **40**, 8188-8195 (2001).

41. Starling, A.P., East, J.M. & Lee, A.G. Effects of phosphatidylcholine fatty acyl chain length on calcium binding and other functions of the calcium-magnesium-ATPase. *Biochemistry.* **32**, 1593-1600 (1993).

42. Mishig-Ochir, T. et al. Cellular membrane composition requirement by antimicrobial and anticancer peptide GA-K4. *Protein Pept. Lett.* (2016).

43. Dawaliby, R. et al. Allosteric regulation of G protein-coupled receptor activity by phospholipids. *Nat. Chem. Biol.* **12**, 35-9 (2016).

44. Gustavsson, M., Traaseth, N.J. & Veglia, G. Activating and deactivating roles of lipid bilayers on the Ca(2+)-ATPase/phospholamban complex. *Biochemistry.* **50**, 10367-74 (2011).

45. Lu, J.X., Damodaran, K., Blazyk, J. & Lorigan, G.A. Solid-state nuclear magnetic resonance relaxation studies of the interaction mechanism of antimicrobial peptides with phospholipid bilayer membranes. *Biochemistry.* **44**, 10208-17 (2005).

46. Yeagle, P.L. Non-covalent binding of membrane lipids to membrane proteins. *Biochim. Biophys. Acta.* **1838**, 1548-1559 (2014).

47. van Meer, G., Voelker, D.R. & Feigenson, G.W. Membrane lipids: where they are and how they behave. *Nat. Rev. Mol. Cell. Biol.* **9**, 112-124 (2008).

48. Murray, D.T., Das, N. & Cross, T.A. Solid state NMR strategy for characterizing native membrane protein structures. *Acc. Chem. Res.* **46**, 2172-81 (2013).

49. Faham, S. & Bowie, J.U. Bicelle crystallization: a new method for crystallizing membrane proteins yields a monomeric bacteriorhodopsin structure. *J. Mol. Biol.* **316**, 1-6 (2002).

50. Landau, E.M. & Rosenbusch, J.P. Lipidic cubic phases: a novel concept for the crystallization of membrane proteins. *Proc. Natl. Acad. Sci. U. S. A.* **93**, 14532-5 (1996).

51. Wadsten, P. et al. Lipidic sponge phase crystallization of membrane proteins. *J. Mol. Biol.* **364**, 44-53 (2006).

52. Carpenter, E.P., Beis, K., Cameron, A.D. & Iwata, S. Overcoming the challenges of membrane protein crystallography. *Curr. Opin. Struct. Biol.* **18**, 581-586 (2008).

53. Johansson, L.C., Wöhri, A.B., Katona, G., Engström, S. & Neutze, R. Membrane protein crystallization from lipidic phases. *Curr. Opin. Struct. Biol.* **19**, 372-378 (2009).

54. Hansen, S.K., Bertelsen, K., Paaske, B., Nielsen, N.C. & Vosegaard, T. Solid-state NMR methods for oriented membrane proteins. *Prog. Nucl. Magn. Reson. Spectrosc.* **88-89**, 48-85 (2015).

55. Cross, T.A., Ekanayake, V., Paulino, J. & Wright, A. Solid state NMR: The essential technology for helical membrane protein structural characterization. *J. Magn. Reson.* **239**, 100-9 (2014).

56. Arnold, T. & Linke, D. The use of detergents to purify membrane proteins. *Curr. Protoc. Protein Sci.* **Chapter 4**, Unit 4.8.1-4.8.30 (2008).

57. Langelaan, D.N. & Rainey, J.K. Headgroup-dependent membrane catalysis of apelin-receptor interactions is likely. *J. Phys. Chem. B.* **113**, 10465-71 (2009).

58. Bechinger, B., Resende, J.M. & Aisenbrey, C. The structural and topological analysis of membrane-associated polypeptides by oriented solid-state NMR spectroscopy: established concepts and novel developments. *Biophys. Chem.* **153**, 115-25 (2011).

59. Fernandez, C., Hilty, C., Wider, G. & Wuthrich, K. Lipid-protein interactions in DHPC micelles containing the integral membrane protein OmpX investigated by NMR spectroscopy. *Proc. Natl. Acad. Sci. U. S. A.* **99**, 13533-7 (2002).

60. Tjandra, N. & Bax, A. Direct measurement of distances and angles in biomolecules by NMR in a dilute liquid crystalline medium. *Science.* **278**, 1111-4 (1997).

61. Brown, L.R., Bosch, C. & Wuthrich, K. Location and orientation relative to the micelle surface for glucagon in mixed micelles with dodecylphosphocholine: EPR and NMR studies. *Biochim. Biophys. Acta.* **642**, 296-312 (1981).

62. Maltsev, S., Hudson, S.M., Sahu, I.D., Liu, L. & Lorigan, G.A. Solid-State NMR 31P Paramagnetic Relaxation Enhancement Membrane Protein Immersion Depth Measurements. *J. Phys. Chem. B* **118**, 4370-4377 (2014).

63. Dürr, U.H.N., Gildenberg, M. & Ramamoorthy, A. The Magic of Bicelles Lights Up Membrane Protein Structure. *Chem. Rev.* **112**, 6054-6074 (2012).

64. Sanders, C.R., Hare, B.J., Howard, K.P. & Prestegard, J.H. Magnetically-oriented phospholipid micelles as a tool for the study of membrane-associated molecules. *Prog. Nucl. Magn. Reson. Spectrosc.* **26**, 421-444 (1994).

65. Dürr, U.H.N., Soong, R. & Ramamoorthy, A. When detergent meets bilayer: Birth and coming of age of lipid bicelles. *Prog. Nucl. Magn. Reson. Spectrosc.* **69**, 1-22 (2013).

66. Prosser, R.S., Hunt, S.A., DiNatale, J.A. & Vold, R.R. Magnetically Aligned Membrane Model Systems with Positive Order Parameter: Switching the Sign of Szz with Paramagnetic Ions. *J. Am. Chem. Soc.* **118**, 269-270 (1996).

67. Prosser, R.S., Hwang, J.S. & Vold, R.R. Magnetically aligned phospholipid bilayers with positive ordering: a new model membrane system. *Biophys. J.* **74**, 2405-18 (1998).

68. Opella, S.J., Ma, C. & Marassi, F.M. Nuclear Magnetic Resonance of Membrane-Associated Peptides and Proteins. *Methods Enzymol.* **339**, 285-313 (2001).

69. Kaseman, D.C. Chemical Shift and Shielding. *The Chemistry LibreTexts Library.* (2014).

70. Wu, C.H., Ramamoorthy, A. & Opella, S.J. High-Resolution Heteronuclear Dipolar Solid-State NMR Spectroscopy. *J. Magn. Reson.* **109**, 270-272 (1994).

71. Dicke, A., Gopinath, T., Wang, Y. & Veglia, G. Probing Residue-Specific Water-Protein Interactions in Oriented Lipid Membranes via Solid-State NMR Spectroscopy. *J. Phys. Chem. B.* **120**, 10959-10968 (2016).

72. Park, S.H., Mrse, A.A., Nevzorov, A.A., De Angelis, A.A. & Opella, S.J. Rotational diffusion of membrane proteins in aligned phospholipid bilayers by solid-state NMR spectroscopy. *J. Magn. Reson.* **178**, 162-165 (2006).

73. Salnikov, E.S. et al. Alamethicin Topology in Phospholipid Membranes by Oriented Solid-state NMR and EPR Spectroscopies: a Comparison. *J. Phys. Chem. B.* **113**, 3034-3042 (2009).

74. Aisenbrey, C. & Bechinger, B. Tilt and Rotational Pitch Angle of Membrane-Inserted Polypeptides from Combined 15N and 2H Solid-State NMR Spectroscopy. *Biochemistry.* **43**, 10502-10512 (2004).

75. Wang, S. & Ladizhansky, V. Recent advances in magic angle spinning solid state NMR of membrane proteins. *Prog. Nucl. Magn. Reson. Spectrosc.* **82**, 1-26 (2014).

76. Roberts, M.F. & Redfield, A.G. Phospholipid bilayer surface configuration probed quantitatively by (31)P field-cycling NMR. *Proc. Natl. Acad. Sci. U. S. A.* **101**, 17066-71 (2004).

77. McDermott, A. Structure and dynamics of membrane proteins by magic angle spinning solid-state NMR. *Annu. Rev. Biophys.* **38**, 385-403 (2009).

78. Hong, M., Zhang, Y. & Hu, F. Membrane protein structure and dynamics from NMR spectroscopy. *Annu. Rev. Phys. Chem.* **63**, 1-24 (2012).

79. Mahlapuu, M., Hakansson, J., Ringstad, L. & Bjorn, C. Antimicrobial Peptides: An Emerging Category of Therapeutic Agents. *Front. Cell. Infect. Microbiol.* **6**, 194 (2016).

80. Fjell, C.D., Hiss, J.A., Hancock, R.E. & Schneider, G. Designing antimicrobial peptides: form follows function. *Nat. Rev. Drug Discov.* **11**, 37-51 (2011).

81. Hancock, R.E. & Sahl, H.G. Antimicrobial and host-defense peptides as new anti-infective therapeutic strategies. *Nat. Biotechnol.* **24**, 1551-7 (2006).

82. Hancock, R.E.W. Peptide antibiotics. *The Lancet.* **349**, 418-422 (1997).

83. Takahashi, D., Shukla, S.K., Prakash, O. & Zhang, G. Structural determinants of host defense peptides for antimicrobial activity and target cell selectivity. *Biochimie.* **92**, 1236-41 (2010).

84. Nguyen, L.T., Haney, E.F. & Vogel, H.J. The expanding scope of antimicrobial peptide structures and their modes of action. *Trends Biotechnol.* **29**, 464-72 (2011).

85. Pasupuleti, M., Schmidtchen, A. & Malmsten, M. Antimicrobial peptides: key components of the innate immune system. *Crit. Rev. Biotechnol.* **32**, 143-71 (2012).

86. Yeaman, M.R. & Yount, N.Y. Mechanisms of antimicrobial peptide action and resistance. *Pharmacol. Rev.* **55**, 27-55 (2003).

87. Perrin, B.S., Jr. et al. High-resolution structures and orientations of antimicrobial peptides piscidin 1 and piscidin 3 in fluid bilayers reveal tilting, kinking, and bilayer immersion. *J. Am. Chem. Soc.* **136**, 3491-504 (2014).

88. De Angelis, A.A. et al. Amphipathic antimicrobial piscidin in magnetically aligned lipid bilayers. *Biophys. J.* **101**, 1086-94 (2011).

89. Chekmenev, E.Y. et al. High-Field NMR Studies of Molecular Recognition and Structure−Function Relationships in Antimicrobial Piscidins at the Water−Lipid Bilayer Interface. *J. Am. Chem. Soc.* **128**, 5308-5309 (2006).

90. Fu, R., Gordon, E.D., Hibbard, D.J. & Cotten, M. High resolution heteronuclear correlation NMR spectroscopy of an antimicrobial peptide in aligned lipid bilayers: peptide-water interactions at the water-bilayer interface. *J. Am. Chem. Soc.* **131**, 10830-1 (2009).

91. Zhang, L., Rozek, A. & Hancock, R.E.W. Interaction of Cationic Antimicrobial Peptides with Model Membranes. *J. Biol. Chem.* **276**, 35714-35722 (2001).

92. Buonocore, F. et al. A piscidin-like antimicrobial peptide from the icefish *Chionodraco hamatus* (Perciformes: Channichthyidae): molecular characterization, localization and bactericidal activity. *Fish Shellfish Immunol.* **33**, 1183-91 (2012).

93. Gehlert, S., Bloch, W. & Suhr, F. Ca(2+)-Dependent Regulations and Signaling in Skeletal Muscle: From Electro-Mechanical Coupling to Adaptation. *Int. J. Mol. Sci.* **16**, 1066-1095 (2015).

94. Cui, C., Merritt, R., Fu, L. & Pan, Z. Targeting calcium signaling in cancer therapy. *Acta Pharm. Sin. B.* **7**, 3-17 (2017).

95. Berridge, M.J., Lipp, P. & Bootman, M.D. The versatility and universality of calcium signalling. *Nat. Rev. Mol. Cell. Biol.* **1**, 11-21 (2000).

96. Bombardier, E., Smith, I.C., Vigna, C., Fajardo, V.A. & Tupling, A.R. Ablation of sarcolipin decreases the energy requirements for Ca2+ transport by sarco(endo)plasmic reticulum Ca2+-ATPases in resting skeletal muscle. *FEBS Lett.* **587**, 1687-92 (2013).

97. Babu, G.J. et al. Targeted overexpression of sarcolipin in the mouse heart decreases sarcoplasmic reticulum calcium transport and cardiac contractility. *J. Biol. Chem.* **281**, 3972-9 (2006).

98. Hovnanian, A. SERCA pumps and human diseases. *Subcell. Biochem.* **45**, 337-63 (2007).

99. Brandl, C.J., Green, N.M., Korczak, B. & MacLennan, D.H. Two Ca2+ ATPase genes: homologies and mechanistic implications of deduced amino acid sequences. *Cell.* **44**, 597-607 (1986).

100. Brandl, C.J., deLeon, S., Martin, D.R. & MacLennan, D.H. Adult forms of the Ca2+ATPase of sarcoplasmic reticulum. Expression in developing skeletal muscle. *J. Biol. Chem.* **262**, 3768-74 (1987).

101. MacLennan, D.H., Brandl, C.J., Korczak, B. & Green, N.M. Amino-acid sequence of a Ca2+ + Mg2+-dependent ATPase from rabbit muscle sarcoplasmic reticulum, deduced from its complementary DNA sequence. *Nature.* **316**, 696-700 (1985).

102. Zarain-Herzberg, A., MacLennan, D.H. & Periasamy, M. Characterization of rabbit cardiac sarco(endo)plasmic reticulum Ca2(+)-ATPase gene. *J. Biol. Chem.* **265**, 4670-7 (1990).

103. Bassani, J.W., Bassani, R.A. & Bers, D.M. Relaxation in rabbit and rat cardiac cells: species-dependent differences in cellular mechanisms. *J. Physiol.* **476**, 279-93 (1994).

104. Anderson, D.M. et al. A micropeptide encoded by a putative long noncoding RNA regulates muscle performance. *Cell.* **160**, 595-606 (2015).

105. Nelson, B.R. et al. A peptide encoded by a transcript annotated as long noncoding RNA enhances SERCA activity in muscle. *Science.* **351**, 271-5 (2016).

106. Magny, E.G. et al. Conserved regulation of cardiac calcium uptake by peptides encoded in small open reading frames. *Science.* **341**, 1116-20 (2013).

107. Anderson, D.M. et al. Widespread control of calcium signaling by a family of SERCA-inhibiting micropeptides. *Sci. Signal.* **9**, ra119 (2016).

108. Desmond, P.F., Muriel, J., Markwardt, M.L., Rizzo, M.A. & Bloch, R.J. Identification of Small Ankyrin 1 as a Novel Sarco(endo)plasmic Reticulum Ca2+-ATPase 1 (SERCA1) Regulatory Protein in Skeletal Muscle. *J. Biol. Chem.* (2015).

109. Babu, G.J., Bhupathy, P., Carnes, C.A., Billman, G.E. & Periasamy, M. Differential expression of sarcolipin protein during muscle development and cardiac pathophysiology. *J. Mol. Cell. Cardiol.* **43**, 215-22 (2007).

110. Nef, H.M. et al. Abnormalities in intracellular Ca2+ regulation contribute to the pathomechanism of Tako-Tsubo cardiomyopathy. *Eur. Heart J.* **30**, 2155-64 (2009).

111. Schneider, J.S. et al. Increased sarcolipin expression and decreased sarco(endo)plasmic reticulum Ca2+ uptake in skeletal muscles of mouse models of Duchenne muscular dystrophy. *J. Muscle. Res. Cell. Motil.* **34**, 349-56 (2013).

112. Kranias, E.G. & Bers, D.M. Calcium and cardiomyopathies. *Subcell. Biochem.* **45**, 523-37 (2007).

113. MacLennan, D.H. & Kranias, E.G. Phospholamban: a crucial regulator of cardiac contractility. *Nat. Rev. Mol. Cell. Biol.* **4**, 566-77 (2003).

114. Schmitt, J.P. et al. Dilated cardiomyopathy and heart failure caused by a mutation in phospholamban. *Science.* **299**, 1410-3 (2003).

115. Wawrzynow, A. et al. Sarcolipin, the "proteolipid" of skeletal muscle sarcoplasmic reticulum, is a unique, amphipathic, 31-residue peptide. *Arch. Biochem. Biophys.* **298**, 620-3 (1992).

116. Odermatt, A. et al. Characterization of the gene encoding human sarcolipin (SLN), a proteolipid associated with SERCA1: absence of structural mutations in five patients with Brody disease. *Genomics.* **45**, 541-53 (1997).

117. Gayan-Ramirez, G., Vanzeir, L., Wuytack, F. & Decramer, M. Corticosteroids decrease mRNA levels of SERCA pumps, whereas they increase sarcolipin mRNA in the rat diaphragm. *J. Physiol.* **524 Pt 2**, 387-97 (2000).

118. Minamisawa, S. et al. Atrial chamber-specific expression of sarcolipin is regulated during development and hypertrophic remodeling. *J. Biol. Chem.* **278**, 9570-5 (2003).

119. Odermatt, A. et al. Sarcolipin regulates the activity of SERCA1, the fast-twitch skeletal muscle sarcoplasmic reticulum Ca2+-ATPase. *J. Biol. Chem.* **273**, 12360-9 (1998).

120. Gorski, P.A., Glaves, J.P., Vangheluwe, P. & Young, H.S. Sarco(endo)plasmic reticulum calcium ATPase (SERCA) inhibition by sarcolipin is encoded in its luminal tail. *J. Biol. Chem.* **288**, 8456-67 (2013).

121. Mall, S. et al. The presence of sarcolipin results in increased heat production by Ca2+-ATPase. *J. Biol. Chem.* **281**, 36597-36602 (2006).

122. Smith, W.S., Broadbridge, R., East, J.M. & Lee, A.G. Sarcolipin uncouples hydrolysis of ATP from accumulation of Ca2+ by the Ca2+-ATPase of skeletal-muscle sarcoplasmic reticulum. *Biochem. J.* **361**, 277-286 (2002).

123. Sahoo, S.K., Shaikh, S.A., Sopariwala, D.H., Bal, N.C. & Periasamy, M. Sarcolipin Protein Interaction with Sarco(endo) plasmic Reticulum Ca2+ ATPase (SERCA) Is Distinct from Phospholamban Protein, and Only Sarcolipin Can Promote Uncoupling of the SERCA Pump. *J. Biol. Chem.* **288**, 6881-6889 (2013).

124. Bhupathy, P., Babu, G.J., Ito, M. & Periasamy, M. Threonine-5 at the N-terminus can modulate sarcolipin function in cardiac myocytes. *J. Mol. Cell. Cardiol.* **47**, 723-9 (2009).

125. Babu, G.J. et al. Ablation of sarcolipin enhances sarcoplasmic reticulum calcium transport and atrial contractility. *Proc. Natl. Acad. Sci. U. S. A.* **104**, 17867-72 (2007).

126. Shanmugam, M. et al. Cardiac specific expression of threonine 5 to alanine mutant sarcolipin results in structural remodeling and diastolic dysfunction. *PLoS One.* **10**, e0115822 (2015).

127. Bal, N.C. et al. Sarcolipin is a newly identified regulator of muscle-based thermogenesis in mammals. *Nat. Med.* **18**, 1575-9 (2012).

128. von Heijne, G. Recent advances in the understanding of membrane protein assembly and structure. *Q. Rev. Biophys.* **32**, 285-307 (1999).

129. Ulmschneider, M.B., Sansom, M.S. & Di Nola, A. Properties of integral membrane protein structures: derivation of an implicit membrane potential. *Proteins.* **59**, 252-65 (2005).

130. Park, S.H. & Opella, S.J. Tilt angle of a trans-membrane helix is determined by hydrophobic mismatch. *J. Mol. Biol.* **350**, 310-8 (2005).

131. Ulmschneider, M.B. & Sansom, M.S.P. Amino acid distributions in integral membrane protein structures. *Biochim. Biophys. Acta.* **1512**, 1-14 (2001).

132. Meruelo, A.D., Samish, I. & Bowie, J.U. TMKink: A method to predict transmembrane helix kinks. *Protein Sci.* **20**, 1256-1264 (2011).

133. Hall, S.E., Roberts, K. & Vaidehi, N. Position of helical kinks in membrane protein crystal structures and the accuracy of computational prediction. *J. Mol. Graph. Model.* **27**, 944-950 (2009).

134. Deupi, X. et al. Ser and Thr Residues Modulate the Conformation of Pro-Kinked Transmembrane α-Helices. *Biophys. J.* **86**, 105-115 (2004).

135. Shelar, A. & Bansal, M. Helix perturbations in membrane proteins assist in inter-helical interactions and optimal helix positioning in the bilayer. *Biochim. Biophys. Acta.* **1858**, 2804-2817 (2016).

136. Heijne, G. The distribution of positively charged residues in bacterial inner membrane proteins correlates with the trans-membrane topology. *EMBO J.* **5**, 3021-7 (1986).

137. Nilsson, J., Persson, B. & von Heijne, G. Comparative analysis of amino acid distributions in integral membrane proteins from 107 genomes. *Proteins.* **60**, 606-16 (2005).

138. Crick, F.H.C. The packing of α-helices: simple coiled-coils. *Acta Cryst.* **6**, 689-697 (1953).

139. McLachlan, A.D. & Stewart, M. Tropomyosin coiled-coil interactions: evidence for an unstaggered structure. *J. Mol. Biol.* **98**, 293-304 (1975).

140. O'Shea, E.K., Klemm, J.D., Kim, P.S. & Alber, T. X-ray structure of the GCN4 leucine zipper, a two-stranded, parallel coiled coil. *Science.* **254**, 539-44 (1991).

141. Mascioni, A., Karim, C., Barany, G., Thomas, D.D. & Veglia, G. Structure and orientation of sarcolipin in lipid environments. *Biochemistry.* **41**, 475-82 (2002).

142. Buffy, J.J. et al. Defining the intramembrane binding mechanism of sarcolipin to calcium ATPase using solution NMR spectroscopy. *J. Mol. Biol.* **358**, 420-9 (2006).

143. Buffy, J.J. et al. Two-dimensional solid-state NMR reveals two topologies of sarcolipin in oriented lipid bilayers. *Biochemistry.* **45**, 10939-46 (2006).

144. Mote, K.R. et al. Multidimensional oriented solid-state NMR experiments enable the sequential assignment of uniformly 15N labeled integral membrane proteins in magnetically aligned lipid bilayers. *J. Biomol. NMR.* **51**, 339-46 (2011).

145. Mote, K.R., Gopinath, T. & Veglia, G. Determination of structural topology of a membrane protein in lipid bilayers using polarization optimized experiments (POE) for static and MAS solid state NMR spectroscopy. *J. Biomol. NMR.* **57**, 91-102 (2013).

146. Gopinath, T., Mote, K.R. & Veglia, G. Sensitivity and resolution enhancement of oriented solid-state NMR: application to membrane proteins. *Prog. Nucl. Magn. Reson. Spectrosc.* **75**, 50-68 (2013).

147. Gopinath, T., Mote, K.R. & Veglia, G. Simultaneous acquisition of 2D and 3D solid-state NMR experiments for sequential assignment of oriented membrane protein samples. *J. Biomol. NMR.* **62**, 53-61 (2015).

148. Gopinath, T., Traaseth, N.J., Mote, K. & Veglia, G. Sensitivity enhanced heteronuclear correlation spectroscopy in multidimensional solid-state NMR of oriented systems via chemical shift coherences. *J. Am. Chem. Soc.* **132**, 5357-63 (2010).

149. Gopinath, T., Verardi, R., Traaseth, N.J. & Veglia, G. Sensitivity enhancement of separated local field experiments: application to membrane proteins. *J. Phys. Chem. B.* **114**, 5089-95 (2010).

150. Moller, J., Oleson, C., Winther, A. & Nissen, P. The sarcoplasmic Ca^{2+}-ATPase: design of a perfect chemi-osmotic pump. *Q. Rev. Biophys.* **43**, 501-566 (2010).

151. Cornelius, F. & Moller, J.V. Electrogenic pump current of sarcoplasmic reticulum Ca(2+)-ATPase reconstituted at high lipid/protein ratio. *FEBS Lett.* **284**, 46-50 (1991).

152. Levy, D., Seigneuret, M., Bluzat, A. & Rigaud, J.L. Evidence for proton countertransport by the sarcoplasmic reticulum Ca2(+)-ATPase during calcium transport in reconstituted proteoliposomes with low ionic permeability. *J. Biol. Chem.* **265**, 19524-34 (1990).

153. Yu, X., Carroll, S., Rigaud, J.L. & Inesi, G. H+ countertransport and electrogenicity of the sarcoplasmic reticulum Ca2+ pump in reconstituted proteoliposomes. *Biophys. J.* **64**, 1232-42 (1993).

154. Hasselbach, W. Relaxing factor and the relaxation of muscle. *Prog. Biophys. Mol. Biol.* **14**, 167-222 (1964).

155. Martonosi, A. & Feretos, R. Sarcoplasmic Reticulum: II. Correlation between adenosine triphosphatase activity and Ca++ uptake *J. Biol. Chem.* **239**, 659-668 (1964).

156. Inesi, G., Kurzmack, M. & Verjovski-Almeida, S. ATPase phosphorylation and calcium ion translocation in the transient state of sarcoplasmic reticulum activity. *Ann. N. Y. Acad. Sci.* **307**, 224-7 (1978).

157. Yu, X. & Inesi, G. Variable stoichiometric efficiency of Ca2+ and Sr2+ transport by the sarcoplasmic reticulum ATPase. *J. Biol. Chem.* **270**, 4361-7 (1995).

158. Toyoshima, C. et al. Crystal structures of the calcium pump and sarcolipin in the Mg2+-bound E1 state. *Nature.* **495**, 260-4 (2013).

159. Winther, A.M. et al. The sarcolipin-bound calcium pump stabilizes calcium sites exposed to the cytoplasm. *Nature.* **495**, 265-9 (2013).

160. Asahi, M. et al. Sarcolipin regulates sarco(endo)plasmic reticulum Ca2+-ATPase (SERCA) by binding to transmembrane helices alone or in association with phospholamban. *Proc. Natl. Acad. Sci. U. S. A.* **100**, 5040-5 (2003).

161. Toyoshima, C. & Cornelius, F. New crystal structures of PII-type ATPases: excitement continues. *Curr. Opin. Struct. Biol.* **23**, 507-14 (2013).

162. Gramolini, A.O. et al. Sarcolipin retention in the endoplasmic reticulum depends on its C-terminal RSYQY sequence and its interaction with sarco(endo)plasmic Ca(2+)-ATPases. *Proc. Natl. Acad. Sci. U. S. A.* **101**, 16807-12 (2004).

163. Hughes, E., Clayton, J.C., Kitmitto, A., Esmann, M. & Middleton, D.A. Solid-state NMR and functional measurements indicate that the conserved tyrosine residues of sarcolipin are involved directly in the inhibition of SERCA1. *J. Biol. Chem.* **282**, 26603-13 (2007).

164. Sahoo, S.K. et al. The N Terminus of Sarcolipin Plays an Important Role in Uncoupling Sarco-endoplasmic Reticulum Ca2+-ATPase (SERCA) ATP Hydrolysis from Ca2+ Transport. *J. Biol. Chem.* **290**, 14057-67 (2015).

165. Autry, J.M., Thomas, D.D. & Espinoza-Fonseca, L.M. Sarcolipin Promotes Uncoupling of the SERCA Ca2+ Pump by Inducing a Structural Rearrangement in the Energy-Transduction Domain. *Biochemistry.* **55**, 6083-6086 (2016).

166. Garnett, C., Sumbilla, C., Belda, F.F., Chen, L. & Inesi, G. Energy transduction and kinetic regulation by the peptide segment connecting phosphorylation and cation binding domains in transport ATPases. *Biochemistry.* **35**, 11019-25 (1996).

167. Zhang, Z. et al. Detailed characterization of the cooperative mechanism of Ca(2+) binding and catalytic activation in the Ca(2+) transport (SERCA) ATPase. *Biochemistry.* **39**, 8758-67 (2000).

168. Zhang, Z., Sumbilla, C., Lewis, D. & Inesi, G. High sensitivity to site directed mutagenesis of the peptide segment connecting phosphorylation and Ca2+ binding domains in the Ca2+ transport ATPase. *FEBS Lett.* **335**, 261-4 (1993).

169. Andersen, J.P. Functional consequences of alterations to amino acids at the M5S5 boundary of the Ca(2+)-ATPase of sarcoplasmic reticulum. Mutation Tyr763-->Gly uncouples ATP hydrolysis from Ca2+ transport. *J. Biol. Chem.* **270**, 908-14 (1995).

170. Daiho, T. et al. Mutations of either or both Cys876 and Cys888 residues of sarcoplasmic reticulum Ca2+-ATPase result in a complete loss of Ca2+ transport activity without a loss of Ca2+-dependent ATPase activity. Role of the CYS876-CYS888 disulfide bond. *J. Biol. Chem.* **276**, 32771-8 (2001).

171. Lomize, M.A., Lomize, A.L., Pogozheva, I.D. & Mosberg, H.I. OPM: Orientations of Proteins in Membranes database. *Bioinformatics* **22**, 623-625 (2006).

172. Boman, H.G. Antibacterial peptides: basic facts and emerging concepts. *J. Intern. Med.* **254**, 197-215 (2003).

173. Porcelli, F., Ramamoorthy, A., Barany, G. & Veglia, G. On the role of NMR spectroscopy for characterization of antimicrobial peptides. *Methods Mol. Biol.* **1063**, 159-80 (2013).

174. Izadpanah, A. & Gallo, R.L. Antimicrobial peptides. *J. Am. Acad. Dermatol.* **52**, 381-90 (2005).

175. Campagna, S., Saint, N., Molle, G. & Aumelas, A. Structure and mechanism of action of the antimicrobial peptide piscidin. *Biochemistry.* **46**, 1771-8 (2007).

176. Masso-Silva, J.A. & Diamond, G. Antimicrobial peptides from fish. *Pharmaceuticals (Basel).* **7**, 265-310 (2014).

177. Sung, W.S., Lee, J. & Lee, D.G. Fungicidal effect and the mode of action of piscidin 2 derived from hybrid striped bass. *Biochem. Biophys. Res. Commun.* **371**, 551-5 (2008).

178. Noga, E.J. & Silphaduang, U. Piscidins: a novel family of peptide antibiotics from fish. *Drug News Perspect.* **16**, 87-92 (2003).

179. Bechinger, B., Macdonald, P.M. & Seelig, J. Deuterium NMR studies of the interactions of polyhydroxyl compounds and of glycolipids with lipid model membranes. *Biochim. Biophys. Acta.* **943**, 381-5 (1988).

180. Hsu, J.C., Lin, L.C., Tzen, J.T. & Chen, J.Y. Characteristics of the antitumor activities in tumor cells and modulation of the inflammatory response in RAW264.7 cells of a novel antimicrobial peptide, chrysophsin-1, from the red sea bream (*Chrysophrys major*). *Peptides.* **32**, 900-10 (2011).

181. Hilchie, A.L. et al. Pleurocidin-family cationic antimicrobial peptides are cytolytic for breast carcinoma cells and prevent growth of tumor xenografts. *Breast Cancer Res.* **13**, R102 (2011).

182. Hancock, R.E. & Sahl, H.G. New strategies and compounds for anti-infective treatment. *Curr. Opin. Microbiol.* **16**, 519-21 (2013).

183. Nicholls, E.F., Madera, L. & Hancock, R.E. Immunomodulators as adjuvants for vaccines and antimicrobial therapy. *Ann. N. Y. Acad. Sci.* **1213**, 46-61 (2010).

184. Pujol, C., Eugene, E., de Saint Martin, L. & Nassif, X. Interaction of *Neisseria meningitidis* with a polarized monolayer of epithelial cells. *Infect. Immun.* **65**, 4836-42 (1997).

185. Ladokhin, A.S., Jayasinghe, S. & White, S.H. How to measure and analyze tryptophan fluorescence in membranes properly, and why bother? *Anal. Biochem.* **285**, 235-45 (2000).

186. Wimley, W.C. & White, S.H. Membrane partitioning: distinguishing bilayer effects from the hydrophobic effect. *Biochemistry.* **32**, 6307-12 (1993).

187. Fernandez-Vidal, M., White, S.H. & Ladokhin, A.S. Membrane partitioning: "classical" and "nonclassical" hydrophobic effects. *J. Membr. Biol.* **239**, 5-14 (2011).

188. Rathinakumar, R. & Wimley, W.C. Biomolecular engineering by combinatorial design and high-throughput screening: small, soluble peptides that permeabilize membranes. *J. Am. Chem. Soc.* **130**, 9849-58 (2008).

189. Ladokhin, A.S. Fluorescence spectroscopy in thermodynamic and kinetic analysis of pH-dependent membrane protein insertion. *Methods Enzymol.* **466**, 19-42 (2009).

190. White, S.H., Wimley, W.C., Ladokhin, A.S. & Hristova, K. Protein folding in membranes: determining energetics of peptide-bilayer interactions. *Methods Enzymol.* **295**, 62-87 (1998).

191. Domadia, P.N., Bhunia, A., Ramamoorthy, A. & Bhattacharjya, S. Structure, interactions, and antibacterial activities of MSI-594 derived mutant peptide MSI-594F5A in lipopolysaccharide micelles: role of the helical hairpin conformation in outer-membrane permeabilization. *J. Am. Chem. Soc.* **132**, 18417-28 (2010).

192. Garg, P., Nemec, K.N., Khaled, A.R. & Tatulian, S.A. Transmembrane pore formation by the carboxyl terminus of Bax protein. *Biochim. Biophys. Acta.* **1828**, 732-42 (2013).

193. Park, N.G. et al. Structure-activity relationships of piscidin 4, a piscine antimicrobial peptide. *Biochemistry.* **50**, 3288-99 (2011).

194. Lakowicz, J.R. *Principles of Fluorescence Spectroscopy*, (Springer Science+Business Media, LLC, 2006).

195. Bax, A. & Davis, D.G. MLEV-17-based two-dimensional homonuclear magnetization transfer spectroscopy. *J. of Mag. Reson. (1969).* **65**, 355-360 (1985).

196. Kumar, A., Ernst, R.R. & Wuthrich, K. A two-dimensional nuclear Overhauser enhancement (2D NOE) experiment for the elucidation of complete proton-proton cross-relaxation networks in biological macromolecules. *Biochem. Biophys. Res. Commun.* **95**, 1-6 (1980).

197. Piotto, M., Saudek, V. & Sklenar, V. Gradient-tailored excitation for single-quantum NMR spectroscopy of aqueous solutions. *J. Biomol. NMR.* **2**, 661-5 (1992).

198. Shaka, A.J., Lee, C.J. & Pines, A. Iterative schemes for bilinear operators; application to spin decoupling. *J. Magn. Reson. (1969).* **77**, 274-293 (1988).

199. Delaglio, F. et al. NMRPipe: A multidimensional spectral processing system based on UNIX pipes. *J. Biomol. NMR.* **6**, 277-93 (1995).

200. Goddard, T.D. & Kneller, D.G. SPARKY 3. (University of California, San Francisco).

201. Wüthrich, K. *NMR of Proteins and Nucleic Acids*, (Wiley, 1986).

202. Shen, Y., Delaglio, F., Cornilescu, G. & Bax, A. TALOS+: a hybrid method for predicting protein backbone torsion angles from NMR chemical shifts. *J. Biomol. NMR.* **44**, 213-23 (2009).

203. Schwieters, C.D., Kuszewski, J.J. & Marius Clore, G. Using Xplor–NIH for NMR molecular structure determination. *Prog. Nucl. Magn. Reson. Spectrosc.* **48**, 47-62 (2006).

204. Davis, I.W. et al. MolProbity: all-atom contacts and structure validation for proteins and nucleic acids. *Nucleic Acids Res.* **35**, W375-83 (2007).

205. Frias, A., Manresa, A., de Oliveira, E., Lopez-Iglesias, C. & Mercade, E. Membrane vesicles: a common feature in the extracellular matter of cold-adapted antarctic bacteria. *Microb. Ecol.* **59**, 476-86 (2010).

206. Andrushchenko, V.V., Aarabi, M.H., Nguyen, L.T., Prenner, E.J. & Vogel, H.J. Thermodynamics of the interactions of tryptophan-rich cathelicidin antimicrobial peptides with model and natural membranes. *Biochim. Biophys. Acta.* **1778**, 1004-14 (2008).

207. Porcelli, F. et al. Structure and orientation of pardaxin determined by NMR experiments in model membranes. *J. Biol. Chem.* **279**, 45815-23 (2004).

208. Porcelli, F., Buck-Koehntop, B.A., Thennarasu, S., Ramamoorthy, A. & Veglia, G. Structures of the dimeric and monomeric variants of magainin antimicrobial peptides (MSI-78 and MSI-594) in micelles and bilayers, determined by NMR spectroscopy. *Biochemistry.* **45**, 5793-9 (2006).

209. Porcelli, F. et al. NMR structure of the cathelicidin-derived human antimicrobial peptide LL-37 in dodecylphosphocholine micelles. *Biochemistry.* **47**, 5565-72 (2008).

210. Mascioni, A., Porcelli, F., Ilangovan, U., Ramamoorthy, A. & Veglia, G. Conformational preferences of the amylin nucleation site in SDS micelles: an NMR study. *Biopolymers.* **69**, 29-41 (2003).

211. Wishart, D.S., Sykes, B.D. & Richards, F.M. The chemical shift index: a fast and simple method for the assignment of protein secondary structure through NMR spectroscopy. *Biochemistry.* **31**, 1647-51 (1992).

212. Berjanskii, M.V. & Wishart, D.S. Application of the random coil index to studying protein flexibility. *J. Biomol. NMR.* **40**, 31-48 (2008).

213. Powers, J.P. & Hancock, R.E. The relationship between peptide structure and antibacterial activity. *Peptides.* **24**, 1681-91 (2003).

214. Jamasbi, E. et al. Melittin peptides exhibit different activity on different cells and model membranes. *Amino Acids.* **46**, 2759-66 (2014).

215. Fernandez, D.I. et al. The antimicrobial peptide aurein 1.2 disrupts model membranes via the carpet mechanism. *Phys. Chem. Chem. Phys.* **14**, 15739-51 (2012).

216. Lai, Y. & Gallo, R.L. AMPed up immunity: how antimicrobial peptides have multiple roles in immune defense. *Trends Immunol.* **30**, 131-41 (2009).

217. Hilchie, A.L., Wuerth, K. & Hancock, R.E. Immune modulation by multifaceted cationic host defense (antimicrobial) peptides. *Nat. Chem. Biol.* **9**, 761-8 (2013).

218. Bechinger, B. & Salnikov, E.S. The membrane interactions of antimicrobial peptides revealed by solid-state NMR spectroscopy. *Chem. Phys. Lipids.* **165**, 282-301 (2012).

219. Verly, R.M. et al. Structure and membrane interactions of the antibiotic peptide dermadistinctin K by multidimensional solution and oriented ^{15}N and ^{31}P solid-state NMR spectroscopy. *Biophys J* **96**, 2194-203 (2009).

220. Wang, G., Li, X. & Wang, Z. APD2: the updated antimicrobial peptide database and its application in peptide design. *Nucleic Acids Res.* **37**, D933-7 (2009).

221. Verardi, R. et al. Probing membrane topology of the antimicrobial peptide distinctin by solid-state NMR spectroscopy in zwitterionic and charged lipid bilayers. *Biochim. Biophys. Acta.* **1808**, 34-40 (2011).

222. Henriques, S.T. & Craik, D.J. Importance of the cell membrane on the mechanism of action of cyclotides. *ACS Chem. Biol.* **7**, 626-36 (2012).

223. Primor, N. & Lazarovici, P. *Pardachirus marmoratus* (Red Sea flatfish) secretion and its isolated toxic fraction pardaxin: the relationship between hemolysis and ATPase inhibition. *Toxicon* **19**, 573-8 (1981).

224. Yan, S. & Wu, G. Analysis on folding of misgurin using two-dimensional HP model. *Proteins.* **80**, 764-73 (2012).

225. Pundir, P., Catalli, A., Leggiadro, C., Douglas, S.E. & Kulka, M. Pleurocidin, a novel antimicrobial peptide, induces human mast cell activation through the FPRL1 receptor. *Mucosal. Immunol.* **7**, 177-87 (2014).

226. Lee, S.A. et al. Solution structure and cell selectivity of piscidin 1 and its analogues. *Biochemistry* **46**, 3653-63 (2007).

227. de Planque, M.R. et al. Interfacial anchor properties of tryptophan residues in transmembrane peptides can dominate over hydrophobic matching effects in peptide-lipid interactions. *Biochemistry.* **42**, 5341-8 (2003).

228. Baldus, M. Molecular interactions investigated by multi-dimensional solid-state NMR. *Curr. Opin. Struct. Biol.* **16**, 618-23 (2006).

229. Tugarinov, V. & Kay, L.E. Methyl groups as probes of structure and dynamics in NMR studies of high-molecular-weight proteins. *Chembiochem.* **6**, 1567-77 (2005).

230. Tugarinov, V., Kanelis, V. & Kay, L.E. Isotope labeling strategies for the study of high-molecular-weight proteins by solution NMR spectroscopy. *Nat. Protoc.* **1**, 749-54 (2006).

231. Ruschak, A.M. & Kay, L.E. Methyl groups as probes of supra-molecular structure, dynamics and function. *J. Biomol. NMR.* **46**, 75-87 (2010).

232. Religa, T.L. & Kay, L.E. Optimal methyl labeling for studies of supra-molecular systems. *J. Biomol. NMR.* **47**, 163-9 (2010).

233. Religa, T.L., Ruschak, A.M., Rosenzweig, R. & Kay, L.E. Site-directed methyl group labeling as an NMR probe of structure and dynamics in supramolecular protein systems: applications to the proteasome and to the ClpP protease. *J. Am. Chem. Soc.* **133**, 9063-8 (2011).

234. Bokoch, M.P. et al. Ligand-specific regulation of the extracellular surface of a G-protein-coupled receptor. *Nature.* **463**, 108-12 (2010).

235. Larda, S.T., Bokoch, M.P., Evanics, F. & Prosser, R.S. Lysine methylation strategies for characterizing protein conformations by NMR. *J. Biomol. NMR.* **54**, 199-209 (2012).

236. Xie, Q., Fulton, D.B. & Andreotti, A.H. A selective NMR probe to monitor the conformational transition from inactive to active kinase. *ACS Chem. Biol.* **10**, 262-8 (2015).

237. Liu, J.J., Horst, R., Katritch, V., Stevens, R.C. & Wuthrich, K. Biased signaling pathways in β_2-adrenergic receptor characterized by ^{19}F-NMR. *Science* **335**, 1106-10 (2012).

238. Shekhawat, S.S., Pham, G.H., Prabakaran, J. & Strieter, E.R. Simultaneous detection of distinct ubiquitin chain topologies by ^{19}F NMR. *ACS Chem Biol* **9**, 2229-36 (2014).

239. Huang, W. et al. Structural insights into micro-opioid receptor activation. *Nature.* **524**, 315-21 (2015).

240. Manglik, A. et al. Structural Insights into the Dynamic Process of β_2-Adrenergic Receptor Signaling. *Cell* **161**, 1101-11 (2015).

241. Cross, T.A., Murray, D.T. & Watts, A. Helical membrane protein conformations and their environment. *Eur. Biophys J.* **42**, 731-55 (2013).

242. Mandal, A. et al. Structural Changes and Proapoptotic Peroxidase Activity of Cardiolipin-Bound Mitochondrial Cytochrome C. *Biophys. J.* **109**, 1873-84 (2015).

243. Rankenberg, J.M. et al. Proline kink angle distributions for GWALP23 in lipid bilayers of different thicknesses. *Biochemistry.* **51**, 3554-64 (2012).

244. Sani, M.A., Whitwell, T.C. & Separovic, F. Lipid composition regulates the conformation and insertion of the antimicrobial peptide maculatin 1.1. *Biochim. Biophys. Acta.* **1818**, 205-11 (2012).

245. Weingarth, M. & Baldus, M. Solid-state NMR-based approaches for supramolecular structure elucidation. *Acc. Chem. Res.* **46**, 2037-46 (2013).

246. Lewandowski, J.R. et al. Enhanced Resolution and Coherence Lifetimes in the Solid-State NMR Spectroscopy of Perdeuterated Proteins under Ultrafast Magic-Angle Spinning. *J. Phys. Chem. Lett.* **2**, 2205-2211 (2011).

247. Takegoshi, K., Nakamura, S. & Terao, T. ^{13}C–^{1}H dipolar-assisted rotational resonance in magic-angle spinning NMR. *Chem. Phys. Lett.* **344**, 631-637 (2001).

248. Bers, D.M. Cardiac excitation-contraction coupling. *Nature.* **415**, 198-205 (2002).

249. Brini, M. & Carafoli, E. Calcium pumps in health and disease. *Physiol. Rev.* **89**, 1341-78 (2009).

250. Stokes, D.L. & Green, N.M. Three-dimensional crystals of CaATPase from sarcoplasmic reticulum. Symmetry and molecular packing. *Biophys. J.* **57**, 1-14 (1990).

251. Madden, T.D., Chapman, D. & Quinn, P.J. Cholesterol modulates activity of calcium-dependent ATPase of the sarcoplasmic reticulum. *Nature.* **279**, 538-41 (1979).

252. Chen, L. et al. Constant-Time Through-Bond ^{13}C Correlation Spectroscopy for Assigning Protein Resonances with Solid-State NMR Spectroscopy. *J. Am. Chem. Soc.* **128**, 9992-9993 (2006).

253. Gustavsson, M. et al. Allosteric regulation of SERCA by phosphorylation-mediated conformational shift of phospholamban. *Proc. Natl. Acad. Sci. U. S. A.* **110**, 17338-43 (2013).

254. Cady, S.D., Goodman, C., Tatko, C.D., DeGrado, W.F. & Hong, M. Determining the Orientation of Uniaxially Rotating Membrane Proteins Using Unoriented Samples: A ^{2}H, ^{13}C, and ^{15}N Solid-State NMR Investigation of the Dynamics and Orientation of a Transmembrane Helical Bundle. *J. Am. Chem. Soc.* **129**, 5719-5729 (2007).

255. Sengupta, I., Nadaud, P.S., Helmus, J.J., Schwieters, C.D. & Jaroniec, C.P. Protein fold determined by paramagnetic magic-angle spinning solid-state NMR spectroscopy. *Nat. Chem.* **4**, 410-7 (2012).

256. Vostrikov, V.V., Mote, K.R., Verardi, R. & Veglia, G. Structural dynamics and topology of phosphorylated phospholamban homopentamer reveal its role in the regulation of calcium transport. *Structure.* **21**, 2119-30 (2013).

257. Wawrzynow, A., Collins, J.H. & Coan, C. An iodoacetamide spin-label selectively labels a cysteine side chain in an occluded site on the sarcoplasmic reticulum calcium-ATPase. *Biochemistry.* **32**, 10803-10811 (1993).

258. Toyoshima, C. & Inesi, G. Structural basis of ion pumping by Ca^{2+}-ATPase of the sarcoplasmic reticulum. *Annu. Rev. Biochem.* **73**, 269-92 (2004).

259. Jensen, A.M., Sorensen, T.L., Olesen, C., Moller, J.V. & Nissen, P. Modulatory and catalytic modes of ATP binding by the calcium pump. *EMBO J.* **25**, 2305-14 (2006).

260. Toyoshima, C. & Mizutani, T. Crystal structure of the calcium pump with a bound ATP analogue. *Nature.* **430**, 529-35 (2004).

261. Toyoshima, C., Nakasako, M., Nomura, H. & Ogawa, H. Crystal structure of the calcium pump of sarcoplasmic reticulum at 2.6 A resolution. *Nature.* **405**, 647-55 (2000).

262. Winters, D.L., Autry, J.M., Svensson, B. & Thomas, D.D. Interdomain Fluorescence Resonance Energy Transfer in SERCA Probed by Cyan-Fluorescent Protein Fused to the Actuator Domain. *Biochemistry.* **47**, 4246-4256 (2008).

263. Espinoza-Fonseca, L.M. & Thomas, D.D. Atomic-level characterization of the activation mechanism of SERCA by calcium. *PLoS One.* **6**, e26936 (2011).

264. Hou, Z. et al. 2-Color calcium pump reveals closure of the cytoplasmic headpiece with calcium binding. *PLoS One.* **7**, e40369 (2012).

265. Gustavsson, M. et al. Lipid-mediated folding/unfolding of phospholamban as a regulatory mechanism for the sarcoplasmic reticulum Ca2+-ATPase. *J. Mol. Biol.* **408**, 755-65 (2011).

266. Adachi, T. et al. *S*-Glutathiolation by peroxynitrite activates SERCA during arterial relaxation by nitric oxide. *Nat. Med.* **10**, 1200-7 (2004).

267. Murphy, A.J. Sulfhydryl group modification of sarcoplasmic reticulum membranes. *Biochemistry.* **15**, 4492-4496 (1976).

268. Coan, C.R. & Inesi, G. Ca^{2+}-dependent effect of ATP on spin-labeled sarcoplasmic reticulum. *J. Biol. Chem.* **252**, 3044-9 (1977).

269. Kawakita, M., Yasuoka, K. & Kaziro, Y. Selective modification of functionally distinct sulfhydryl groups of sarcoplasmic reticulum Ca^{2+},Mg^{2+}-adenosine triphosphatase with *N*-ethylmaleimide. *J. Biochem.* **87**, 609-17 (1980).

270. Kawakita, M. & Yamashita, T. Reactive sulfhydryl groups of sarcoplasmic reticulum ATPase. III. Identification of cysteine residues whose modification with *N*-ethylmaleimide leads to loss of the Ca^{2+}-transporting activity. *J. Biochem.* **102**, 103-9 (1987).

271. Saito-Nakatsuka, K., Yamashita, T., Kubota, I. & Kawakita, M. Reactive sulfhydryl groups of sarcoplasmic reticulum ATPase. I. Location of a group which is most reactive with *N*-ethylmaleimide. *J. Biochem.* **101**, 365-76 (1987).

272. Suzuki, H., Obara, M., Kuwayama, H. & Kanazawa, T. A conformational change of *N*-iodoacetyl-*N'*-(5-sulfo-1-naphthyl)ethylenediamine-labeled sarcoplasmic reticulum Ca^{2+}-ATPase upon ATP binding to the catalytic site. *J. Biol. Chem.* **262**, 15448-56 (1987).

273. Yamashita, T. & Kawakita, M. Reactive sulfhydryl groups of sarcoplasmic reticulum ATPase. II. Site of labeling with iodoacetamide and its fluorescent derivative. *J. Biochem.* **101**, 377-85 (1987).

274. Bishop, J.E., Squier, T.C., Bigelow, D.J. & Inesi, G. (Iodoacetamido)fluorescein labels a pair of proximal cysteines on the calcium ATPase of sarcoplasmic reticulum. *Biochemistry.* **27**, 5233-5240 (1988).

275. Rice, W.J., Green, N.M. & MacLennan, D.H. Site-directed disulfide mapping of helices M4 and M6 in the Ca2+ binding domain of SERCA1a, the Ca^{2+} ATPase of fast twitch skeletal muscle sarcoplasmic reticulum. *J. Biol. Chem.* **272**, 31412-9 (1997).

276. Viner, R.I., Williams, T.D. & Schöneich, C. Peroxynitrite Modification of Protein Thiols: Oxidation, Nitrosylation, and *S*-Glutathiolation of Functionally Important Cysteine Residue(s) in the Sarcoplasmic Reticulum Ca-ATPase. *Biochemistry.* **38**, 12408-12415 (1999).

277. Sharov, V.S., Dremina, E.S., Galeva, N.A., Williams, T.D. & Schoneich, C. Quantitative mapping of oxidation-sensitive cysteine residues in SERCA in vivo and in vitro by HPLC-electrospray-tandem MS: selective protein oxidation during biological aging. *Biochem. J.* **394**, 605-15 (2006).

278. Cornea, R.L. et al. High-throughput FRET assay yields allosteric SERCA activators. *J. Biomol. Screen.* **18**, 97-107 (2013).

279. Clausen, J.D. et al. SERCA mutant E309Q binds two Ca(2+) ions but adopts a catalytically incompetent conformation. *EMBO J.* **32**, 3231-43 (2013).

280. Van Melckebeke, H. et al. Probing water accessibility in HET-s(218-289) amyloid fibrils by solid-state NMR. *J. Mol. Biol.* **405**, 765-72 (2011).

281. Weingarth, M. et al. Quantitative analysis of the water occupancy around the selectivity filter of a K+ channel in different gating modes. *J. Am. Chem. Soc.* **136**, 2000-7 (2014).

282. Xu, F. & Cross, T.A. Water: foldase activity in catalyzing polypeptide conformational rearrangements. *Proc. Natl. Acad. Sci. U. S. A.* **96**, 9057-61 (1999).

283. Hu, F., Schmidt-Rohr, K. & Hong, M. NMR detection of pH-dependent histidine-water proton exchange reveals the conduction mechanism of a transmembrane proton channel. *J. Am. Chem. Soc.* **134**, 3703-13 (2012).

284. Thennarasu, S. et al. Limiting an antimicrobial peptide to the lipid-water interface enhances its bacterial membrane selectivity: a case study of MSI-367. *Biochemistry.* **49**, 10595-605 (2010).

285. Levitt, D.G., Elias, S.R. & Hautman, J.M. Number of water molecules coupled to the transport of sodium, potassium and hydrogen ions via gramicidin, nonactin or valinomycin. *Biochim. Biophys. Acta.* **512**, 436-51 (1978).

286. Sanders, C.R. & Myers, J.K. Disease-related misassembly of membrane proteins. *Annu. Rev. Biophys. Biomol. Struct.* **33**, 25-51 (2004).

287. Disalvo, E.A. Membrane Hydration: A Hint to a New Model for Biomembranes. *Subcell. Biochem.* **71**, 1-16 (2015).

288. Englander, S.W., Downer, N.W. & Teitelbaum, H. Hydrogen exchange. *Annu. Rev. Biochem.* **41**, 903-24 (1972).

289. Spera, S., Ikura, M. & Bax, A. Measurement of the exchange rates of rapidly exchanging amide protons: Application to the study of calmodulin and its complex with a myosin light chain kinase fragment. *J. Biomol. NMR.* **1**, 155-165.

290. Wuthrich, K., Otting, G. & Liepinsh, E. Protein hydration in aqueous solution. *Faraday Discuss.*, 35-45 (1992).

291. Huang, H. & Melacini, G. High-resolution protein hydration NMR experiments: probing how protein surfaces interact with water and other non-covalent ligands. *Anal. Chim. Acta.* **564**, 1-9 (2006).

292. Hwang, T.-L., Mori, S., Shaka, A.J. & van Zijl, P.C.M. Application of Phase-Modulated CLEAN Chemical EXchange Spectroscopy (CLEANEX-PM) to Detect Water−Protein Proton Exchange and Intermolecular NOEs. *J. Am. Chem. Soc.* **119**, 6203-6204 (1997).

293. Ader, C. et al. Structural rearrangements of membrane proteins probed by water-edited solid-state NMR spectroscopy. *J. Am. Chem. Soc.* **131**, 170-6 (2009).

294. Huster, D., Yao, X. & Hong, M. Membrane protein topology probed by (1)H spin diffusion from lipids using solid-state NMR spectroscopy. *J. Am. Chem. Soc.* **124**, 874-83 (2002).

295. Williams, J.K., Tietze, D., Lee, M., Wang, J. & Hong, M. Solid-State NMR Investigation of the Conformation, Proton Conduction, and Hydration of the Influenza B Virus M2 Transmembrane Proton Channel. *J. Am. Chem. Soc.* **138**, 8143-8155 (2016).

296. Williams, J.K. & Hong, M. Probing membrane protein structure using water polarization transfer solid-state NMR. *J. Magn. Reson.* **247**, 118-27 (2014).

297. Zhang, Z. et al. Solid-state NMR shows that dynamically different domains of membrane proteins have different hydration dependence. *J. Phys. Chem. B.* **118**, 9553-64 (2014).

298. Bechinger, B. & Seelig, J. Conformational changes of the phosphatidylcholine headgroup due to membrane dehydration. A 2H-NMR study. *Chem. Phys. Lipids.* **58**, 1-5 (1991).

299. Opella, S.J. & Marassi, F.M. Structure Determination of Membrane Proteins by NMR Spectroscopy. *Chem. Rev.* **104**, 3587-3606 (2004).

300. Cross, T.A., Sharma, M., Yi, M. & Zhou, H.X. Influence of solubilizing environments on membrane protein structures. *Trends Biochem. Sci.* **36**, 117-25 (2011).

301. Miao, Y. & Cross, T.A. Solid state NMR and protein-protein interactions in membranes. *Curr. Opin. Struct. Biol.* **23**, 919-28 (2013).

302. Page, R.C., Li, C., Hu, J., Gao, F.P. & Cross, T.A. Lipid bilayers: an essential environment for the understanding of membrane proteins. *Magn. Reson. Chem.* **45 Suppl 1**, S2-11 (2007).

303. Zhou, H.X. & Cross, T.A. Modeling the membrane environment has implications for membrane protein structure and function: influenza A M2 protein. *Protein Sci.* **22**, 381-94 (2013).

304. Wang, S., Shi, L., Kawamura, I., Brown, L.S. & Ladizhansky, V. Site-specific solid-state NMR detection of hydrogen-deuterium exchange reveals conformational changes in a 7-helical transmembrane protein. *Biophys. J.* **101**, L23-5 (2011).

305. Ward, M.E. et al. Proton-detected solid-state NMR reveals intramembrane polar networks in a seven-helical transmembrane protein proteorhodopsin. *J. Am. Chem. Soc.* **133**, 17434-43 (2011).

306. Dvinskikh, S., Dürr, U., Yamamoto, K. & Ramamoorthy, A. A High-Resolution Solid-State NMR Approach for the Structural Studies of Bicelles. *J. Am. Chem. Soc.* **128**, 6326-6327 (2006).

307. Gopinath, T. & Veglia, G. Sensitivity enhancement in static solid-state NMR experiments via single- and multiple-quantum dipolar coherences. *J. Am. Chem. Soc.* **131**, 5754-6 (2009).

308. Marassi, F.M. & Opella, S.J. A solid-state NMR index of helical membrane protein structure and topology. *J. Magn. Reson.* **144**, 150-5 (2000).

309. Veglia, G., Zeri, A.C., Ma, C. & Opella, S.J. Deuterium/hydrogen exchange factors measured by solution nuclear magnetic resonance spectroscopy as indicators of the structure and topology of membrane proteins. *Biophys. J.* **82**, 2176-83 (2002).

310. Schmidt-Rohr, K. & Spiess, H.W. Multidimensional Solid-State NMR and Polymers. in *Multidimensional Solid-State NMR and Polymers* 1-12 (Academic Press, San Diego, 1994).

311. Veglia, G. et al. 1.11 The Hybrid Solution/Solid-State NMR Method for Membrane Protein Structure Determination. in *Comprehensive Biophysics* (ed. Egelman, E.H.) 182-198 (Elsevier, Amsterdam, 2012).

312. Buck, B. et al. Overexpression, purification, and characterization of recombinant Ca-ATPase regulators for high-resolution solution and solid-state NMR studies. *Protein Expr. Purif.* **30**, 253-61 (2003).

313. Gor'kov, P.L. et al. Using low-E resonators to reduce RF heating in biological samples for static solid-state NMR up to 900 MHz. *J. Magn. Reson.* **185**, 77-93 (2007).

314. Caravatti, P., Braunschweiler, L. & Ernst, R.R. Heteronuclear correlation spectroscopy in rotating solids. *Chem. Phys. Lett.* **100**, 305-310 (1983).

315. Lee, M. & Goldburg, W.I. Nuclear-Magnetic-Resonance Line Narrowing by a Rotating rf Field. *Phys. Rev.* **140**, A1261-A1271 (1965).

316. Levitt, M.H., Kolbert, A.C., Bielecki, A. & Ruben, D.J. High-resolution 1H NMR in solids with frequency-switched multiple-pulse sequences. *Solid State Nucl. Magn. Reson.* **2**, 151-63 (1993).

317. Hartmann, S.R. & Hahn, E.L. Nuclear Double Resonance in the Rotating Frame. *Phys. Rev.* **128**, 2042-2053 (1962).

318. Fung, B.M., Khitrin, A.K. & Ermolaev, K. An improved broadband decoupling sequence for liquid crystals and solids. *J. Magn. Reson.* **142**, 97-101 (2000).

319. Shi, L., Cembran, A., Gao, J. & Veglia, G. Tilt and azimuthal angles of a transmembrane peptide: a comparison between molecular dynamics calculations and solid-state NMR data of sarcolipin in lipid membranes. *Biophys. J.* **96**, 3648-62 (2009).

320. Quine, J.R. et al. Intensity and mosaic spread analysis from PISEMA tensors in solid-state NMR. *J. Magn. Reson.* **179**, 190-8 (2006).

321. Krishna, M.M., Hoang, L., Lin, Y. & Englander, S.W. Hydrogen exchange methods to study protein folding. *Methods.* **34**, 51-64 (2004).

322. Englander, S.W., Mayne, L., Kan, Z.Y. & Hu, W. Protein Folding-How and Why: By Hydrogen Exchange, Fragment Separation, and Mass Spectrometry. *Annu. Rev. Biophys.* **45**, 135-52 (2016).

323. Murray, D.T., Li, C., Gao, F.P., Qin, H. & Cross, T.A. Membrane protein structural validation by oriented sample solid-state NMR: diacylglycerol kinase. *Biophys. J.* **106**, 1559-69 (2014).

324. Zhou, H.X. & Cross, T.A. Influences of membrane mimetic environments on membrane protein structures. *Annu. Rev. Biophys.* **42**, 361-92 (2013).

325. Yamamoto, K., Soong, R. & Ramamoorthy, A. Comprehensive Analysis of Lipid Dynamics Variation with Lipid Composition and Hydration of Bicelles Using Nuclear Magnetic Resonance (NMR) Spectroscopy. *Langmuir.* **25**, 7010-7018 (2009).

326. Etzkorn, M. et al. Secondary structure, dynamics, and topology of a seven-helix receptor in native membranes, studied by solid-state NMR spectroscopy. *Angew. Chem. Int. Ed. Engl.* **46**, 459-62 (2007).

327. Liao, S.Y., Fritzsching, K.J. & Hong, M. Conformational analysis of the full-length M2 protein of the influenza A virus using solid-state NMR. *Protein Sci.* **22**, 1623-38 (2013).

328. Hasselbach, W. Quantitative aspects of the calcium concept of excitation contraction coupling--a critical evaluation. *Basic Res. Cardiol.* **75**, 2-12 (1980).

329. Simmerman, H.K., Collins, J.H., Theibert, J.L., Wegener, A.D. & Jones, L.R. Sequence analysis of phospholamban. Identification of phosphorylation sites and two major structural domains. *J. Biol. Chem.* **261**, 13333-41 (1986).

330. Simmerman, H.K. & Jones, L.R. Phospholamban: protein structure, mechanism of action, and role in cardiac function. *Physiol. Rev.* **78**, 921-47 (1998).

331. Akin, B.L., Hurley, T.D., Chen, Z. & Jones, L.R. The structural basis for phospholamban inhibition of the calcium pump in sarcoplasmic reticulum. *J. Biol. Chem.* **288**, 30181-91 (2013).

332. Jones, L.R., Cornea, R.L. & Chen, Z. Close proximity between residue 30 of phospholamban and cysteine 318 of the cardiac Ca2+ pump revealed by intermolecular thiol cross-linking. *J. Biol. Chem.* **277**, 28319-29 (2002).

333. Toyoshima, C. et al. Modeling of the inhibitory interaction of phospholamban with the Ca2+ ATPase. *Proc. Natl. Acad. Sci. U. S. A.* **100**, 467-72 (2003).

334. Bal, N.C. et al. Sarcolipin is a novel regulator of muscle based thermogenesis and metabolism in mammals. *FASEB J.* **27**, 1 (2013).

335. Morita, T. et al. Interaction sites among phospholamban, sarcolipin, and the sarco(endo)plasmic reticulum Ca(2+)-ATPase. *Biochem. Biophys. Res. Commun.* **369**, 188-94 (2008).

336. Stammers, A.N. et al. The regulation of sarco(endo)plasmic reticulum calcium-ATPases (SERCA). *Can. J. Physiol. Pharmacol.*, 1-12 (2015).

337. Shaikh, S.A., Sahoo, S.K. & Periasamy, M. Phospholamban and sarcolipin: Are they functionally redundant or distinct regulators of the Sarco(Endo)Plasmic Reticulum Calcium ATPase? *J. Mol. Cell. Cardiol.* **91**, 81-91 (2016).

338. Zamoon, J., Mascioni, A., Thomas, D.D. & Veglia, G. NMR solution structure and topological orientation of monomeric phospholamban in dodecylphosphocholine micelles. *Biophys. J.* **85**, 2589-98 (2003).

339. Traaseth, N.J. et al. Structural and dynamic basis of phospholamban and sarcolipin inhibition of Ca(2+)-ATPase. *Biochemistry.* **47**, 3-13 (2008).

340. Ghimire, H. et al. Probing the helical tilt and dynamic properties of membrane-bound phospholamban in magnetically aligned bicelles using electron paramagnetic resonance spectroscopy. *Biochim. Biophys. Acta.* **1818**, 645-50 (2012).

341. Verardi, R., Shi, L., Traaseth, N.J., Walsh, N. & Veglia, G. Structural topology of phospholamban pentamer in lipid bilayers by a hybrid solution and solid-state NMR method. *Proc. Natl. Acad. Sci. U. S. A.* **108**, 9101-6 (2011).

342. Clayton, J.C., Hughes, E. & Middleton, D.A. The cytoplasmic domains of phospholamban and phospholemman associate with phospholipid membrane surfaces. *Biochemistry.* **44**, 17016-26 (2005).

343. Abu-Baker, S. et al. The structural topology of wild-type phospholamban in oriented lipid bilayers using 15N solid-state NMR spectroscopy. *Protein Sci.* **16**, 2345-9 (2007).

344. Seidel, K. et al. Structural characterization of Ca(2+)-ATPase-bound phospholamban in lipid bilayers by solid-state nuclear magnetic resonance (NMR) spectroscopy. *Biochemistry.* **47**, 4369-76 (2008).

345. Gustavsson, M., Traaseth, N.J. & Veglia, G. Probing ground and excited states of phospholamban in model and native lipid membranes by magic angle spinning NMR spectroscopy. *Biochim. Biophys. Acta.* **1818**, 146-53 (2012).

346. de Meis, L. & Vianna, A.L. Energy interconversion by the Ca2+-dependent ATPase of the sarcoplasmic reticulum. *Annu. Rev. Biochem.* **48**, 275-92 (1979).

347. Danko, S., Daiho, T., Yamasaki, K., Liu, X. & Suzuki, H. Formation of the stable structural analog of ADP-sensitive phosphoenzyme of Ca2+-ATPase with occluded Ca2+ by beryllium fluoride: structural changes during phosphorylation and isomerization. *J. Biol. Chem.* **284**, 22722-35 (2009).

348. Sorensen, T.L., Moller, J.V. & Nissen, P. Phosphoryl transfer and calcium ion occlusion in the calcium pump. *Science.* **304**, 1672-5 (2004).

349. Espinoza-Fonseca, L.M., Autry, J.M. & Thomas, D.D. Sarcolipin and phospholamban inhibit the calcium pump by populating a similar metal ion-free intermediate state. *Biochem. Biophys. Res. Commun.* **463**, 37-41 (2015).

350. Lin, M.T. et al. Escherichia coli auxotroph host strains for amino acid-selective isotope labeling of recombinant proteins. *Methods Enzymol.* **565**, 45-66 (2015).

351. Reddy, L.G., Cornea, R.L., Winters, D.L., McKenna, E. & Thomas, D.D. Defining the molecular components of calcium transport regulation in a reconstituted membrane system. *Biochemistry.* **42**, 4585-92 (2003).

352. Reddy, L.G. et al. Functional reconstitution of recombinant phospholamban with rabbit skeletal Ca(2+)-ATPase. *J. Biol. Chem.* **270**, 9390-7 (1995).

353. Afara, M.R., Trieber, C.A., Ceholski, D.K. & Young, H.S. Peptide inhibitors use two related mechanisms to alter the apparent calcium affinity of the sarcoplasmic reticulum calcium pump. *Biochemistry.* **47**, 9522-30 (2008).

354. Trieber, C.A., Afara, M. & Young, H.S. Effects of Phospholamban Transmembrane Mutants on the Calcium Affinity, Maximal Activity, and Cooperativity of the Sarcoplasmic Reticulum Calcium Pump. *Biochemistry.* **48**, 9287-9296 (2009).

355. Trieber, C.A., Douglas, J.L., Afara, M. & Young, H.S. The Effects of Mutation on the Regulatory Properties of Phospholamban in Co-Reconstituted Membranes. *Biochemistry.* **44**, 3289-3297 (2005).

356. Young, H.S., Reddy, L.G., Jones, L.R. & Stokes, D.L. Co-reconstitution and co-crystallization of phospholamban and Ca(2+)-ATPase. *Ann. N. Y. Acad. Sci.* **853**, 103-15 (1998).

357. Levy, D., Gulik, A., Bluzat, A. & Rigaud, J.L. Reconstitution of the sarcoplasmic reticulum Ca(2+)-ATPase: mechanisms of membrane protein insertion into liposomes during reconstitution procedures involving the use of detergents. *Biochim. Biophys. Acta.* **1107**, 283-98 (1992).

358. Gopinath, T. & Veglia, G. Dual acquisition magic-angle spinning solid-state NMR-spectroscopy: simultaneous acquisition of multidimensional spectra of biomacromolecules. *Angew. Chem. Int. Ed. Engl.* **51**, 2731-5 (2012).

359. Gramolini, A.O. et al. Cardiac-specific overexpression of sarcolipin in phospholamban null mice impairs myocyte function that is restored by phosphorylation. *Proc. Natl. Acad. Sci. U. S. A.* **103**, 2446-51 (2006).

360. Hellstern, S. et al. Sarcolipin, the shorter homologue of phospholamban, forms oligomeric structures in detergent micelles and in liposomes. *J. Biol. Chem.* **276**, 30845-52 (2001).

361. Douglas, J.L., Trieber, C.A., Afara, M. & Young, H.S. Rapid, high-yield expression and purification of Ca2+-ATPase regulatory proteins for high-resolution structural studies. *Protein Expr. Purif.* **40**, 118-25 (2005).

362. Watanabe, M. & Konishi, M. Intracellular calibration of the fluorescent Mg2+ indicator furaptra in rat ventricular myocytes. *Pflugers Arch.* **442**, 35-40 (2001).

363. Smith, G.A., Vandenberg, J.I., Freestone, N.S. & Dixon, H.B. The effect of Mg2+ on cardiac muscle function: Is CaATP the substrate for priming myofibril cross-bridge formation and Ca2+ reuptake by the sarcoplasmic reticulum? *Biochem. J.* **354**, 539-51 (2001).

364. Peinelt, C. & Apell, H.J. Kinetics of the Ca(2+), H(+), and Mg(2+) interaction with the ion-binding sites of the SR Ca-ATPase. *Biophys. J.* **82**, 170-81 (2002).

365. Forge, V., Mintz, E. & Guillain, F. Ca2+ binding to sarcoplasmic reticulum ATPase revisited. I. Mechanism of affinity and cooperativity modulation by H+ and Mg2+. *J. Biol. Chem.* **268**, 10953-60 (1993).

366. Forge, V., Mintz, E., Canet, D. & Guillain, F. Lumenal Ca2+ dissociation from the phosphorylated Ca(2+)-ATPase of the sarcoplasmic reticulum is sequential. *J. Biol. Chem.* **270**, 18271-6 (1995).

367. Demuth, D., Haase, N., Malzacher, D. & Vogel, M. Effects of solvent concentration and composition on protein dynamics: 13C MAS NMR studies of elastin in glycerol-water mixtures. *Biochim. Biophys. Acta.* **1854**, 995-1000 (2015).

368. Chen, Z., Akin, B.L., Stokes, D.L. & Jones, L.R. Cross-linking of C-terminal residues of phospholamban to the Ca2+ pump of cardiac sarcoplasmic reticulum to probe spatial and functional interactions within the transmembrane domain. *J. Biol. Chem.* **281**, 14163-72 (2006).

369. Chen, Z., Stokes, D.L., Rice, W.J. & Jones, L.R. Spatial and dynamic interactions between phospholamban and the canine cardiac Ca2+ pump revealed with use of heterobifunctional cross-linking agents. *J. Biol. Chem.* **278**, 48348-56 (2003).

370. Mote, K.R. Structural Characterization of Sarcolipin by Solid State NMR and Investigation of its Role in the Regulation of Sarco(endo)plasmic Reticulum Calcium Adenosine-Triphospatase. *Retrieved from the University of Minnesota Digital Conservancy* (2014).

371. de Meis, L. Uncoupled ATPase activity and heat production by the sarcoplasmic reticulum Ca2+-ATPase. Regulation by ADP. *J. Biol. Chem.* **276**, 25078-87 (2001).

372. Inesi, G. & de Meis, L. Regulation of steady state filling in sarcoplasmic reticulum. Roles of back-inhibition, leakage, and slippage of the calcium pump. *J. Biol. Chem.* **264**, 5929-36 (1989).

373. Berman, M.C. Slippage and uncoupling in P-type cation pumps; implications for energy transduction mechanisms and regulation of metabolism. *Biochim. Biophys. Acta.* **1513**, 95-121 (2001).

374. Schoenmakers, T.J., Visser, G.J., Flik, G. & Theuvenet, A.P. CHELATOR: an improved method for computing metal ion concentrations in physiological solutions. *Biotechniques.* **12**, 870-4, 876-9 (1992).

375. Yount, R.G., Babcock, D., Ballantyne, W. & Ojala, D. Adenylyl imidodiphosphate, an adenosine triphosphate analog containing a P--N--P linkage. *Biochemistry.* **10**, 2484-9 (1971).

376. Olivieri, C. et al. Structure and membrane interactions of chionodracine, a piscidin-like antimicrobial peptide from the icefish Chionodraco hamatus. *Biochim. Biophys. Acta.* **1848**, 1285-93 (2015).

377. Vostrikov, V.V. et al. Ca(2+) ATPase Conformational Transitions in Lipid Bilayers Mapped by Site-directed Ethylation and Solid-State NMR. *ACS Chem. Biol.* **11**, 329-34 (2016).

378. Montigny, C. et al. S-palmitoylation and s-oleoylation of rabbit and pig sarcolipin. *J. Biol. Chem.* **289**, 33850-61 (2014).

379. Yokoe, S. et al. Inhibition of phospholamban phosphorylation by O-GlcNAcylation: implications for diabetic cardiomyopathy. *Glycobiology.* **20**, 1217-26 (2010).

380. Bond, M.R. & Hanover, J.A. O-GlcNAc cycling: a link between metabolism and chronic disease. *Annu. Rev. Nutr.* **33**, 205-29 (2013).

381. Bers, D.M. Calcium and cardiac rhythms: physiological and pathophysiological. *Circ. Res.* **90**, 14-7 (2002).

382. Haghighi, K., Gregory, K.N. & Kranias, E.G. Sarcoplasmic reticulum Ca-ATPase-phospholamban interactions and dilated cardiomyopathy. *Biochem. Biophys. Res. Commun.* **322**, 1214-22 (2004).

383. Kranias, E.G. & Hajjar, R.J. Modulation of cardiac contractility by the phospholamban/SERCA2a regulatome. *Circ. Res.* **110**, 1646-60 (2012).

384. Chen, Y.X. et al. Alternative O-GlcNAcylation/O-phosphorylation of Ser16 induce different conformational disturbances to the N terminus of murine estrogen receptor beta. *Chem. Biol.* **13**, 937-44 (2006).

385. Copeland, R.J., Bullen, J.W. & Hart, G.W. Cross-talk between GlcNAcylation and phosphorylation: roles in insulin resistance and glucose toxicity. *Am. J. Physiol. Endocrinol. Metab.* **295**, E17-28 (2008).

386. Hart, G.W., Slawson, C., Ramirez-Correa, G. & Lagerlof, O. Cross talk between O-GlcNAcylation and phosphorylation: roles in signaling, transcription, and chronic disease. *Annu Rev Biochem* **80**, 825-58 (2011).